

Role of Interfaces in Perovskite Devices

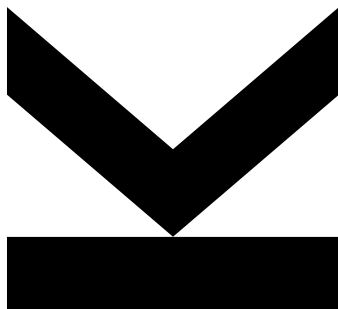
Submitted by
**MSc. Bekele Hailegnaw
Teklemariam**

Submitted at
**Linz Institute for Organic
Solar Cells (LIOS)/ Institute
of Physical Chemistry**

Supervisor and
First Examiner
**Assoc. Univ.-Prof. DI Dr.
Markus Clark Scharber**

Second Examiner
**Univ.-Prof. DI Dr. Martin
Kaltenbrunner**

November, 2019



Doctoral Thesis

to obtain the academic degree of

Doktor der Naturwissenschaften

in the Doctoral Program

Natural Science

STATUTORY DECLARATION

I hereby declare that the thesis submitted is my own unaided work, that I have not used other than the sources indicated, and that all direct and indirect sources are acknowledged as references.

This printed thesis is identical with the electronic version submitted.

Place, Date

Signature

Acknowledgements

First of all, I would like to express my deepest gratitude and respect to my supervisor Assoc. Univ. Prof. DI Dr. Markus Clark Scharber for his genuine guidance, encouragement and instructive and continuous feedback to all my work from the beginning to the end. Again I thank him deep from the bottom of my heart for his kind personality.

I am very much grateful to Prof. Niyazi Serdar Sariciftci for his kindheartedness to support me in all aspects, advice, encouragement and concurrent professional guidance during my study.

I would like to thank Dr. Getachew Adam for his all-round support and guidance during my work.

I was fortunate to have Dr. Christoph Ulbricht, discussing ideas with him was immensely important, helpful and of course more than fun.

I am thankful to DI Dr. Philipp Stadler for his kind assistance to work on Quantum Design DynaCool PPMS for magnetic characterization.

I would like to extend my gratitude to all members of the Linz Institute for Organic Solar Cells (LIOS) for their wonderful “parenthood” and kind support. I am thankful to Gerda Kalab for her support in purchasing chemicals. I thank Patrick John Denk for being a man of in need to fix the instruments and making the lab suitable for my research. Without the advice and support of our secretaries to handle bureaucratic issues, I wouldn’t focus on my research properly. I would like to thank Mrs. Birgit Paulik, Sara Gusner, and Isolde Wandling.

I thank Prof. Johannes David Pedarnig for his help to measure x-ray diffraction spectra.

I am grateful for the financial support of the Austrian Academy of Science in the framework of Chemical Monthly Fellowship.

I am thankful for the financial support of the Austrian Research Promotion Agency (FFG) in the framework of the project Flex!PV-2.0-85360 during my PhD study.

Finally, I thank my families: my father for being an inspiration and mothers, brothers and sisters for their material and spiritual support, and for their encouragement which gave me reinforcement in my life that I am truly grateful for.

Abstract

Perovskite solar cells are a class of swiftly evolving next-generation photovoltaic devices that have attracted a lot of interest due to their exceedingly improving performance, low processing costs and the excellent optoelectronic properties of the perovskite semiconductors. However, issues related to device processing reproducibility, anomalous hysteresis, scalability as well as factors, limiting the performance and stability of the devices, are hampering the advancement of this technology. The development of reproducible and optimal processing conditions and a detailed understanding of processes related to charge transport and recombination in the perovskite devices are required before considering large scale production and commercialization. Also, the proper choice of charge transport materials and the engineering of interfaces are found to be crucial for the overall performance and stability of perovskite devices.

In this PhD thesis, the effect of different charge-transport layers and interfaces present in the device stack on the performance and stability of perovskite devices were studied. In addition, the role of processing additives, used to control the formation of the perovskite absorber material, was investigated. The main objective of the research was to prepare efficient, reproducible and stable so-called inverted (p-i-n) perovskite solar cells.

In the framework of this thesis various electron transport materials were tested. Thin layers of low temperature processed titanium oxide or different polyphosphazene derivatives were used as an additional buffer layer in perovskite solar cells to improve the cathodic interface of the device. Solar cells with an additional buffer layer were found to exhibit improved photocurrent density-voltage characteristics with reduced hysteresis and improved overall device performance and stability.

The morphology and crystallinity of the photoactive perovskite layer determine to a large extent the performance and stability of perovskite solar cells. Solvent engineering is an effective technique to design and control the formation of thin films of high-quality perovskite materials. In this thesis, acetylacetone was used as a solvent additive to modify the morphology and crystallinity of mixed halide perovskite films and to improve the device performance. Perovskite solar cells processed with acetylacetone show improved photovoltaic properties with good stability under continuous operation in ambient air.

Thorough characterization of the perovskite devices was performed using various optical, electrical and microscopic techniques. Current density-voltage and external quantum efficiency measurements were applied to evaluate the photon utilization efficiency of the perovskite solar cells. Impedance spectroscopy was used to characterize the charge carrier dynamics in the bulk and at the interfaces of perovskite solar cells. To study the optical properties of perovskite films in combination with different charge transport interlayers, photoluminescence and

photoluminescence decay spectroscopy were applied. Space-charge limited current and Mott-Schottky plot analysis were used to depict trap-states density and recombination channels in the perovskite devices. Atomic force microscopy and scanning electron microscopy were applied to characterize the topography of the sample devices.

Furthermore, the long-term stability of the optimized perovskite solar cells was studied under continuous operation and ambient conditions. The experimental results suggest that the decay of the device performance under continuous operation is mainly related to changes in the photoactive perovskite film and ion migration.

Overall, this dissertation reveals the importance of proper device design and processing. The findings suggest that to achieve highly efficient and stable perovskite solar cells, one needs to consider the combined effect of careful interface and compositional engineering and processing conditions of the perovskite devices.

Kurzfassung

Perowskit-Solarzellen sind eine Klasse von sich schnell entwickelnden Photovoltaikerelementen der nächsten Generation, die aufgrund ihres ausgezeichneten Wirkungsgrads, der niedrigen Herstellungskosten und der hervorragenden optoelektronischen Eigenschaften der Perowskithalbleiter großes Interesse erregt. Probleme im Zusammenhang mit unzureichender Reproduzierbarkeit in der Zellproduktion, anomalen Hystereseverläufen, der Skalierbarkeit, sowie Faktoren, die die Leistung und Stabilität der Zellen einschränken, behindern jedoch die Weiterentwicklung dieser Technologie. Die Entwicklung reproduzierbarer und optimierter Verarbeitungsbedingungen, und ein detailliertes Verständnis der Transport- und der Rekombinationsprozesse von Ladungsträgern in Perowskit-Solarzellen sind erforderlich, bevor eine großflächige Produktion und Kommerzialisierung in Betracht gezogen werden können. Auch die richtige Auswahl der Ladungstransportmaterialien und die Verbesserung der Grenzflächen sind für die Gesamtleistung und Stabilität der Perowskitsolarzellen von entscheidender Bedeutung.

In dieser Dissertation wurde der Einfluss verschiedener Ladungstransportschichten und Grenzflächen im Bauteilstapel auf den Wirkungsgrad und die Stabilität von Perowskit-Solarzellen untersucht. Zusätzlich wurde die Rolle von Prozessadditiven untersucht, die zur Kontrolle der Bildung des Perowskit-Absorbermaterials verwendet werden. Das Hauptziel der Forschung war die Herstellung von effizienten, reproduzierbaren und stabilen sogenannten invertierten (p-i-n) Perowskit-Solarzellen.

Im Rahmen dieser Arbeit wurden verschiedene Elektronentransportmaterialien getestet. Dünne Schichten aus Titanoxid, die bei niedrigen Temperaturen erzeugt wurden, oder aus verschiedenen Polyphosphazenderivaten wurden als zusätzliche Pufferschicht verwendet, um die kathodische Grenzfläche in Perowskitsolarzellen zu verbessern. Es wurde beobachtet, dass Solarzellen mit einer solchen zusätzlichen Pufferschicht verbesserte Photostromdichte-Spannungseigenschaften bei reduzierter Hysterese mit erhöhter Gesamtleistung und Stabilität aufweisen.

Die Morphologie und Kristallinität der photoaktiven Perowskitschicht bestimmen in hohem Maße die Leistungsfähigkeit und Stabilität von Perowskit-Solarzellen. Lösungsmittel-Engineering ist eine effektive Technik, um die Bildung dünner Filme aus hochwertigen Perowskitmaterialien zu kontrollieren. In dieser Arbeit wurde Acetylaceton als Lösungsmittelzusatz verwendet, um die Morphologie und Kristallinität von gemischten Halogenidperowskitfilmen zu modifizieren und dadurch den Wirkungsgrad der hergestellten Zellen zu verbessern. Perowskit-Solarzellen, die mit Acetylaceton verarbeitet wurden, weisen verbesserte photovoltaische Eigenschaften mit guter Stabilität bei Langzeit-Betrieb unter atmosphärischen Bedingungen auf.

Eine gründliche Charakterisierung der Perowskitesolarzellen wurde mit verschiedenen optischen, elektrischen und mikroskopischen Techniken durchgeführt. Messungen der Stromdichte-Spannungs-Kennlinien und der externen Quanteneffizienz wurden verwendet, um den Wirkungsgrad der Perowskitesolarzellen zu bestimmen. Impedanzspektroskopie wurde genutzt, um die Ladungsträgerdynamik im Halbleiter und an den Grenzflächen der Perowskitesolarzellen zu charakterisieren. Um die optischen Eigenschaften von Perowskitfilmen in Kombination mit verschiedenen Ladungstransportzwischen-schichten zu untersuchen, wurden Photolumineszenz- und Photolumineszenz-Zerfallsspektroskopie angewendet. Raumladungsbegrenzter Strom und Mott-Schottky-Analyse wurden verwendet, um die Defektdichte und die Rekombinationskanäle in den Zellen zu erforschen. Rasterkraftmikroskopie und Rasterelektronenmikroskopie wurden angewendet, um die Topographie der Halbleiterschichten zu charakterisieren.

Darüber hinaus wurde die Langzeitstabilität der optimierten Perowskitesolarzellen unter Dauerbetrieb und Umgebungsbedingungen untersucht. Die experimentellen Ergebnisse legen nahe, dass die Abnahme des Wirkungsgrads im Dauerbetrieb hauptsächlich mit Änderungen des photoaktiven Perowskitfilms und der Ionenmigration zusammenhängt.

Die präsentierten Ergebnisse untermauern, dass für hocheffiziente und stabile Perowskitesolarzellen ein optimierter Herstellungsprozess und die richtige Wahl der Grenzschichten erforderlich sind.

List of Papers Included in the Thesis

This dissertation combines the findings discussed in the following scientific papers. The findings from the papers are included in section “3” with subtitle “3.i”, where “i” is the paper number (i = 1, 2, 3 and 4) indicated here.

Paper-1: Inverted (p-i-n) Perovskite Solar Cells Using Low Temperature Processed TiO_x Interlayer
Bekele Hailegnaw, Getachew Adam, Herwing Heilbrunner, Dogukan H. Apaydin, Christoph Ulbricht, Niyazi Serdar Sariciftci and Markus Clark Scharber,
RSC Advances, 2018, 8, 24836-24846.

Paper-2: Improving the Performance of Perovskite Solar Cells Using a Polyphosphazene Interfacing layer
Bekele Hailegnaw, Vanessa Poscher, Christoph Ulbricht, Hathaichanok Seelajaroen, Ian Teasdale, Yolanda Salinas, Niyazi Serdar Sariciftci and Markus Clark Scharber,
Physica Status Solidi A 2019, 1900436(1-10).

Paper-3: Acetylacetone Improves the Performance of Planar Mixed Halide Perovskite Solar Cells,
Bekele Hailegnaw, Getachew Adam, Dominik Wielend, Johannes David Pedarnig, Niyazi Serdar Sariciftci and Markus Clark Scharber,
Journal of Physical Chemistry C 2019, 123, 23807-23816.

Paper-4: Impedance Spectroscopy of Perovskite Solar Cells: Studying the Physico-chemical Dynamics Under Continuous Operation
Bekele Hailegnaw, Niyazi Serdar Sariciftci and Markus Clark Scharber,
Manuscript to be submitted.

Contribution Report

Paper-1: I am the main author and responsible for data analysis. Device fabrication, optimization, and characterization were done together with Getachew Adam. Photoluminescence and Photoluminescence decay measurements were conducted together with Herwing Heilbrunner. SEM was conducted by Dogukan H. Apaydin. The titanium oxide sol-gel was synthesized together with Christoph Ulbricht. The electroluminescence was recorded together with Markus C. Scharber and wrote the manuscript together with the co-authors.

Paper-2: I am the main author and did data analysis, device fabrication, optimization, and characterization. Polyphosphazene derivatives were synthesized by Vanessa Poscher. Hathaichanok Seelajaroen measured the cyclic voltammetry of the Polyphosphazene film. The titanium oxide sol-gel was synthesized together with Christoph Ulbricht. I wrote the manuscript together with the co-authors.

Paper-3: I am the main author and responsible for data analysis, device fabrication, optimization, and characterization. SEM was done together with Domink Wielend, and the XRD was measured together with Johannes D. Pedarnig. The manuscript was written together with the co-authors.

Paper-4: I am the main author and did the device fabrication and characterization. Data analysis was done together with Markus C. Scharber and wrote the manuscript together with both Niyazi S. Sariciftci, Markus C. Scharber.

Publications not Included in the Thesis

Paper-I: Optoelectronic Properties of Layered Perovskite Solar Cells,
Bekele Hailegnaw, Sanghyun Paek, Kyung Taek Cho, Yonghui Lee, Fathi Ongül,
Mohammad Khaja Nazeeruddin and Markus Clark Scharber,
Solar Rapid Research Letters, 2019, 1900126(1-6).

Paper-II: The influence of perovskite precursor composition on the morphology and photovoltaic performance of mixed halide MAPb_{1-3-x}Cl_x solar cells
Sekai Tombe, Getachew Adam, Herwing Heilbrunner, Cigdem Yumusak, Dogukan H. Apaydin, Bekele Hailegnaw, Christoph Ulbricht, Christopher J. Arendse, Heinz Langhals, E. Iwuohaa, Niyazi Serdar Sariciftci and Markus Clark Scharber,
Solar Energy, 2018, 163, 215-223.

Paper-III: Growth of Magneto-Optically Active Crystals at Room Temperature
Bekele Hailegnaw, Owe Monkovious, Mariano Desusa, Alexander Kovalenko, Philipp Staddler, Niyazi Serdar Sariciftci and Markus Clark Scharber,
Manuscript

Paper-IV: Nanoscale Investigation of Charge Carrier Dynamics in Triple-cation Mixed-halide Perovskite at Second-microsecond Timescales via Kelvin Probe Force Microscopy
David Toth, Bekele Hailegnaw, Filipe Richheimer, Sebastian Wood, Ferry Kienberger Markus Clark Scharber and Georg Gramse,
Manuscript

Role of Interfaces in Perovskite Devices

Table of Contents

Goals and Objectives of the Thesis.....	12
1. Introduction.....	13
1.1. History of Solar Cells	13
1.2. Perovskite Solar Cells.....	14
1.2.1. Compositional Engineering in Perovskite Solar Cells.....	15
1.2.2. Interface Engineering in Perovskite Solar Cells	19
2. Experimental Section.....	24
2.1. Materials.....	24
2.1.1. Synthesis of Organic Halides.....	25
2.1.2. Synthesis of Nickel Oxide (NiO _x) Nanoparticles	25
2.1.3. Synthesis of TiO _x Sol-gel	26
2.2. Preparation of the Perovskite Precursors.....	27
2.2.1. Mixed-Halide Perovskite (CH ₃ NH ₃ PbI _{3-x} Cl _x)	27
2.2.2. Mixed-Cation Mixed-Halide Perovskite (CsFAMAPbI _{3-x} Br _x).....	27
2.3. Device Fabrication.....	27
2.4. Characterization Techniques	29
2.4.1. Profilometer	29
2.4.2. Optical Spectroscopy.....	30
2.4.3. X-ray Diffraction Spectroscopy	31
2.4.4. Microscopy	32
2.4.5. Optoelectronic Characterization.....	34
2.4.6. Impedance Spectroscopy	36
2.4.7. Capacitance-Voltage Measurement.....	45
3. Results and Discussion.....	46
3.1. Low Temperature Processed TiO _x Interfacial Layer for Inverted p-i-n Perovskite Solar Cells	46
3.1.1. Current Density-Voltage Response.....	47
3.1.2. Topographic and Optoelectronic Results	49
3.1.3. Impedance Spectroscopy (IS).....	51
3.1.4. Device Optimization.....	53
3.1.5. Stability Study.....	56
3.1.6. Conclusion.....	59

3.2. The Role of Polyphosphazene Buffer Layer in Inverted Mixed-Cation Mixed-Halide Perovskite Solar Cells	60
3.2.1. Cyclic Voltammetry and Optical Characterization	60
3.2.2. Current Density-Voltage Response.....	64
3.2.1. Poly[bis(allylamino)phosphazene] ((PPz5) Thickness Optimization	65
3.2.1. Impedance Spectroscopy	69
3.2.2. Organic Solar Cells.....	72
3.2.3. Conclusion.....	73
3.3. Solvent Additive In Mixed-Halide Perovskite Solar cells.....	74
3.3.1. Acetylacetone Solvent Additive.....	74
3.3.2. Crystallographic and Optical Results	74
3.3.3. Space-Charge-Limited Current (SCLC)	78
3.3.4. Current Density-Voltage Response.....	78
3.3.5. Capacitance-Voltage (C-V) and Mott-Schottky Plot.....	80
3.3.6. Stability Study.....	85
3.3.7. Impedance Spectroscopy	86
3.3.8. Conclusion.....	90
3.4. Stability Study of Mixed Halide PSCs Using Impedance Spectroscopy.....	91
3.4.1. Introduction.....	91
3.4.2. Electrochemical Impedance Spectroscopy (EIS) Results.....	93
3.4.3. Intensity Modulated Photovoltage Spectroscopy (IMVS) Results.....	96
3.4.4. Capacitance-Voltage (C-V) Results	99
3.4.5. Conclusion.....	100
Summary and Outlook	102
References	104
Curriculum Vitae	113

Goals and Objectives of the Thesis

Perovskite solar cells (PSCs) undoubtedly continue to attract tremendous interest in the scientific community for the last 10 years, with an outstanding improvement of their photovoltaic performance from 3.8 % in 2009 to the current record above 25 %. Since 2012, radical improvements in the device performance have been achieved through careful control of the device fabrication process, the composition of the photoactive materials, extensive optimization of advanced structures, and many exciting theoretical and experimental studies. Despite the extraordinary progress in the performance and optoelectronic properties, there are many substantial challenges that need to be addressed before the technology can be commercialized on a larger scale. Issues related to reproducible device fabrication, long term stability of the devices, anomalous hysteretic current density-voltage (J-V) characteristics and the use of lead in the absorber material are among the most challenging problems which need to be solved.

The precise selection and engineering of interfaces play a crucial role in the charge extraction processes, the hysteresis behavior and the stability of perovskite devices, and deserves further detailed investigations. Inverted perovskite solar cells commonly deliver lower open-circuit voltages, which is attributed to losses at the interfaces due to charge carriers recombination and/or energetic offsets across the interfaces. It is generally accepted that non-radiative recombination has a detrimental impact on the performance of photovoltaic devices.

The objectives of this PhD research are:

- To understand the role of surfaces and interfaces on the performance and stability of inverted (p-i-n) perovskite devices
- To study the role of selected processing additives on the performance and stability of perovskite opto-electronic devices
- To develop a detailed understanding of the effect of surfaces and interfaces on the charge carrier dynamics in perovskite devices
- To find hole and electron transport layers for inverted perovskite solar cells to improve the photon energy utilization (reduced open-circuit voltage losses) and power conversion efficiency
- To identify charge transport layers which are robust and can function as an encapsulation for the photoactive perovskite layer against polar solvents
- To optimize the performance and stability of inverted perovskite devices
- To develop facile and reproducible methods to process the perovskite films and to fabricate devices
- Furthermore, to utilize different optical and electrical characterization techniques to study the perovskite devices.

1. Introduction

The ever growing energy demand, food insecurity and environmental issues are among the most menacing issues facing humanity in the 21st century. The current energy consumption of our global society is above 18.5 TW, and is expected to reach about 30 TW by 2050.^[1] Currently, more than 80 % of our energy consumption is based on non-renewable fossil fuels which are associated with threatening drawbacks. Aside from its unsustainability, it releases greenhouse gases like carbon dioxide (CO₂), methane, and nitrogen oxide (NO_x). If mankind continues burning fossil fuels with such an increasing rate, the annual CO₂ emission from energy-related sources will exceed 37 Giga tons by 2035. This would lead to an average global temperature increase, causing a reduction of agricultural productions, polar ice melting, rising of ocean levels and frequent floodings, storms and droughts around the world. It becomes a must to identify environmental friendly, affordable, CO₂-free and renewable energy sources to limit the rise of the global temperature and to put our future on a more safe and sustainable footing.^[2,3,4]

There are several renewable energy options like solar energy, hydroelectric, geothermal, biomass, tidal energy and wind. Solar energy is likely the most promising candidate practically inexhaustible, CO₂-free and ecologically pure energy. The sun emits a large amount of electromagnetic radiation with a power of about 3.83×10^{23} kilowatts per second. Although most of this radiation is lost to the space, the amount of radiation that strikes the earth's surface in one hour would be sufficient to cover the amount of energy consumed by all human activities in one year. After reflection and absorption through the atmosphere some 120,000 TW of radiation (5 % ultraviolet; 43 % visible and 52 % infrared) reaches to the surface of Earth.^[2,5,6] Besides to these, it is also environmentally benign, as there are no pollution or waste byproducts that come out of it. Therefore, solar energy is an indispensable option for our future sustainable energy quest.

1.1. History of Solar Cells

Humanity has been using solar radiation as source of energy for generations. During the ancient civilizations, traditional solar technologies were used for warming habitations and water heating. Socrates (470-399 B.C) taught the importance of constructing homes in a way, that sun rays could warm the interior rooms during winter. In 212 B.C., Archimedes supposedly used solar radiation in warfare, to burn Roman ships by using parabolic mirrors to reflect and focus sunlight. In the 1st to 4th centuries A.D. Romans used south-faced large windows to warm their bathhouses.^[7-9]

In the Renaissance, concentration and conversion of solar radiation were studied. In 1839, A. E. Becquerel discovered the photovoltaic (PV) effect, upon illumination of connected platinum electrodes immersed in an acidic solution containing silver halide salt. Since then the idea of converting light into electric power or chemical fuels increasingly attracts researchers and engineers. In 1873, W. Smith discovered the photoconductivity effect in selenium. Three years

later (1876) W. Adams found photovoltaic characteristics in solidified selenium when shining a light on it. After seven years (in 1883), C. Fritts fabricated the first solar cell using selenium/gold junction. In 1905, Albert Einstein explained the nature of light and the photoelectric effect on which the working principle of photovoltaic technology is based.^[7,8,10]

In 1954, D.M. Chapin, C.S. Fuller, and G.L. Pearson, of Bell Laboratories constructed the first practical silicon solar cell (SC) with a power conversion efficiency (PCE) of about 6%.^[7] This opened an entirely new era allowing the conversion of solar energy directly to electricity. Since then, several different photovoltaic technologies were discovered. Photovoltaic cells are commonly classified into three generations based on the underlying technology. The first photovoltaic cells are based on single-crystal and multi-crystalline silicon and commonly known as first generation photovoltaic devices. These cells have a theoretical maximum efficiency of 31%. Most commercial solar cells today are based on this technology. These cells are efficient and stable but also expensive, in terms of capital as well as energy investment. Trying to address these limitations, the second generation solar cells based on thin-film inorganic semiconductors like cadmium telluride (CdTe), copper indium gallium selenide (CIGS) and amorphous silicon (a-Si) are applied. These cells gained an economic advantage over the first generation but are commonly less efficient, and need improvement to become an even more viable option. Further development and application of new concepts led to the third generation photovoltaic cells, which include multi-layer (tandem) cells, multi electron-hole pairs per photon cells, thermophotovoltaic cells and emerging photovoltaics. Emerging photovoltaics are based on low-cost thin films of inorganic and hybrid semiconductors, organic/inorganic dyes, inorganic quantum dots, organic polymers and molecules and, more recently organo-metal halide perovskites.^[3,5,8,11]

1.2. Perovskite Solar Cells

Perovskite solar cells are the fastest growing field in optoelectronics, which have attracted enormous interest in the scientific community during the last few years. Perovskites are materials which have similar structure compared to the mineral calcium titanate (CaTiO_3) and general formula of ABX_3 as shown in Figure 1.1. Here, A is a monovalent organic or inorganic cation such as methylammonium (CH_3NH_3^+), formamidinium ($\text{HC}(\text{NH}_2)_2^+$), ethylammonium ($\text{CH}_3\text{CH}_2\text{NH}_3^+$), guanidinium ($\text{C}(\text{NH}_2)_3^+$), Cs^+ , Rb^+ , etc.; B corresponds to a divalent and/or trivalent metal ion which includes Pb^{2+} , Sn^{2+} , Cr^{2+} , Mn^{2+} , Ni^{2+} , Co^{2+} , Fe^{2+} , Cu^{2+} , Bi^{3+} , Ge^{2+} , Eu^{2+} , Yb^{2+} , etc.; and the anion X represent halides (I^- , Br^- , Cl^- and mixture of halides) and other monovalent anions with similar size with halides such as borontetrafluoride (BF_4^-) and thiocyanide (SCN^-).^[12-17]

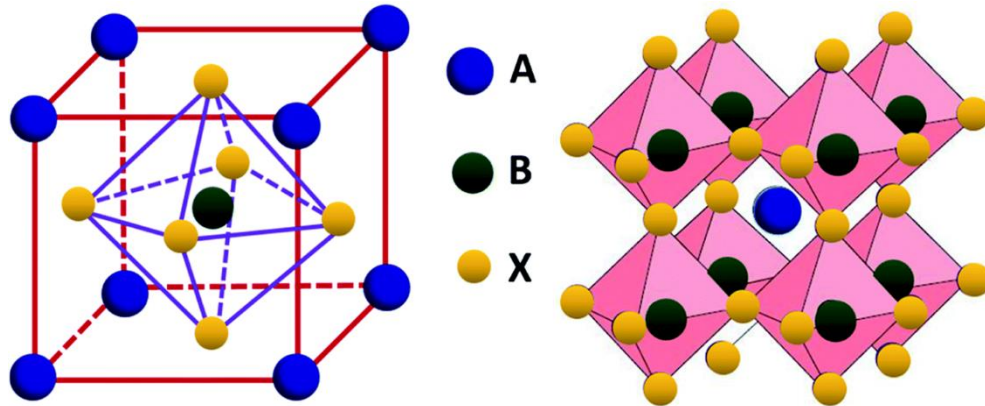


Figure 1.1: Schematic representation of perovskite crystals having a general formula of ABX_3 .^[16]

These materials possess unique optoelectronic and chemical properties. High absorption coefficients, small exciton binding energies, long carrier diffusion lengths (due to high mobilities and long charge lifetimes), ease of solution processability, high structural defect tolerance and shallow intrinsic defects, and benign grain boundary effects make this class of materials highly appealing. It is also possible to tune the band-gap of the perovskites to a large extent by the choice of metal cation, inorganic anions, and organic/inorganic cations.^[16-20] These characteristics make it to be a promising candidate in many optoelectronic applications, such as photovoltaics, photodetectors, light emission, X-ray imaging, lasers, gamma-ray detection, subwavelength photonic devices in long-wavelength region.^[21-25]

The first perovskite solar cell was reported by Miyasaka et al. in 2009 with a PCE of about 3.8 %.^[26] It was fabricated by adopting a dye-sensitized solar cell architecture in which the photoactive perovskite material was deposited on a mesoporous TiO_2 electron-collector. In 2011, Park et al. improved the PCE to about 6.5 % with the same dye-sensitized concept.^[27] Further improvement of PCE to about 9.7 % was achieved in 2012 by replacing the liquid electrolyte with a solid organic hole transporting material.^[28,29] Since then, many exciting theoretical and experimental studies were conducted to understand the optoelectrical properties of these materials. Unprecedented improvements and breakthroughs in the PCE of perovskite solar cells (PSCs) have been accomplished through extensive optimization of thin-film growth, compositional and interfacial engineering.^[14,30-37] The current record efficiency of PSC exceeds 25 % which makes it one of the fastest evolving photovoltaic technologies, and comparable in efficiency with silicon, cadmium telluride and other high-performance solar cells.^[28,38,39,40]

1.2.1. Compositional Engineering in Perovskite Solar Cells

A wide variety of three-dimensional (3D) and two-dimensional (2D) perovskite photoactive materials with the corresponding unique chemical, mechanical and optoelectronic properties have been reported. These materials are synthesized via mixing precursor salts in appropriate ratios, and complete or partial substitution of different cations, divalent metals and halide anions in the

ABX_3 complex. The dimensionality and phase of the resulting perovskite crystal is dependent on the size correlation of the component ions, and is in accordance with Goldschmidt tolerance factor (t).^[41] It has been shown that controlling the composition and ratio of the component ions allow to tune the band-gap, photo-absorption, stability and performance of the resulting devices. There are many classes of perovskites obtained by controlling the composition and ratio of one ion or combination of more than one ion.^[42-44]

1.2.1.1. Halide Ions (X-) Variation

Many researchers investigated the role of varying and mixing the halide ion in the perovskite structure. It is proven that halide composition plays a vital role in controlling the intrinsic properties of the perovskites (such as electronic and optical properties), on the crystal phase, crystal growth dynamics, film morphology and thus the performance of perovskite devices.

In 2013, Noh et al. verified the possibility of band-gap engineering via chemical management in methylammonium (MA) perovskites ($CH_3NH_3PbI_{3-x}Br_x$).^[45] Besides band-gap tuning, it was shown that the substitution of I^- with Br^- in the perovskite matrix increases the thermal and ambient condition stability of the perovskite films, as the distorted tetragonal crystal phase of methylammonium lead iodide ($MAPbI_3$) changed to more ordered and symmetric cubic phase.^[45-47] Furthermore, mixed halide perovskites ($MAPbI_{3-x}Cl_x$) with I^- and Cl^- anion source were found to show longer charge diffusion lengths with improved photophysical properties, better processability and stability compared to pristine $MAPbI_3$. Studies suggest that the presence of Cl^- ion facilitates the nucleation and crystal growth of $MAPbI_{3-x}Cl_x$ perovskite which exhibits nearly the same Fermi level as $MAPbI_3$.^[13,31,48,49]

1.2.1.2. A-Cation Variation

Methylammonium lead iodide is one of the most commonly studied perovskite materials. But this material is chemically unstable when exposed to moisture, heat, or light.^[50-52] A remarkable improvement of the thermal and moisture stability, mechanical robustness and overall device performance of perovskite solar cells was achieved via compositional designing of the A-cation. Partial or complete substitution of thermally unstable and photosensitive organic cations with inorganic Cs^+ ions has demonstrated to boost the stability of the perovskite structure. Partial incorporation of Rb shows further enhancement of the film robustness and device stability.^[14,19,53-56]

Snaith et al. demonstrated that partial replacement of the photosensitive FA by Cs ions has a tremendous effect on the thermal, mechanical and photostability of perovskite films. They demonstrated structurally stable mixed-cation mixed-halide perovskite ($Cs_{0.17}FA_{0.83}PbI_{3-x}Br_x$) with a band-gap of about 1.75 eV (Figure 1.2). Mixed-halide perovskite ($FAPbI_{3-x}Br_x$) films show yellowing of the films with Br^- composition in the range of 0.9 to 0.18, while $Cs_{0.17}FA_{0.83}PbI_{3-x}Br_x$ films remain continuous dark films throughout these compositional range (Figure 1.2(a) and (b)).

The UV-Vis absorption spectral response of $\text{Cs}_{0.17}\text{FA}_{0.83}\text{PbI}_{3-x}\text{Br}_x$ films shows a sharp optical band edge for all Br fractions (Figure 1.2(d)). $\text{FAPbI}_{3-x}\text{Br}_x$ films with elevated bromide content show strong tendencies for band edges at higher energies (Figure 1.2(c)). XRD spectra of $\text{Cs}_{0.17}\text{FA}_{0.83}\text{PbI}_{3-x}\text{Br}_x$ films (Figure 1.2(f)) show a well-defined single phase for all compositions which further indicates phase stability achieved due to Cs incorporation.^[19]

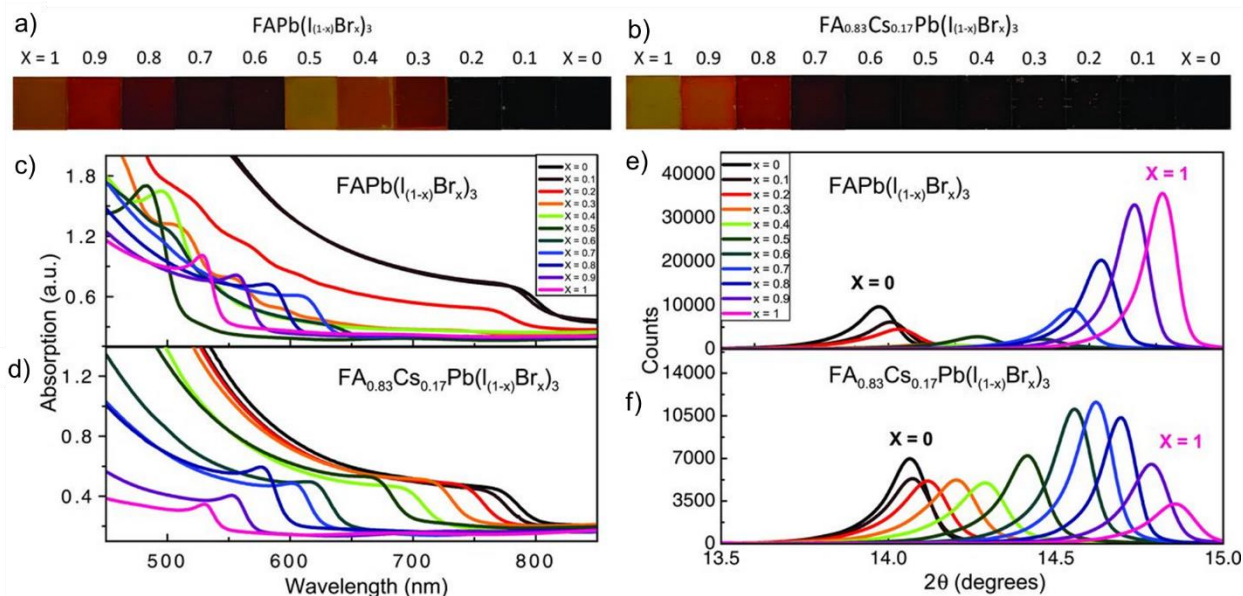


Figure 1.2: Tuning of the band-gap. Photographs of perovskite films with increasing Br content from $x = 0$ to 1 for (a) $\text{FAPb}(\text{I}_{1-x}\text{Br}_x)_3$ and (b) $\text{FA}_{0.83}\text{Cs}_{0.17}\text{Pb}(\text{I}_{1-x}\text{Br}_x)_3$. UV-Vis absorbance spectra of (c) $\text{FAPb}(\text{I}_{1-x}\text{Br}_x)_3$ and (d) $\text{FA}_{0.83}\text{Cs}_{0.17}\text{Pb}(\text{I}_{1-x}\text{Br}_x)_3$ films. XRD pattern of (e) $\text{FAPb}(\text{I}_{1-x}\text{Br}_x)_3$ and (f) $\text{FA}_{0.83}\text{Cs}_{0.17}\text{Pb}(\text{I}_{1-x}\text{Br}_x)_3$ films. (Reproduced from Ref. [19] with permission from The American Association for the Advancement of Science and Copyright Clearance Center)

1.2.1.3. B-Cation Variation

Partial or total replacement of lead with other metal cations, such as Sn^{2+} , Co^{2+} , Bi^{3+} , etc. in the perovskite system show great potential to tune the properties of the resulting perovskite materials. Moreover, this approach holds the promise to offer more environmentally friendly alternative perovskites. There are some efforts and investigations reported which use metal ions such as Sn^{2+} and Bi^{3+} to produce lead-free hybrid perovskites.^[57] Sn has shown to be a good candidate to substitute lead as it has analogous electronic structure and a similar ionic radius (1.35 Å) compared to Pb (1.49 Å). A lead-free MASnI_3 perovskite structure with pseudo-cubic symmetry group P4mm has been reported.^[58,59] Investigations on partial substitution of Pb by Sn show nonlinear band-gap reduction in $\text{CH}_3\text{NH}_3\text{Sn}_x\text{Pb}_{(1-x)}\text{I}_3$, extending absorption into the near-IR (1050 nm).^[60,61]

Partial replacement of Pb^{2+} with Sr^{2+} can enhance the charge carrier collection efficiency in devices.^[62] Xu et al. reported a perovskite with partial substituted 3d orbital transition metal cation (Co^{2+}) in Pb^{2+} sites. This led to an improved solar cell with PCE as high as 21 %.^[63] Moreover, Abdelhady et al. also reported improved conductivity and reduced optical band-gap by partial

substitution of Pb^{2+} with a very small amounts ($<0.1\%$ molar) of tri-valent Bi^{3+} .^[64,65] The partial substitution of Pb with other divalent cations, such as, Mn^{2+} , Cd^{2+} , or Ca^{2+} , has also been studied in MAPbI_3 powders, and optical investigations suggest that the electronic properties were affected.^[66,67]

1.2.1.4. Use of Additives in perovskite

The application of additives is a well-known technique to tune the structure and quality of the photoactive films in organic bulk-heterojunction solar cells.^[68,69] An analogous approach can be applied for the processing of perovskite absorbers to grow high-quality films, and to improve the photovoltaic performance. Most utilized additives help forming continuous perovskite films with big multi-crystalline grains by slowing-down the crystallization kinetics. There are a variety of additives which have been investigated for perovskite processing, such as solvent additives, polymer additives, metal halide additives or inorganic acid additives.^[70-73] The application of additives has proven to be effective in improving film morphology, charge transport, optical behavior, and to boost the overall performance of the PSCs.

A high quality $\text{CH}_3\text{NH}_3\text{PbI}_3$ film was formed by adding methylammonium iodide in isopropanol on top of PbI_2 using a two-step spin coating method.^[71,74] Using $\text{Pb}(\text{SCN})_2$ as an additive allows the preparation of good quality MAPbI_3 , mixed-halide mixed-cation and triple cation perovskites devices. Films with $\text{Pb}(\text{SCN})_2$ additive show improved grain size and surface smoothness, reduced pinholes and trap densities, as well as prolonged charge carrier lifetime and hence improved PCE and stability (see in Figure 1.3).^[75,76]

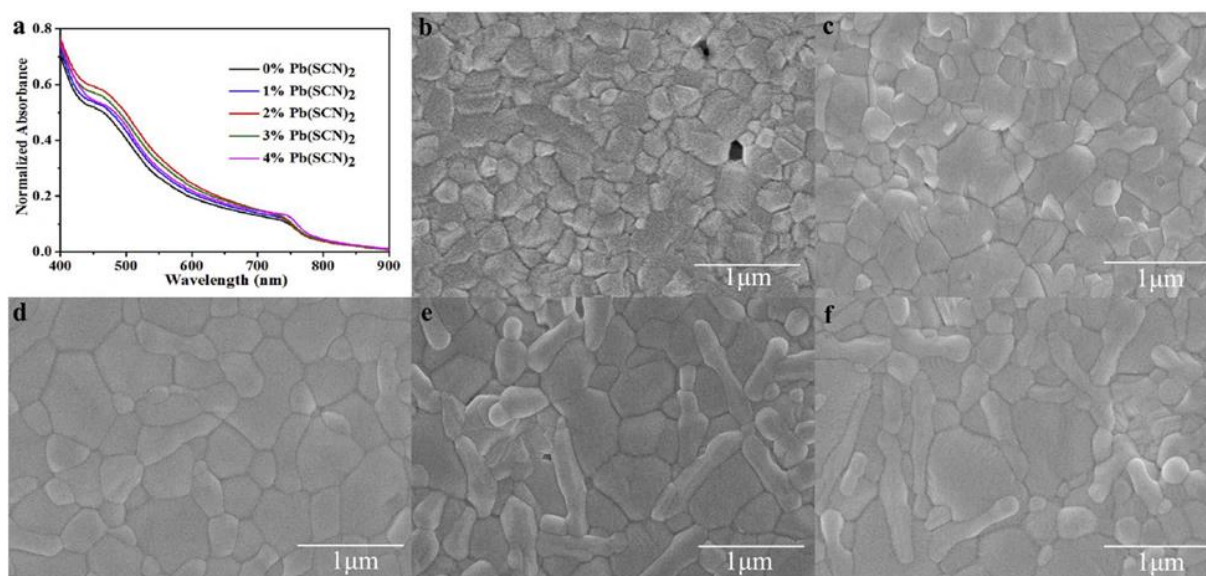


Figure 1.3. (a) UV-Vis absorption spectra of $\text{FA}_{0.8}\text{CS}_{0.2}\text{Pb}_{1.68}\text{Br}_{0.32}$ thin films with various $\text{Pb}(\text{SCN})_2$ contents deposited on FTO substrates. Topographic SEM images of $\text{FA}_{0.8}\text{CS}_{0.2}\text{Pb}_{1.68}\text{Br}_{0.32}$ films with various $\text{Pb}(\text{SCN})_2$ deposited on mesoporous TiO_2 layer: (b) 0 mol %, (c) 1 mol %, (d) 2 mol %, (e) 3 mol % and (f) 4 mol % composition. (Reproduced from Ref. [76] with permission from Elsevier, copyright 2017)

1.2.1.4. 2D/3D Perovskite designing

Another milestone was achieved in improving the performance and stability of PSCs by employing 2D/3D perovskite engineering. Two-dimensional perovskites (2D, also called Ruddlesden-Popper perovskite) can be obtained by incorporating large cations such as n-butylammonium (BA), benzylammonium, α -methylbenzylammonium, propylammonium, etc. Mixing different size A-cations yields 2D/3D perovskites which combine the stability of 2D perovskites and the good optical merits of 3D perovskites. The large A-cations occupy the space between highly crystalline anionic layers of 3D- ABX_3 perovskite, act as a moisture barrier, and give structural support for the perovskite.^[77-79]

1.2.2. Interface Engineering in Perovskite Solar Cells

Studies have shown that charge carrier recombination and accumulation at the interface between the semiconductor layer and the electrodes of an opto-electronic device are main contributors to performance loss.^[80-83] In PSCs, there are four important interfaces. The interface formed by the hole transporting layer and the photoactive perovskite layer, the interface between the perovskite layer and the electron transport layer (ETL), the interface formed by the HTL (inverted) or ETL (normal) and the front contact and interface between the ETL (inverted) or HTL (normal) and the back contact. Currently, the most efficient PSCs are based on a mesoporous electron transporting layer (ETL) deposited on the transparent front contact and coated with the photoactive perovskite layer, providing a large surface area for charge carrier extraction. However, this device configuration lacks technological simplicity and process compatibility, as the mesoporous ETL requires high processing temperatures, usually above 400 °C, which is not compatible with many transparent conductive oxides and substrate materials. Planar perovskite solar cells are proposed as an ideal alternative for the mesoporous system due to their simple fabrication processes.^[56] However, the charge extraction and performance of planar PSCs are highly dependent on the perovskite/ETL interface as well as the energy level alignment of ETL and perovskite material. Planar PSCs can be classified into inverted (p-i-n) and regular (n-i-p) configuration depending on the layer sequence in the device structure as shown in Figure 1.4.

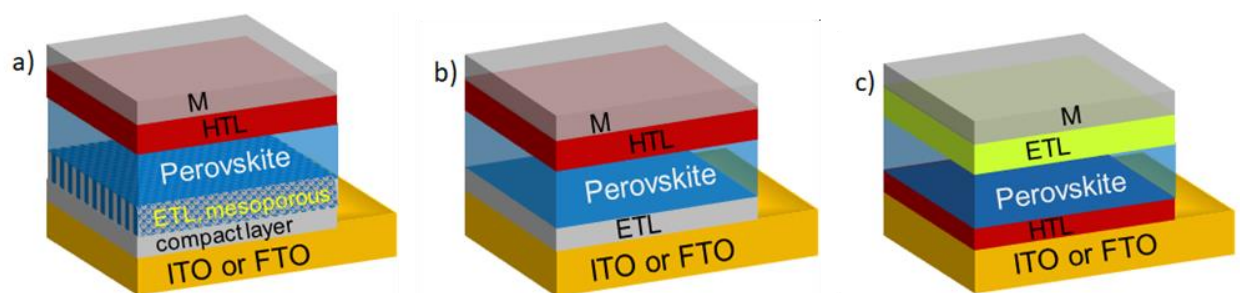


Figure 1.4. Diagrams of various structures employed in PSCs; (a) mesoporous and (b) normal (n-i-p) planar configuration, and (c) inverted (p-i-n) planar structure.^[84]

Upon illumination, the photons are absorbed by the photoactive perovskite layer resulting in the generation of charge carriers which is followed by transport of these carriers through the charge transport channels (ETL and HTL), and then extracted through cathodic and anodic interfaces (see Figure 1.5(a)). But this process can be affected by the presence of defects and trap-states across different interfaces which can act as recombination sites for charge carriers (see in Figure 1.5(b)). This diminishes the charge carrier extraction and reduces the device performance.^[80,84] Therefore, a careful designing of the surfaces and interfaces is crucial for effective charge carrier extraction processes.

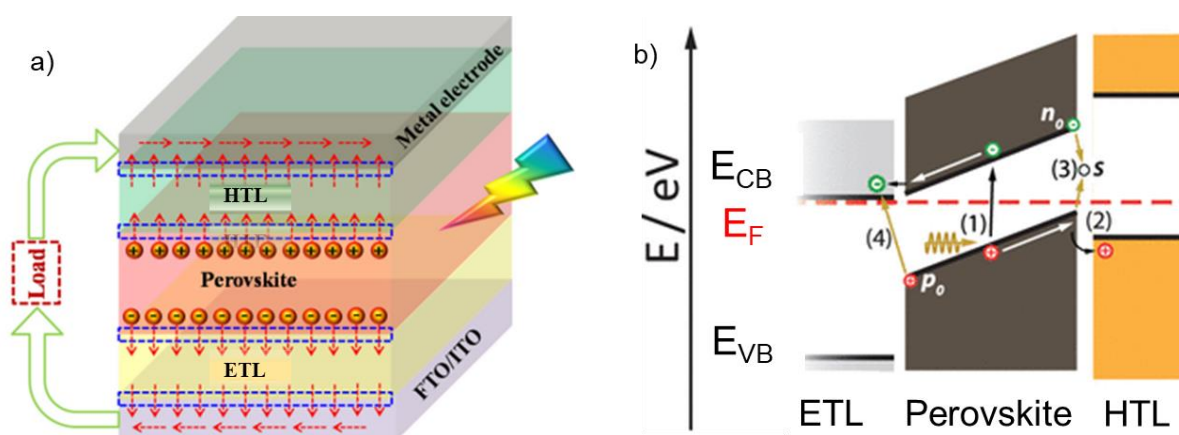


Figure 1.5. (a) Schematic diagram of charge transport across different interfaces in PSCs. (Reproduced from Ref. [84] with permission from Institute of Physics and the Physical Society, 1860254.) (b) Schematic depiction of interface related charge carrier loss mechanisms in the photovoltaic device: after photoexcitation (1), charge carrier transport to the contact interfaces occurs without significant losses; at the interface, carrier extraction can be impaired by (2) interfacial energy barriers due to inadequate band alignment, (3) defect-induced surface (interface) recombination, and (4) back recombination of extracted carriers, which reside in the interface region. (Reproduced from Ref. [80] with permission from American Chemical Society, Copyright 2019)

1.2.2.1. Hole Transport Layers (HTLs)

Hole transport layers in perovskite devices allow the extraction and transport of photogenerated holes, while blocking photogenerated electrons to the cathode contact. Due to this, HTLs sometimes referred as electron blocking layers. HTLs play a crucial role to reduce the charge recombination at the anode/perovskite interface and to modify the anodic work function to form a proper selective contact for the hole extraction. Moreover, the proper choice and energy level alignment at the HTL/perovskite interface has proven to play a detrimental role for the device photovoltage and overall performance.^[56,84,85,86]

For inverted (p-i-n configuration) devices, the photoactive film is deposited on top of the HTL, and the film growth and interfacial characteristics are highly dependent on the nature of the HTL/perovskite interface. The HTL should be stable towards the solvent used in the perovskite precursor solution and its surface chemistry should favor the growth of the perovskite film. In addition, as illumination is made from the HTL side, the layer should be transparent to avoid any

photon loss before reaching the photoactive layer. Some wide band-gap p-type polymers like poly(3,4-ethylenedioxythiophene):poly(styrene sulfonate) (PEDOT:PSS), poly(bis(4-phenyl)(2,4,6-trimethylphenyl)amine) (PTAA) and poly(p-phenylene) (PPP), as well as inorganic semiconductors such as NiO_x, CuSCN, V₂O₅ and MoO₃ have been used as HTLs in p-i-n PSCs.^[85-88]

PEDOT:PSS is one of the most extensively studied and most widely used hole transporting material. It shows good Fermi energy level alignment to a wide spectrum of photoactive layers and good hole mobility, enabling devices with good performance. However, due to its acidic characteristics and sensitivity to oxygen and moisture, PEDOT:PSS can cause long term stability issues in perovskite devices. Nickel oxide is another widely studied HTM. It consists of Ni(III) and Ni(IV) oxide impurities generally denoted as NiO_x, which has a high transmittance with a wide band-gap of 3.5 to 3.9 eV and high work function of about -5.3 eV.^[84,87] During this PhD study, PEDOT:PSS and NiO_x were used as hole transport layers to fabricate perovskite devices based on mixed halide perovskite and mixed-halide mixed-cation perovskite species.

1.2.2.2. Electron Transport Layers (ETLs)

The electron extraction and transport process at the cathode side of the PSCs are realized by using ETLs. The ETLs play crucial role to extract the photogenerated electrons and to avoid charge carrier recombination by blocking the hole transfer to the anode. ETLs are referred as hole blocking layers.^[85] TiO_x, ZnO, and SnO_x are some of the most commonly used and well studied n-type metal oxides, which are used as ETLs. However, the photocatalytic activity of TiO_x and thermal instability of ZnO trigger degradation of the photoactive layer and thus PSCs deposited directly on top of these oxides have shown less stability. However, interface modification at these oxides using self-assembled monolayers, inorganic materials, fullerene or its derivatives have proven to reduce the detrimental effects of these oxide layers and to improve the device performance.^[84,89]

In p-i-n (inverted) PSCs, [6,6]-phenyl-C₆₁ butyric acid methyl ester (PCBM) is the most commonly used ETL. It plays a vital role by passivating trap-states and by protecting the metal electrode from direct contact with the corrosive perovskite material. When an additional layer needs to be deposited, PCBM can also protect the underlying perovskite film from direct exposure to the processing solvents.^[90,91] However, forming an ohmic contact and the mismatch between the lowest unoccupied molecular orbital (LUMO) of PCBM and the metal electrode can reduce the device efficiency.^[92-94] The barrier height formed between the Fermi level of the metal electrode and the LUMO level of PCBM causes charge carrier extraction resistance and hence reduces the electron extraction and overall performance of the device.^[84,93] To overcome this issue and improve the charge carrier extraction across the interface between PCBM and the metal contact, many efforts have been made. Introducing an additional buffer layer between the ETL and the

back contact electrode proved to improve the performance and stability of devices. Different materials, including inorganic compounds such as TiO_x , ZnO , LiF , MgF_2 , $\text{Cr/Cr}_2\text{O}_3$, etc., as well as organic materials such as poly(2-ethyl-2-oxazoline) (PEOz), 2,9-dimethyl-4,7-diphenyl-1,10-phenanthroline (BCP) and fullerene C_{60} derivatives have been reported to be used as a buffer layer between PCBM and the metal electrode.^[94-97] Chen et al. showed the enhancement of charge carrier extraction kinetics, and improvement of open-circuit voltage, fill factor and other photovoltaic parameters in the presence of poly(2-ethyl-2-oxazoline) (PEOz) interlayer between PCBM and Ag electrode.^[94] P. Decampo et al. demonstrated the possibility of using TiO_x as an interlayer in inverted mixed halide based PSCs.^[98]

1.2.2.3. Photoactive Perovskite Film Morphology

The surfaces and interfacial defects of the photoactive films are considered to be the main sites for non-radiative charge carrier recombination as schematically depicted in Figure 1.5(b). The surface termination of perovskite films can be either the cation moiety or metal halide unit depending on the composition and processing condition. This has a direct impact on the physics and chemistry of surfaces (like reactivity, surface potential, electronic structure and stability). There are different deposition techniques and experimental approaches used to process perovskite films. One-step solution-based deposition, two-step sequential deposition based on solution processing, one-step and two-step vacuum depositions, and vapor assisted solution processing methods are techniques, which are widely used in the fabrication of perovskite layers.^[16,99,100] These deposition techniques control not only the bulk crystal quality of the perovskite film but also the surface morphology, composition, as well as chemical and electrical properties. Many other techniques have been employed aiming to improve the morphology and quality of the films, such as solvent treatment (typically with DMSO, DMF, or isopropanol), incorporation of additives (liquid and/or solid), and in-situ anti-solvent quenching during film deposition.^[56,72,101,102]

Furthermore, controlling the stoichiometric ratio between the divalent metal cations (B^{2+}), the monovalent organic and/or inorganic cation (A^+) and the halides (X^-) has a significant influence on the morphology and surface termination chemistry of perovskite films, and hence, the performance of the perovskite devices.^[103-107] Small changes in the stoichiometry of the precursor solution can have a significant effect on the properties (surface composition, photoluminescence, crystallinity, energetic disorder, etc.) of perovskite films and hence, on the performance and stability of the devices.^[103,107,108] In this dissertation a solvent additive technique was applied to modify the surface morphology and improve the film quality of mixed halide perovskite. The results are presented in section 3.3.

In this PhD research different organic and inorganic transport layers were applied to inverted (p-i-n) perovskite solar cells, and studied the charge carrier dynamics at different interfaces and

the effects on the performance and stability of the devices. Attempts were made to optimize the interfaces, thickness, and composition of different layers for improved performance and reduced hysteretic behavior in devices.

Thorough investigations were performed by applying different optical, electronic and microscopic characterization techniques to gain a deeper understanding of interfacial dynamics, surface chemistry, and surface defects. Thin layers of low temperature processed titanium oxide (TiO_x) or of polyphosphazene derivatives (PPz) were used as a buffer layer between the PCBM ETL and back metal electrodes to modify the ETL/metal interface and to improve the device efficiency and stability. Furthermore, acetylacetone was used as a solvent additive, aiming to modify the film growth and surface morphology of the photoactive mixed halide perovskite.

The effects of different ETLs and solvent engineering on the charge carrier extraction processes in perovskite devices are presented in section 3. In section 3.1 a low temperature processed titanium oxide (TiO_x) is applied as a buffer layer between the PCBM ETL and back contact electrodes. The second sub-section (3.2) presents the very first study on polyphosphazene derivatives (PPz) used as an interlayer between the PCBM ETL and back metal contact. Section 3.3 presents the role of solvent engineering to modify the film growth and surface morphology of perovskite films. In the last section (3.4) electrical characterization; impedance spectroscopy and maximum-power-point tracking were applied to study the physical and chemical dynamics in the bulk and interfaces of PSCs under continuous operation.

2. Experimental Section

2.1. Materials

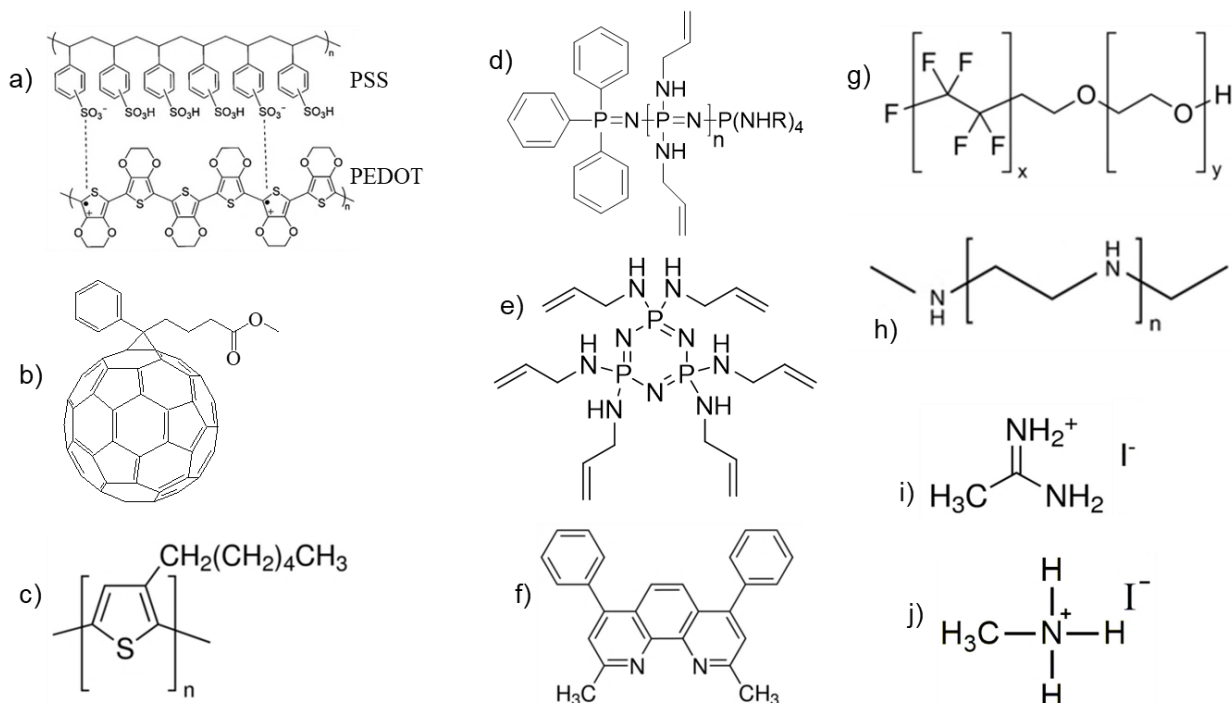


Figure 2.1: Chemical structure of molecules used: a) poly(3,4-ethylenedioxythiophene) polystyrene sulfonate, b) [6,6]-phenyl-C₆₁-butyric acid methyl ester, c) poly(3-hexylthiophene-2,5-diyl), d) linear poly[bis(allylamino)phosphazene] ($n = 5$ or $n = 50$) where $R =$ allyl, e) allylamino cyclic phosphazene, f) Bathocuproine (BCP), g) Zonyl®FSO fluorosurfactant, h) polyethyleneimine, i) FAI and j) methylammonium iodide.

To accomplish this study patterned indium tin oxide (ITO) coated glass substrates ($15 \Omega/\text{cm}^2$), lead iodide (PbI_2 , Sigma Aldrich, 99.9 %), lead bromide (PbBr_2 , Sigma Aldrich, 99.99 %), lead chloride (PbCl_2 , Sigma Aldrich, 99.99 %), [6,6]-phenyl-C₆₁-butyric acid methyl ester (PCBM, Solenne BV), various poly(3,4-ethylenedioxythiophene) polystyrene sulfonate (PEDOT:PSS) formulations (Clevios PH 1000; Clevios F HC Solar, SCA 418-12; Clevios P VP.AI 4083; Clevios HTL Solar, SCA388-6), Zonyl®FS-300 fluorosurfactant (40 % in H_2O , Fluka), nickel chloride hexahydrate ($\text{NiCl}_2 \cdot 6\text{H}_2\text{O}$, Sigma Aldrich, 99.9 %), cesium iodide (CsI, Sigma Aldrich, 99.99 %), sodium hydroxide (NaOH, Sigma Aldrich, ≥ 98 %), hydroiodic acid (HI, 57 wt % in H_2O), hydrobromic acid (HBr, >48 wt % in H_2O), formamidinium acetate salt ($\text{CH}_5\text{N}_2\text{CH}_3\text{COO}$, Merck, 99 %), methylamine (CH_3NH_2 , Aldrich, 33 wt % in absolute ethanol), poly(3-hexylthiophene-2,5-diyl) (P3HT, RR, Rieke), polyethyleneimine (PEI, Aldrich), titanium oxide (TiO_x) sol-gel, polyphosphazene (PPz), 2,9-dimethyl-4,7-diphenyl-1,10-phenanthroline (Bathocuproine, BCP, Sigma Aldrich, 96 %), isopropanol, isopropanol, *N,N*-dimethylformamide (DMF, anhydrous, Sigma Aldrich), dimethylsulfoxide (DMSO, Anal. R. VWR chemicals, 99.5 %), acetone, ethanol, and chlorobenzene were used.

Methylammonium bromide (MABr, $\text{CH}_3\text{NH}_3\text{Br}$), methylammonium iodide (MAI, $\text{CH}_3\text{NH}_3\text{I}$) and formamidinium iodide (FAI, $\text{CH}(\text{NH}_2)_2\text{I}$) were sensitized as mentioned below. PTFE syringe filters (VWR, $0.45\ \mu\text{m}$) were used to filter perovskite precursor solutions, NiO_x colloidal solution and PEDOT:PSS (Clevios F HC Solar and SCA418-12). Regenerated cellulose (Sartorius RC, $0.45\ \mu\text{m}$) syringe filters were used to filter PEDOT:PSS (Clevios PH1000).

Titanium diisopropoxide bis(acetylacetonate) ($[(\text{CH}_3)_2\text{CHO}]_2\text{Ti}(\text{C}_5\text{H}_7\text{O}_2)_2$), Sigma Aldrich, 99.9 %), 2-methoxyethanol ($\text{CH}_3\text{OCH}_2\text{CH}_2\text{OH}$, Sigma Aldrich, 99.9 %) and ethanolamine ($\text{H}_2\text{NCH}_2\text{CH}_2\text{OH}$, Sigma Aldrich, 99 %) were used to synthesize TiO_x sol-gel.

Polyphosphazene derivatives namely, linear poly[bis(allylamino)phosphazene] ($n \sim 5$ and $n \sim 50$) and allylamino cyclic phosphazene (see Figure 2.1(d&e)) were synthesized according to already reported literature^[109-111] by Vanessa Poscher at the Institute of Polymer Chemistry, Johannes Kepler University. To synthesize PPz derivatives anhydrous diethylether (p.a, VWR), phosphorus trichloride (PCl_3), allylamine ($\text{C}_3\text{H}_7\text{N}$), lithium bis(trimethylsilyl)amide ($\text{LiN}(\text{SiMe}_3)_2$, 97 %), dichlorotriphenylphosphorane (Ph_3Cl_2 , 95 %) and hexachlorocyclotriphosphazene (99 %) were purchased from Sigma Aldrich, and thionyl chloride (SOCl_2 , 99 %, Fluka), anhydrous dichloromethane (DCM, 99.7 %) and tetrahydrofuran (THF, 99.8 %, Alfa Assar), triethylamine (NEt_3 , $\geq 99\%$) and ethanol (p.a) were purchased from Merck. Deuterated chloroform (CDCl_3 , 99.8 %, Sigma Aldrich) and methanol (MeOD-d_4) ($> 99.8\%$, Fluorochem) were used for NMR experiments.

2.1.1. Synthesis of Organic Halides

To synthesize formamidinium iodide ($\text{CH}(\text{NH}_2)_2\text{I}$), hydroiodic acid was added in a round-bottom flask followed by addition of an equimolar amount of formamidinium acetate salt under continuous stirring while the mixture was immersed in an ice bath to keep the reaction temperature at $0\ ^\circ\text{C}$. The reaction mixture was left stirring inside the ice bath for 2 hrs. The solvent was then dried using a rotary evaporator. The resulting crystals were re-dissolved in a small amount of ethanol and re-precipitated by adding diethyl ether, and decanted. Washing with diethyl ether was repeated until clean white crystals were obtained. Crystals were then filtered-off with a Buchner funnel, and transferred to a round bottom flask followed by freeze drying. Finally, the dried, white crystal powder of FAI was transferred into a vial and kept in a nitrogen glove box. Methylamine and hydroiodic acid were used in 1:1 molar ratio to synthesize methylammonium iodide ($\text{CH}_3\text{NH}_3\text{I}$) following the same synthesis procedure used for FAI. The same procedure was applied to synthesize methylammonium bromide ($\text{CH}_3\text{NH}_3\text{Br}$) using methylamine and hydrobromic acid.

2.1.2. Synthesis of Nickel Oxide (NiO_x) Nanoparticles

Nickel oxide nanoparticles were synthesized following the procedure described by Young et al.^[112] About 2 % (wt/v) of NiO_x powder was mixed with deionized water (20 mg/mL), and treated with

ultrasound sonication (UP50H, 50 Watt, 30 kHz frequency) five to six times for about five minutes, in between, the NiO_x water mix was kept in an ultra-sonication bath to avoid aggregation. The solution was then filtered through 0.45 μm pore size filter before use. Figure 2.2(a) shows the typical topographic scanning electron microscopy (SEM) image of NiO_x film deposited on ITO coated glass substrate at 4000 rpm for 15 s and 5000 rpm for 15 s followed by heating at 140 °C for 20 min. Figure 2.2(b) shows the statistical grain-size histogram of NiO_x film in Figure 2.2(a). Though the thickness of the NiO_x thin film is ≤50 nm, the average horizontal grain-size of the surface particles is in the range 100 nm. This could be due to the aggregation of neighboring NiO_x particles during film formation.

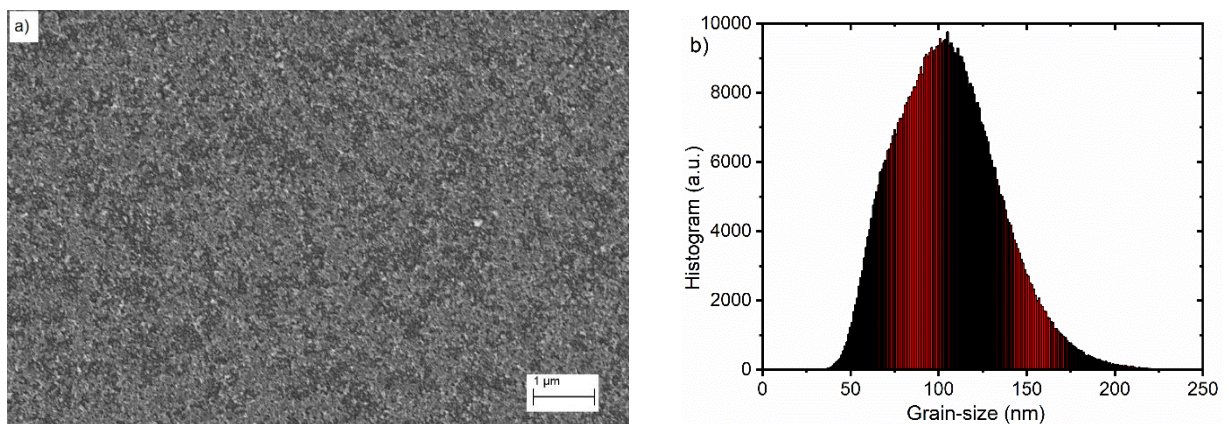


Figure 2.2: (a) Topographic SEM image, and (b) statistical grain-size histogram of a NiO_x film deposited on to of an indium tin oxide coated glass substrate.

2.1.3. Synthesis of TiO_x Sol-gel

The sol-gel TiO_x synthesis was done following the procedure reported by S. H. Park et al.^[113] A three-neck flask (100 mL) was used to mix the precursor materials. The flask was first dried at about 120 °C while providing a flow of nitrogen (N₂) to remove any moisture. Then, a 5 mL of titanium (IV) isopropoxide (Ti[OCH(CH₃)₂]₄), 20 mL of 2-methoxyethanol (CH₃OCH₂CH₂OH) and 2 mL of ethanolamine (H₂NCH₂CH₂OH) were sequentially injected into the three-neck flask at room-temperature. The mixture was stirred for 60 min at room temperature and for 60 min at 80 °C (in silicon oil bath) while maintaining N₂ atmosphere. Then, the temperature was increased to 120 °C for 60 min with continuous stirring to distill-off low boiling solvents. By this, the solution transformed into a low-density gel with dark wine color. The mixture was allowed to cool down to room temperature, and into which isopropyl alcohol (IPA, 10 mL) was added to prepare the TiO_x sol-gel precursor solution. The precursor solution was further diluted with IPA (1:150 (v/v) ratio) to obtain the final TiO_x sol-gel formulation suited for device processing.

2.2. Preparation of the Perovskite Precursors

2.2.1. Mixed-Halide Perovskite ($\text{CH}_3\text{NH}_3\text{PbI}_{3-x}\text{Cl}_x$)

To prepare $\text{MAPbI}_{3-x}\text{Cl}_x$ perovskite precursor solutions, lead halides and methylammonium halide were dissolved in defined molar ratios. An established formulation uses PbI_2 , PbCl_2 , and MAI in a molar ratio of 1:1:4, respectively, dissolved in a specific volume of DMF to yield Pb concentration of 0.88 M.^[152] $\text{MAPbI}_{3-x}\text{Cl}_x$ perovskite solutions with acetylacetone (AA) additive were prepared by using the same molar ratio of lead halides and methylammonium halide as described above, and were dissolved in DMF containing different volume percent compositions (5, 10, 15 and 20 (v/v)%) of acetylacetone (AA) additive. The mixtures were stirred overnight at about 45 °C, and filtered using a 0.45 μm pore-size PTFE filter before use.

2.2.2. Mixed-Cation Mixed-Halide Perovskite ($\text{CsFAMAPbI}_{3-x}\text{Br}_x$)

Mixed-cation mixed-halide perovskite ($\text{Cs}_{0.05}(\text{FA}_{0.83}\text{MA}_{0.17})_{0.95}\text{PbI}_{3-x}\text{Br}_x$) solution was prepared by mixing PbI_2 (1.1 M), FAI (1.0 M), MABr (0.2 M) and PbBr_2 (0.2 M) in dry N,N-dimethylformamide and dimethylsulfoxide solvent mixtures (4:1 (v/v) ratio) followed by stirring at 45 °C.^[32,35] After the mixture is dissolved and stirred for about 30 min, 5 (v/v)% ratio of CsI from 1.5 M stock solution (in DMSO) was added into the mixture. The stirring was continued overnight at the same temperature. The solution was filtered through a PTFE syringe filter (0.45 μm) before use.

2.3. Device Fabrication

Glass substrates with sputtered indium tin oxide (ITO) were sequentially sonicated in detergent, deionized water, acetone, and isopropanol (IPA). To deposit a thin layer of nickel oxide (NiO_x) nanoparticles HTL, about 20 mg/mL of NiO_x particles in water were cracked using an ultrasound sonicator (UP50H, 50 Watt, frequency 30 kHz), followed by filtration through 0.45 μm pore-size polytetrafluoroethylene (PTFE) syringe filter. Then, NiO_x was deposited by spin-coating (4000 rpm for 15 s and 5000 rpm for 15 s) onto the ITO-coated substrates and annealed at 140 °C for 20 min, which resulted in 40 to 50 nm thick NiO_x thin-films. For the deposition of perovskite films and further processing, the substrates were transferred into the glove box.

PEDOT:PSS (Clevios F HC or Clevios PH1000) based hole transporting layers were deposited by spin-coating (2500 rpm for 45 s) and dried at 120 °C for 15 min which was followed by IPA washing via spin-coating at 4000 rpm for 15 s and heating once more at 120 °C for 15 min. The substrates with HTL were transferred into the glove box to deposit mixed-cation mixed-halide perovskite films, while mixed-halide perovskites were processed in ambient air.

The mixed-cation mixed-halide perovskite ($\text{CsFAMAPbI}_{3-x}\text{Br}_x$) solution was deposited on top of the HTL using a two-step spin-coating process: first is at 1500 rpm for 10 s with ramp step 9 and the

second-step at 6000 rpm for 30 s with ramp step 2. During the second-step anti-solvent quenching was done by gently dropping about 200 μl of chlorobenzene starting at 23rd s of the spin-coating process for about 3 s. The film was then annealed at 100 °C for 60 mins. After annealing, the films were cooled to room temperature, and 2 % (wt/v) of PCBM dissolved in a mixture of chlorobenzene and chloroform solvents (50:50 volume ratio) was spin-coated on top of the perovskite film. Diluted TiO_x sol-gel solution was spin-coated on top of PCBM at 4000 rpm for 30 s followed by annealing at 110 °C for about 5 min in ambient air. For devices with PPz interlayer, PPz dissolved in IPA (0.25 mg/mL, 0.5 mg/mL, 1 mg/mL, 2 mg/mL and 5 mg/mL) was spin-coated at 5000 rpm for 30 s followed by annealing at 102 °C for about 3 min inside the glove-box. Finally devices were finalized by thermal evaporation of metal electrode (Al, Cu or Ag) through a shadow mask at a pressure of about 10^{-6} mbar.

Mixed-halide perovskite ($\text{MAPbI}_{3-x}\text{Cl}_x$) devices were fabricated from perovskite precursor solutions with and without AA additive. The active layers were spin-coated at 1000 rpm for 17 s and 2000 rpm for 5 s on top of the hole transporting layer, PEDOT:PSS (Clevios PH1000). The transformation of perovskite films were completed via annealing at 115 °C for about 30 min. $\text{MAPbI}_{3-x}\text{Cl}_x$ films with AA additive were also spin-coated at two different spin-coating speeds to deposit thinner films, one at 1500 rpm for 30 s and the other ones at 2000 rpm for 30 s. The films were thermally treated similarly at 115 °C for about 30 min. After the films cooled to room temperature; 2 % (wt/v) of PCBM dissolved in a mixture of chlorobenzene and chloroform (50:50 volume ratio) was spin-coated on top of the perovskite film. For optimized sample devices, TiO_x sol-gel was spin-coated on top of PCBM at 5000 rpm for 30 s and annealed at 110 °C for 10 min. Finally the inverted PSC fabrication was finished by thermal evaporation of 110 nm Al back contacts.

Bulk-heterojunction solar cells (BHJSCs) based on a P3HT:PCBM photoactive blend were fabricated in n-i-p configuration. A thin layer of PPz5 (1 mg/mL in IPA) or polyethyleneimine (PEI, 0.2 mg/mL in n-butanol) were spin-coated on top of cleaned ITO (5000 rpm for 30 s with ramp: 1000 rpm/s). To check the combined effect of PEI and PPz5, PPz5 was spin-coated on top of PEI (5000 rpm for 30 s with ramp: 2500 rpm/s). All films were annealed at 105 °C for 5 min. The photoactive blend solution was prepared by dissolving P3HT:PCBM (1:1 weight ratio) in chlorobenzene (20 mg/mL) under stirring at 60 °C. The solution was spin-coated on top of the buffer layer (1500 rpm for 20 s with ramp: 750 rpm/s and at 2000 rpm for 30 s with ramp: 1000 rpm/s) and annealed at 110 °C for 5 min. In a last step, 10 nm of MoO_x and 100 nm of Ag were thermally deposited through a shadow mask by thermal evaporation at about 10^{-6} mbar pressure.

Devices with p-i-n BHJSC architecture were fabricated as well using poly(3,4-ethylenedioxythiophene) polystyrene sulfonate (PEDOT:PSS) or a thin layer of PPz5 as a hole

transport layer. PPz5 was spin-coated and thermally treated as mentioned above. PEDOT:PSS was spin-coated (1000 rpm for 3 s with ramp: 500 rpm/s and at 4000 rpm with ramp: 2000 rpm/s for 30 s) and annealed at 120 °C for 15 min. P3HT:PCBM solution was spin-coated and thermally treated in the same way described for the n-i-p device stack. Solar cells were finished via thermal deposition of a thin anode interlayer of LiF (0.8 nm), followed by 110 nm of aluminum contacts.

2.4. Characterization Techniques

2.4.1. Profilometer

To measure the thickness of the photoactive perovskite layers a profilometer (DektakXT, BRUKER) was used (Figure 2.3). The thickness of mixed-halide perovskite and mixed-cation mixed-halide perovskite films deposited on oxygen plasma treated glass substrates at different spin-coating speeds were measured. The profilometer was also used to measure the thickness of different HTLs (NiO_x and PEDOT: PSS), ETLs (PCBM), and different buffer layers (TiO_x , PPz). Thin films of PEDOT:PSS, NiO_x and TiO_x were deposited on glass substrates under different spin-coating parameters and measured. Thin-films of PPz5 based on 0.25, 0.5, 1, 2, and 5 mg/mL concentrations (in isopropanol) were deposited on glass substrates using identical spin-coating parameters, and the thicknesses were measured.

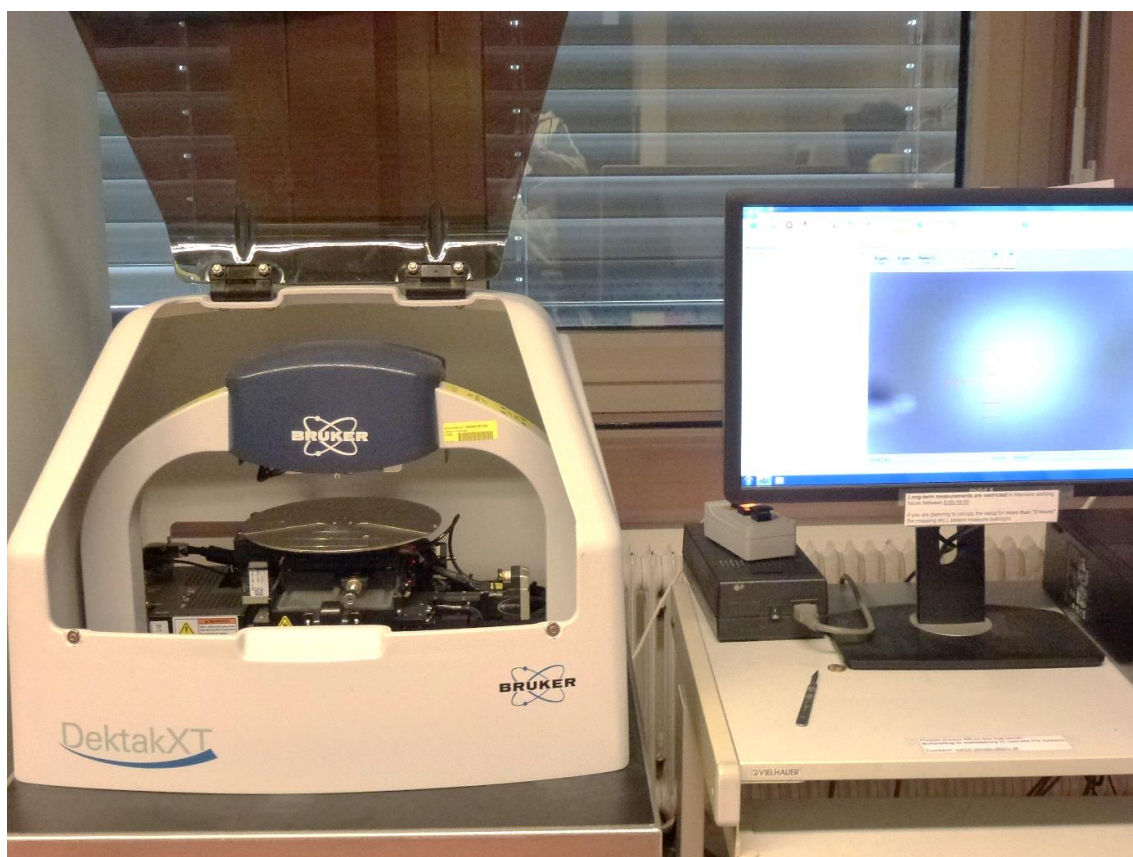


Figure 2.3: Image of BRUKER DektakXT profilometer.

2.4.2. Optical Spectroscopy

A UV-Vis-NIR spectrophotometer (Perkin Elmer Lambda 1050) was used to measure the absorbance, transmittance and reflectance of sample films, specifically, perovskite thin films and PPz5 thin layers. The instrument uses a tungsten and a deuterium lamp as light sources which provide a wide range of wavelengths from 150 to 3100 nm.

To measure the UV-Vis absorption and transmittance of mixed-halide perovskite ($\text{MAPbI}_{3-x}\text{Cl}_x$) thin-films, prepared with and without acetylacetone additive, precursor solutions were processed on glass substrates. Spectra were recorded in the presence of an identical glass substrate on the reference side.

The optical response of PPz5 thin-films was measured to determine the approximate band-gap of the polymer. PPz5 dissolved in IPA (10 mg/mL) was spin-coated at 1000 rpm for 30 s followed by drying at 100 °C for 5 min. Then, the UV-Vis absorption spectrum was measured.

2.4.2.1. Photoluminescence and Electroluminescence

Photoluminescence (PL) and electroluminescence (EL) measurements were conducted for various samples. To measure the PL, different laser sources such as a COHERENT OBIS laser (532 nm), a COHERENT OBIS laser (488 nm), and a VIOFLAME 405 nm laser (COHERENT UV GaN-based, 25 mW) were used to excite samples. The photons emitted from samples were collected by an integrating sphere (HAMAMATSU PHOTONICS, A9924-06) and transferred by fiber optics to a Shamrock SR-303i monochromator and an Andor™ iDus Si-CCD detector.

To study the effect of a TiO_x interlayer, the PL of mixed-cation mixed-halide perovskite films, perovskite films covered with PCBM (PVS/PCBM) and films with TiO_x on top of PCBM (PVS/PCBM/ TiO_x) were measured using a VIOFLAME 405 nm laser excitation.

The room temperature PL of mixed-cation mixed-halide perovskite (PVS) films, PVS coated with PCBM (PVS/PCBM) and PVS/PCBM films covered with PPz5 (PVS/PCBM/PPz5) was measured under COHERENT OBIS laser (532 nm) excitation.

$\text{MAPbI}_{3-x}\text{Cl}_x$ perovskite solutions, with and without acetylacetone additive, were deposited on glass, and on glass substrates covered with PEDOT:PSS, using the same spin-coating parameters used for the solar cell fabrication. Films were excited under COHERENT OBIS laser (532 nm), and the PL was measured using a Shamrock SR-303i monochromator and an Andor™ iDus Si-CCD detector.

The bias dependent PL of mixed-cation mixed-halide perovskite solar cells with and without PPz5 interlayer were measured using the same PL set-up. The sample device was connected to the Keithley-2400 source meter and directly aligned to the integrated sphere. Solar cells were

operated at different applied potential while excited by a laser source. The photoluminescence was recorded as a function of the applied voltage and wavelength.

The electroluminescence of perovskite solar cells was measured using the same monochromator and detector utilized in the for PL signal recordings. A Keithley-2400 source meter was used to apply voltage and to measure the resulting currents under different voltage bias. The radiative emission of the device was focused into an integration sphere and directed to a Shamrock SR-303i monochromator and an Andor™ iDus Si-CCD detector.

2.4.2.2. Photoluminescence Decay (PLD)

The photoluminescence decay of different sample films was measured by using a Nd:YAG laser (Spit light Compact 100), emitting at 532 nm with a pulse length of ~10 ns to excite the samples, and a Shamrock (SR-303i-A) monochromator equipped with an intensified charge-coupled device camera (Andor iStar DH320T-18U-73; gate step: 2.5 ns; gate width: 2.5 ns). The instrumental set-up is shown in Figure 2.4.



Figure 2.4: Photoluminescence (PL) and photoluminescence decay (PLD) set-up.

2.4.3. X-ray Diffraction Spectroscopy

In this PhD thesis work, a BRUKER D8 X-ray powder diffractometer (shown in Figure 2.5) operated at the Applied Physics Institute, Johannes Kepler University Linz was used to characterize mixed-

halide perovskite films and mixed-cation mixed-halide perovskite films deposited on amorphous glass substrates. It is equipped with a Copper K- α radiation source providing a wavelength of 1.54 Å.

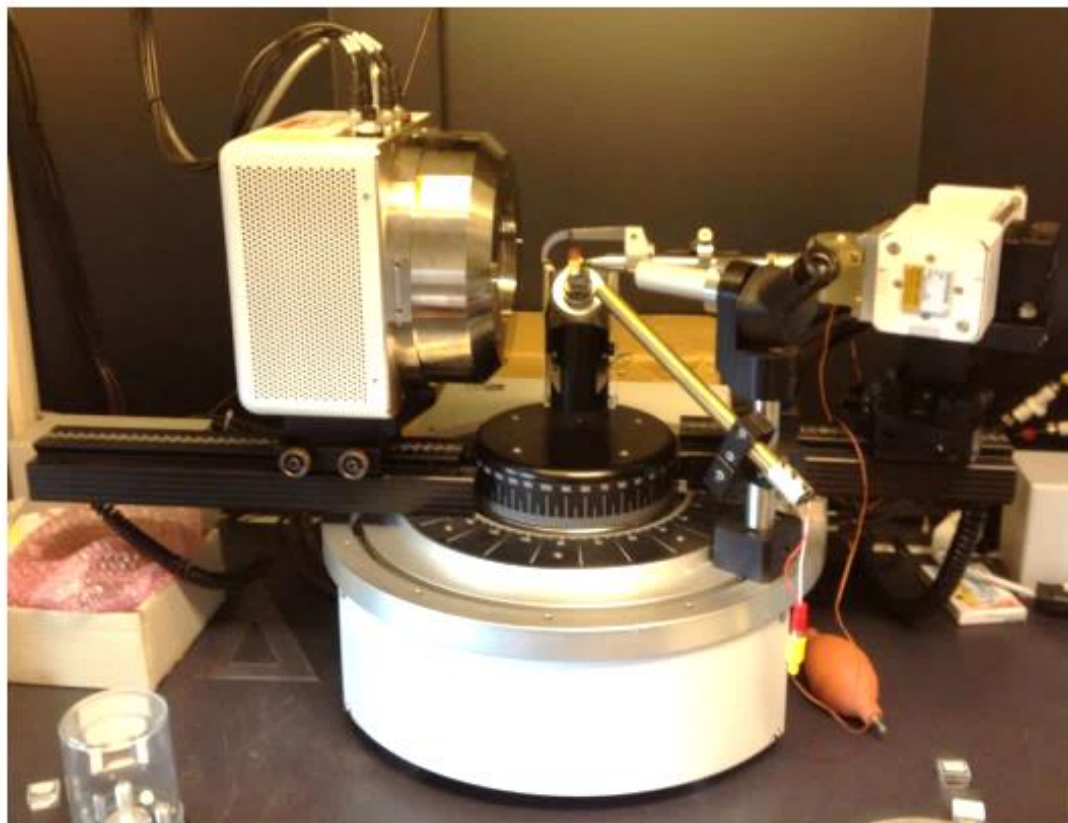


Figure 2.5: Image of BRUKER D8 X-ray powder diffractometer with Cu K α radiation source.

2.4.4. Microscopy

2.4.4.1. Atomic Force Microscopy

Tapping mode atomic force microscopy (AFM, Bruker Innova) shown in Figure 2.6 was used to characterize the surface profile of perovskite films deposited on different substrates, NiO_x films deposited on ITO coated glass substrates, perovskite films, PCBM films covering perovskite films, TiO_x thin-films on top of perovskite/PCBM film stacks, and PPz5 thin-layers deposited on perovskite/PCBM film stacks.



Figure 2.6: Image of an atomic force microscope (AFM, Bruker Innova).

2.4.4.2. Scanning Electron Microscopy (SEM)

Scanning electron microscopy (SEM, ZEISS 1540 XB cross-beam scanning microscope equipped with a focused ion-beam (FIB) unit) was used to characterize the topographic morphology of perovskite films, and perovskite films covered with different ET materials (Figure 2.7). Cross-section SEM imaging of perovskite solar cells was conducted as well.



Figure 2.7: Image of a scanning electron microscope (SEM, ZEISS 1540 XB cross-beam scanning microscope equipped with a focused ion-beam (FIB) unit).

2.4.5. Optoelectronic Characterization

2.4.5.1. Photocurrent Density-Voltage (J-V) Curves

As solar cells are electric devices, a current-voltage scan is the most commonly used characterization technique. Most of the photovoltaic parameters such as fill factor (FF), power conversion efficiency (PCE), open circuit voltage (V_{OC}), short circuit current (J_{SC}) and hysteresis of the solar cell are extracted from the current-voltage characteristic.

The characteristic photocurrent density-voltage (J-V) response of perovskite devices was measured with a Keithley-2401 source meter. A LOT-Quantum Design solar simulator (LS0821) with a 1600 W xenon lamp, providing AM1.5 global spectrum, was used for radiation source. The intensity of the solar simulator was adjusted using a calibrated silicon reference diode.

2.4.5.2. External Quantum Efficiency (EQE)

External quantum efficiency is also called incident-photon-to-current conversion efficiency (IPCE) which is a measure of device efficiency to convert incident photons of certain wavelength into current. The EQE of PSCs was measured by using an optical setup consisting of a lock-in amplifier (SR830, Stanford Research Systems) and a Jaissle 1002 potentiostat functioning as a preamplifier. Devices were illuminated with light from a xenon lamp passing through a monochromator (Oriel Cornerstone). A filter wheel holding long-pass filters and a mechanical chopper were mounted between the xenon lamp and the monochromator. Chopping frequencies in the range of 10 to 200 Hz were chosen. A calibrated silicon diode (Hamamatsu S2281) was used as a reference for the light intensity at each wavelength.

2.4.5.3. Maximum Power Point (MPP) Tracking

To study the steady-state stability of PSCs, maximum power point (MPP) tracking of encapsulated solar cells was measured in ambient air as well as in the glove box (with oxygen level in the range of 0.1 to 10 ppm) under AM1.5 global spectrum illumination with continuous ventilation to keep the temperature of the devices close to room temperature. The J-V characteristics of perovskite devices were measured before and after MPP tracking. ATLAS solar simulator (SoTest 1200) was used for ambient measurements and a LOT-Quantum Design solar simulator (LS0821), constructed from a 1600 W xenon lamp, was used for the glove box measurements.

2.4.5.4. Space-Charge-Limited Current (SCLC)

Space-charge-limited current (SCLC) is an important technique that is applicable to examine the mobility of charge carriers and the density and energetics of trap-states in electronic devices (e.g., solar cells, light-emitting diodes). SCLC measurement involves the application of a sufficiently large voltage across the semiconductor through Ohmic contacts. Charges are injected into the

material and generate a current flow. If there are defect-sites in the semiconductor, some of the charges will be captured and thus reduce the density of free charges injected. The resulting current at a given voltage becomes limited by the space-charge effect and hence the defect density in the material can be derived from the space-charge-injected current region of J-V curve.^[114]

Current density-voltage (J-V) curves measured by SCLC method comprise three regimes as schematically shown in Figure 2.8, the Ohmic response regime at a lower bias (cyan line), the space-charge-limited current regime (orange line) and the intermediate regime (green line). At lower bias, the defects are partially filled, and the current is linearly related to the voltage applied ($I \propto V$). The intermediate regime is called the trap-space-charge region, which is identified via its dramatic increase of the current injection when all the defects are filled. The trap-density in the device can be estimated from this regime. The onset of the trap-filled limit voltage (V_{TFL}) is directly related to the trap density (N_t) as follow.^[13,115,116]

$$V_{TFE} = \frac{eN_t d}{2\epsilon_r \epsilon_0} \quad 2.1$$

Where ϵ_0 is the vacuum permittivity (8.854×10^{-12} F/m), ϵ_r is the dielectric constant of the perovskite, and d-represents the thickness of the perovskite layer. The third regime is called the trap-free SCLC regime from which the charge mobility can be calculated at high bias using equation 2.2.^[116,117]

$$J = \frac{9}{8} \mu \epsilon_0 \epsilon_r \frac{V^2}{d^3} \quad 2.2$$

where μ is the charge mobility, V is the applied voltage.

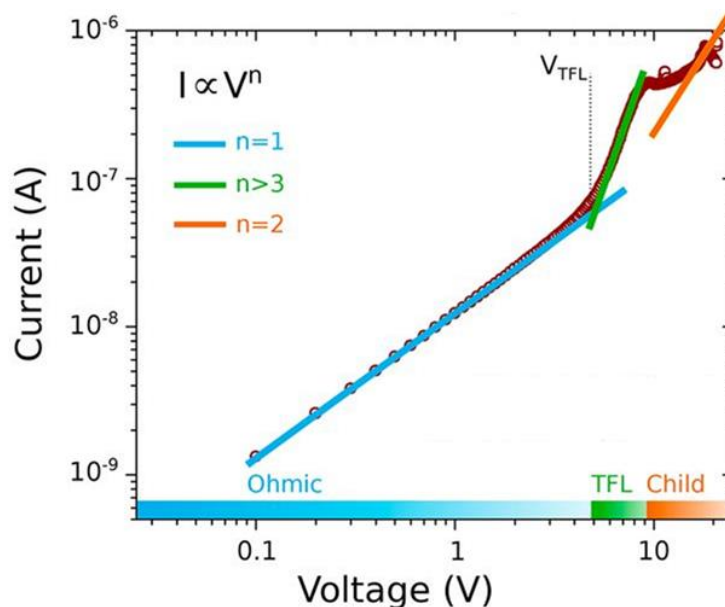


Figure 2.8: Schematic diagram of current-voltage curve for the space charge limited current (SCLC) method showing three regions: A linear ohmic regime ($I \propto V$, cyan line) is followed by the trap-filled regime, marked by a steep increase in current ($I \propto V^{n>3}$, green line) and a trap-free Child's regime ($I \propto V^2$, green line) at high voltages. Reproduced from Ref. [116] with permission from American Association for the Advancement of Science, Copyright 2015)

In this PhD research, space-charge-limited current method was used to determine the trap-state density in the photoactive films. Hole only devices based on $\text{MAPbI}_{3-x}\text{Cl}_x$ perovskite with and without AA additive were fabricated by using PEDOT:PSS (PH1000) as a bottom HTL (ITO side) and PEDOT:PSS (Clevios HTL Solar, SCA388-6) as a top HTL under Au top contacts. The photocurrent density-voltage (J-V) characteristics of the hole only devices were measured in forward bias in the range of 0 to 5 V with 50 mV steps, using a Keithley-2401 source meter.

2.4.6. Impedance Spectroscopy

2.4.6.1. Theory of Impedance Spectroscopy

Resistance (R) is a measure of a substance to resist the flow of electrical current. It is defined by Ohm's Law at all current, voltage and alternating frequency levels.

$$R = \frac{V}{I} \quad 2.3$$

Impedance (Z) is a measure of the ability to resist the flow of electrical current like resistance, but it is a more general term as it considers the phase shift between the voltage input and the current output, and is not in accordance with Ohm's law. Electrochemical impedance spectroscopy (EIS) is an important characterization technique which can be applied to investigate the electrical properties of materials, and dynamics process in the bulk or interfaces of any kind of solid or liquid material: ionic, semiconducting, mixed electronic-ionic, and even insulators (dielectrics). EIS measures the resistive and capacitive behavior of an electrochemical system by applying an alternating (AC) potential at different frequency and measuring the alternating current response through the cell. But it can also work by applying an alternating (AC) current to an electrochemical system and measuring the voltage through the system.^[118]

The applied AC potential signal as a function of time is given by;

$$E_t = E_o \sin(\omega t) \quad 2.4$$

Where E_t is the potential at time t, E_o is the amplitude of the potential and ω is the radial frequency, $\omega = 2\pi f$.

And the response signal measured (AC current) is given by;

$$I_t = I_o \sin(\omega t + \phi) \quad 2.5$$

Where I_t is the current response at time t, I_o is the current amplitude and ϕ is the phase shift between the AC potential and AC current signal.

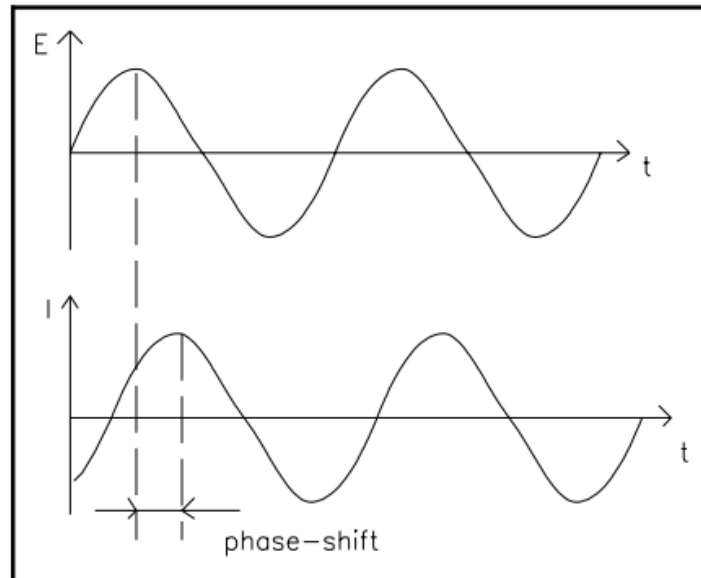


Figure 2.9: Schematic illustration of an impedance experiment: sinusoidal voltage input V at a single frequency/and sinusoidal current response in a linear system.^[118]

Combining the AC voltage and AC current, impedance is given by an expression analogous to Ohms law.^[119,120]

$$Z = \frac{E_t}{I_t} = \frac{E_o \sin(\omega t)}{I_o \sin(\omega t + \phi)} \quad 2.6$$

Where Z_o is the magnitude impedance, $Z_o = \frac{E_o}{I_o}$

$$Z = Z_o \frac{\sin(\omega t)}{\sin(\omega t + \phi)} \quad 2.7$$

The impedance is expressed by impedance magnitude and phase shift (ϕ).

Its known that according to Euler's relation:

$$\exp(j\phi) = \cos(\phi) + j\sin(\phi)$$

Based on this approach,

The potential can be expressed as: $E_t = E_o \exp(j\omega t)$

The current signal: $I_t = I_o \exp(j\omega t - \phi)$

And the impedance is given by:

$$Z = \frac{E_o \exp(j\omega t)}{I_o \exp(j\omega t - \phi)} = Z_o (\cos\phi + j\sin\phi) \quad 2.8$$

$$Z = Z_o \cos\phi + jZ_o \sin\phi = Z_{real} + jZ_{im} \quad 2.9$$

Where Z_{real} is a real part of impedance and Z_{im} is an imaginary part of impedance.

The phase angel (ϕ) at a given radial frequency (ω) given by:

$$\tan\phi = \frac{Z_{im}}{Z_{real}} ; \phi = \arctan\left(\frac{Z_{im}}{Z_{real}}\right) \quad 2.10$$

And the magnitude of impedance (modulus) is derived from the rectangular coordinates of the real and imaginary components of the impedance as shown in Figure 2.10.

$$|Z|^2 = Z_{real}^2 + Z_{im}^2 \quad 2.11$$

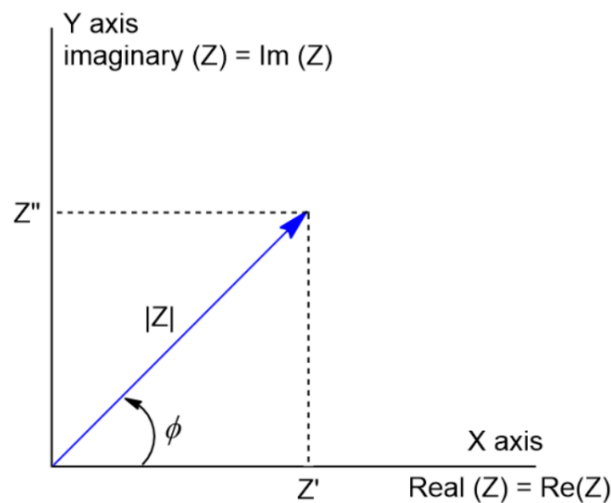


Figure 2.10: Rectangular and polar coordinates of real (Z') and imaginary (Z'') impedance together with the magnitude impedance $|Z|$ as the diagonal of the rectangle with phase angle (ϕ) from the $Re(Z)$. ^[119]

2.4.6.2. Intensity-Modulated Impedance Spectroscopy

Intensity-modulated impedance spectroscopy is another kind of impedance technique which uses modulated light as the perturbation signal to measure transfer function instead of using an AC voltage input signal to measure AC current signal. Intensity-modulated impedance spectroscopy includes techniques such as intensity-modulated photovoltage spectroscopy (IMVS) and intensity-modulated photocurrent spectroscopy (IMPS) which are located at different regions in the current-voltage (I-V) curve of solar cells as schematically shown in Figure 2.11. The EIS response under light can be applied at the I-V curve depending on the experimental set-up.^[121]

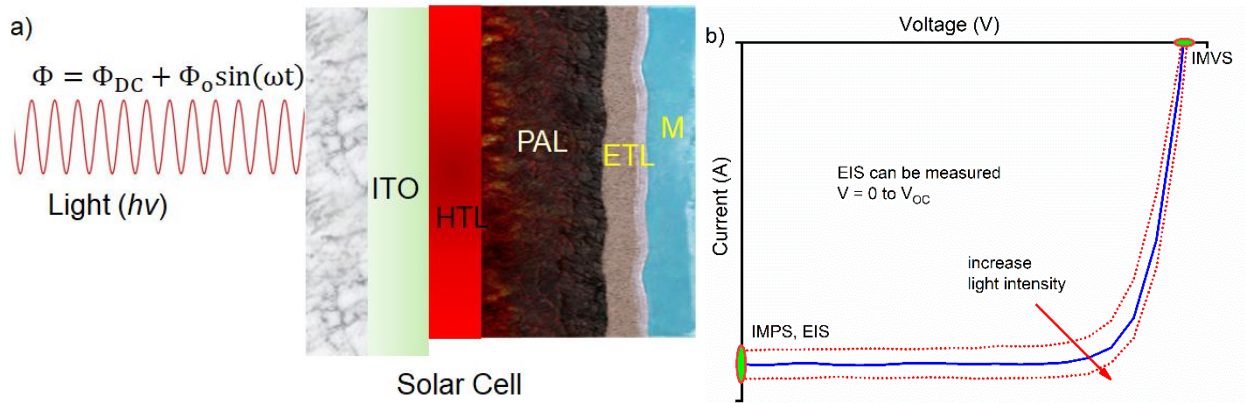


Figure 2.11: Schematics of the light signal focused on a PSC during intensity-modulated impedance measurement. (b) Photocurrent-voltage (I-V) curves of a solar cell with EIS, IMPS, and IMVS at the different points of the curve.

2.4.6.2.1. Intensity-Modulated Photovoltage Spectroscopy (IMVS)

Intensity-modulated photovoltage spectroscopy is an important intensity modulated impedance technique used to characterize recombination dynamics in mesoporous dye-sensitized, organic and perovskite solar cells in which the cell is held at open-circuit conditions under DC light illumination. The light intensity absorbed by the sample is fluctuated by a few percents (AC signal) to modulate the Fermi levels results in the production of a potential difference (photovoltage) measured as a function of modulation frequency. The experimental set-up is shown in Figure 2.12. The perturbation of light intensity controls modulated generation and recombination rates which causes modulation of the Fermi-levels.

The IMVS response involves the measurement of frequency-dependent transfer functions between the modulated input photon flux function ($\bar{\Phi}$) and measured modulated photovoltage output (\tilde{U}_{photo}).

$$H_{IMVS}(\omega) = \frac{\tilde{U}_{photo}}{\eta q \bar{\Phi}} = \frac{\tilde{U}_{photo}}{\bar{\Phi}} e^{i\varphi} \quad 2.12$$

Where η is the quantum efficiency for charge generation, q is the elementary charge and φ is the phase angle. The IMVS transfer function (H_{IMVS}) has units of Ωcm^2 which shows IMVS can be related to the impedance. But, as IMVS measurement is held at open-circuit voltage, there is no current flow through the external circuit during measurement and the control variable is the internal current, while for that of impedance measurements is usually the AC voltage.

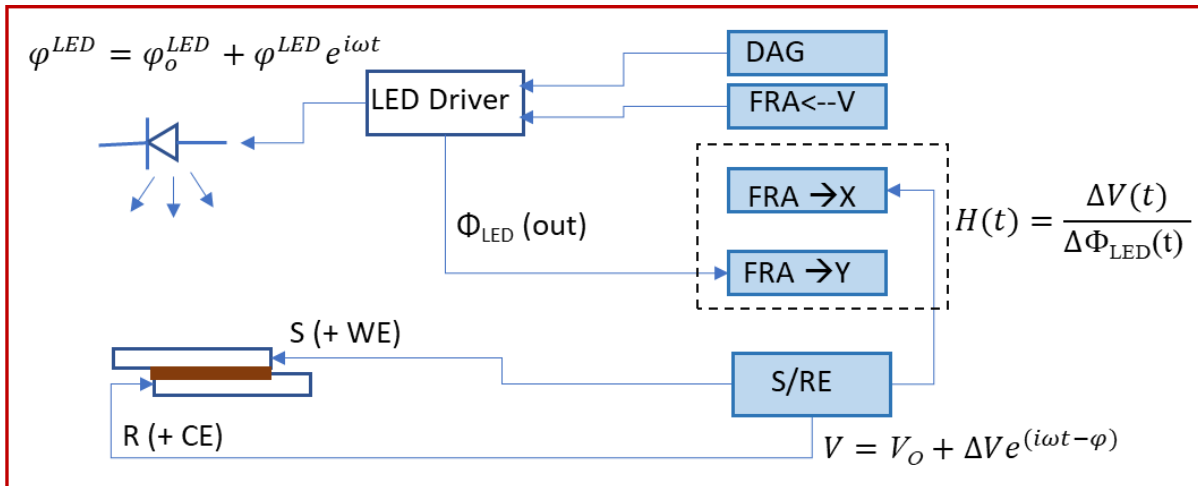


Figure 2.12: Schematic overview for the experimental setup for IMVS measurements.

2.4.6.3. Equivalent Circuit

To analyze and interpret the EIS data, a physical model consisting of electrical circuit elements is required. There can be more than one possible equivalent circuit, which gives a good fit with the experimental data. But fitting with the data does not necessarily mean that all of the seemingly suitable equivalent circuit models represent the electrochemical device structure. Rather, an intuitive understanding of the electrochemical device structure is an essential requirement to select a physically reasonable equivalent circuit for a given device. The equivalent circuit model is a combination of electrical circuit elements such as resistors, capacitors, and inductors.

Resistor (R) - is a real impedance which is independent of frequency with no phase shift ($\phi = 0$) between the input voltage and current response.

An inductor (L) - is an imaginary impedance component which stores energy in a magnetic field with AC current response phase-shifted by $+90^\circ$ with respect to the input AC voltage. The impedance of an inductor changes proportional to frequency.

$$L = \frac{Z}{j\omega} \quad 2.13$$

Capacitor (C) - is also an imaginary impedance component, and opposite to an inductor in which the capacitor's impedance decreases as the frequency is raised. The AC current through a capacitor is phase-shifted by -90° with respect to the input AC voltage.

$$C = \frac{1}{j\omega Z} \quad 2.14$$

Constant Phase Element (CPE)

For a system with ideal capacitive behavior the Nyquist plot is expected to be a perfect semicircle with the center on the x-axis. However, in real world, a Nyquist plot with depressed semicircles is

observed which is very difficult to fit with an ideal capacitor circuit element, and hence, such responses are represented by a constant phase element (CPE). Such response of an electrochemical device is associated with surface roughness, inhomogeneous reaction rates on a surface, different thickness or composition of a coating, which leads to varying in conductivity, and inhomogeneous current and potential distribution at the interface.^[122] The impedance of a CPE is given by:

$$Z_{CPE} = \frac{1}{T(j\omega)^P} \quad 2.15$$

where T is a constant with the unit F cm⁻², and P is related to the angle a purely capacitive response needs to be rotated in a complex plane plot. A CPE with 'P' value of 1 gives the same impedance as in the true capacitance. A CPE with P < 1, in parallel with a resistor gives a depressed semicircle on a Nyquist plot, and as P-value decreases the semicircle depression increases. When a CPE with p = 0 indicates an impedance of an ideal resistor. A CPE with P value of 0.5 implies a phase angle of 45 ° and represents a Warburg diffusion process which could be related to the diffusion of electrons or ions through a material.

2.4.6.3.1. Common Equivalent Circuit Models for Perovskite Solar Cells

2.4.6.3.1.1. Equivalent Circuits with Single Time Scale (Randles Circuit)

The impedance response of a perovskite solar cell with single time-constant in the Nyquist plot (as shown in Figure 2.13(a)) can be simulated using the Randles equivalent circuit (Figure 2.13(b)). It is the simplest model which consists of a double layer capacitance (C_{dl}) in parallel with a resistance (R_p) in combination with external series resistance (R_s). R_s accounts for the ohmic contribution of contacts and wires. The parallel resistance (R_p) is associated with the charge transfer resistance (R_{ct}) across the interfaces which is equal to the diameter of the semicircle in Nyquist plot. The capacitor (C_{dl}) is related to the accumulation of charges at the interfaces.^[118,119,123]

The impedance function of the system is given by;

$$Z(\omega) = R_s + \frac{R_{ct}}{1+i\omega C_{dl}R_{ct}} = R_s + \frac{R_{ct}}{1+i\omega\tau_1} \quad 2.16$$

Where τ_1 – is the time constant which is given by: $\tau = 1/2\pi f = R_{ct}C_{dl}$

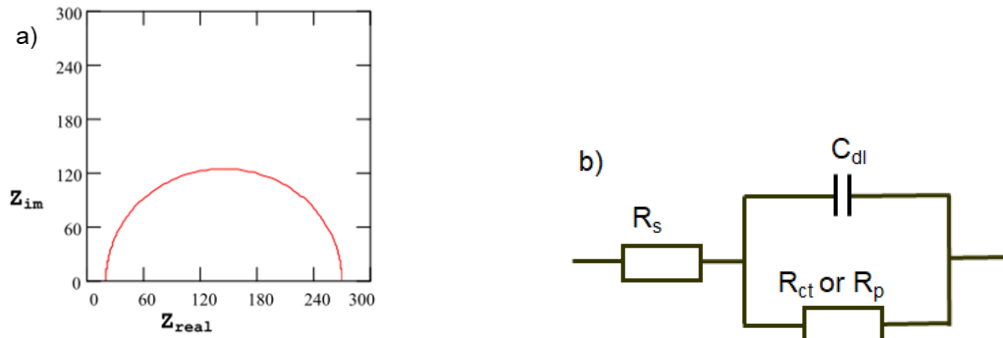


Figure 2.13 (a) Single time-component impedance response presented with Nyquist plot, and (b) the corresponding single time-constant equivalent circuit model (called Randles circuit).

2.4.6.3.1.2. Equivalent Circuits with Two or More Time Constant

For impedance responses of perovskite solar cells with two time constants, which is reflected in the Nyquist plot of the measurement data (Figure 2.14(a)), various possible equivalent circuits has been proposed. Matryoshka (ladder), Voight and Maxwell equivalent circuits are among the possible equivalent circuits which can give a good fit with the impedance response (see Figure 2.14(b, c and d)).^[124,125] G. Garcia-Belmonte et al. proposed to use the Matryoshka circuit model for planar perovskite solar cells.^[126] The circuit is a combination of the external series resistance (R_s) due to contacts resistance, wire resistance and sheet resistance of the electrode, two capacitive (C_1 and C_2) and two resistive (R_2 and R_3) elements, as drawn in Figure 2.14(b). The capacitive element, C_1 is a geometric capacitance associated with the dielectric response of the perovskite layer which dominates the capacitive response in the high-frequency region (>1 kHz) of the spectra. The second capacitive element, C_2 is a low-frequency response (≤ 1 Hz) related to the surface charge accumulation at the interfaces of the solar cell. The resistance, R_2 is coupled with C_1 and associated with the charge transport resistance of the bulk perovskite. It is also influenced by the contact transport resistance at the interfaces. The low-frequency resistance, R_3 is associated with recombination resistance at the interfaces, and slow processes like ion diffusion.^[124,126,]

The impedance functions for the two-component with Matryoshka circuit is given by:

$$Z_T = R_s + \frac{R_2 + R_3 + i\omega_2 C_2 R_2 R_3}{i\omega_1 C_1 (R_2 + R_3 + i\omega_2 C_2 R_2 R_3) + i\omega_2 C_2 R_3 + 1} = R_s + \frac{R_2 + R_3 + iR_2}{i\omega_1 C_1 R_3 + 2i} \quad 2.17$$

Where the time constant $\tau_j = 1/\omega_j = R_{j+1}C_j$, ω_1 -is high-frequency and ω_2 -low-frequency.

However, most experimental data exhibit depressed semicircles in the Nyquist plot, implying the capacitive behavior deviates from ideal. Fitting depressed semicircles using Matryoshka circuit with ideal capacitor is quite tricky. But, replacing the geometric and surface capacitors with non-ideal circuit element, called constant phase element (CPE) (see Figure 2.14(e)) gives a good fitting. In this thesis, Matryoshka circuit was used to fit the impedance measurement results.

Sometimes the impedance measurement data of PSCs exhibit three distinguishable time constants at high, medium and low-frequency region. To fit such measurement data, a hybrid Matryoshka-Voight circuit (Figure 2.14(f)) is usually used. Alternatively Matryoshka, Voight and Maxwell type circuits can also be used.^[124,127]

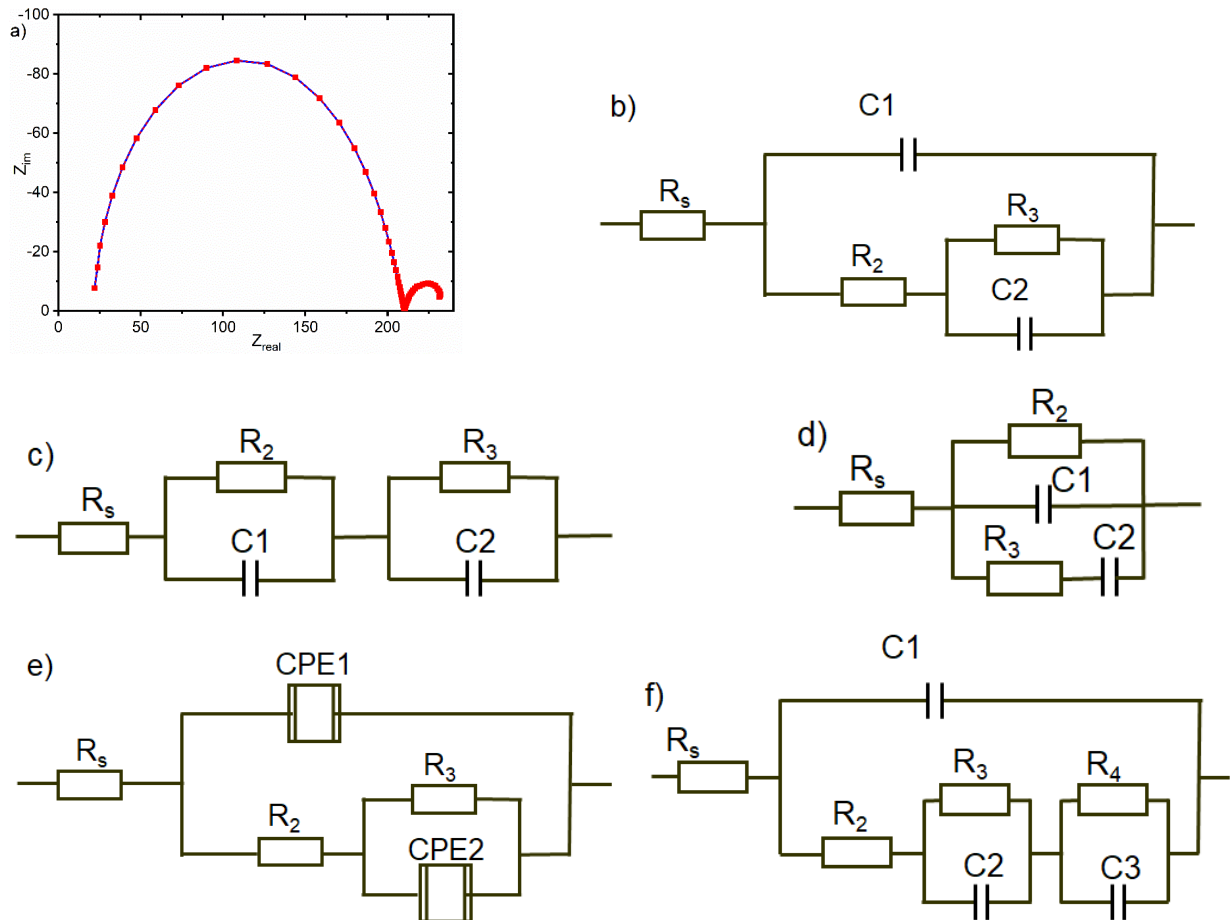


Figure 2.14: (a) Nyquist plot of characteristic two time-constant impedance response of perovskite solar cells. Possible equivalent circuit models for impedance response with two distinguishable time constants; (b) Matryoshka, (c) Voight, and (d) Maxwell circuits. (e) Matryoshka circuit with constant phase element (CPE) replacing the ideal capacitors. (f) Equivalent circuit model for impedance response with three time-constants.

2.4.6.4. Intensity Modulated Impedance Spectroscopy Setup

In this study an intensity modulated EIS technique was used to study the electronic and ionic dynamics across the interfaces and bulk of perovskite solar cells. The characterization was applied under light perturbation in the frequency range of 1 MHz to 0.02 Hz using a EchemLab XM-Potentiostat/Galvanostat (Solartron Analytical) set-up equipped with ModuLab®XM PhotoEchem software (Figure 2.15). The software includes comprehensive packages such as;

- Intensity Modulated Photocurrent Spectroscopy (IMPS)
- Intensity Modulated Photovoltage Spectroscopy (IMVS)
- Electrochemical Impedance Spectroscopy (in the dark and under light)
- I-V(in the dark and under light)
- Charge Extraction Methods, e.g. short-circuit and dark charge extraction

- Photo Voltage Decay

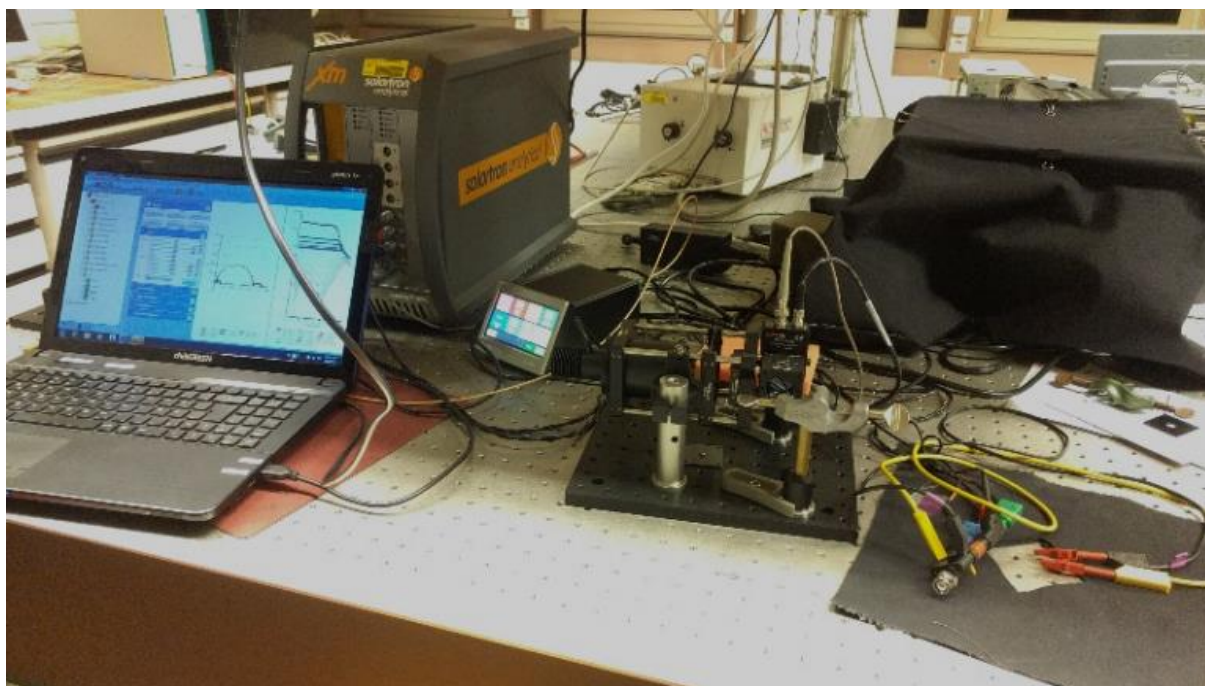


Figure 2.15: Image of EchemLab XM-Potentiostat/Galvanostat (Solartron Analytical, AMETEK) with 590 nm LED which is adjusted using the attached Thorlabs DC2100 driver.

2.4.6.4.1. IMVS Measurement

Intensity-modulated photovoltage spectroscopy measurements were carried out at open-circuit (V_{OC}) conditions under illumination with 10 % modulation amplitude. The sample devices were focused in front of the LED. In the PhotoEchem software the parameters were set to measure at V_{OC} (DC-voltage) condition with 10 % light intensity perturbation in the frequency range from 1 MHz to 20 mHz. The values of LED light intensity were fed to the program to vary the intensity by controlling the current applied to the LED source. The software generates an intensity calibration curve using its NIST calibrated reference photodiode and controls the LED intensity directly via the LED driver (Thorlabs DC2100). Before the IMVS measurement was started, the J-V characteristics of the device was measured to check the device status and the proper connection.

2.4.6.4.2. Electrochemical impedance spectroscopy (EIS) Measurement

Following the IMVS measurements, electrochemical impedance spectroscopy measurements were carried out at short-circuit conditions under illumination using the same experimental setup. To measure the EIS, in the PhotoEchem software the applied potential was set to measure at short-circuit (0 V DC-voltage) and 10 mV AC voltage in the frequency range from 1 MHz to 20 mHz. Similar to IMVS measurement, the values of LED light intensity were fed to the program to vary the intensity by controlling the current applied to the LED source. After the EIS and IMVS

measurements were finished, the J-V response was measured to check the status of the device (whether the device remained stable or show significant change).

2.4.7. Capacitance-Voltage Measurement

A Novocontrol impedance spectrometer (see Figure 2.16) was used to measure the capacitance-applied voltage (C-V) response of perovskite solar cells to evaluate the trap density and depletion energy. The solar cells were connected to the impedance via the 4-wire impedance test interface system in which the bottom contact was connected to the high current interface and the top (cathodic) contact was connected to the low current port. The instrument is equipped with WinDETA software to control the instrument and data analysis. Within the WinDETA software, the sample specifications regarding the active area and thickness were set to 0.15 cm² and 70 nm, respectively, to eliminate the effect of spray capacitance. Frequency of 10 kHz, and AC Voltage of 10 mV were filled in the initial and final conditions. Then, the applied DC voltage was set in the range of -0.5 to 1.5 V (forward bias) with 25 mV steps. The C-V response of the devices were measured under dark conditions, and from which the C-V and Mott-Schottky analysis was done.

In the Mott-Schottky plot, C and V are related by:^[164-129]

$$\frac{1}{C^2} = \frac{-2(V-V_{bi})}{\epsilon_r \epsilon_0 q A^2 N_t} \quad 2.18$$

Where N_t is the doping density (in this case the defect density in the perovskite film), q is the elementary charge, ϵ_r is the dielectric constant of the perovskite, A area of measured cells (0.15 cm² for both the sample and control cells), V_{bi} is the built-in voltage and ϵ_0 is vacuum permittivity.

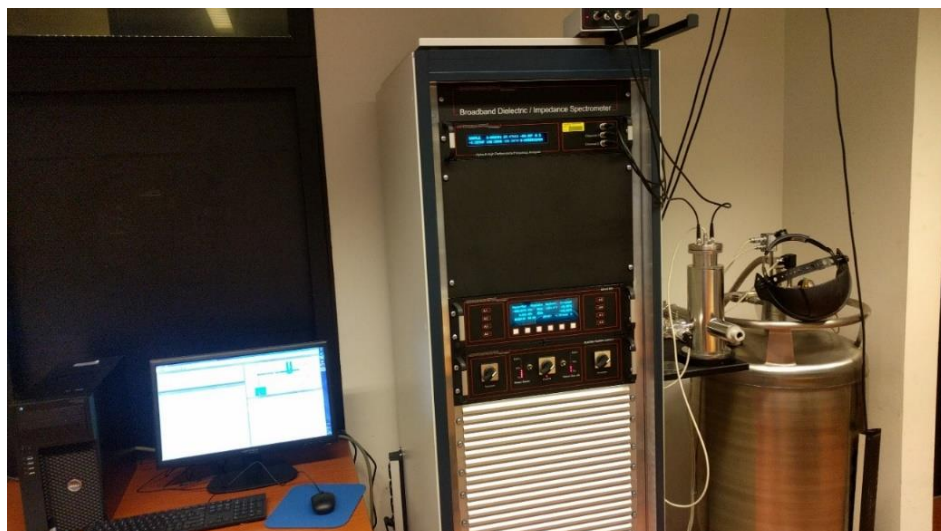


Figure 2.16: Image of Novocontrol Broadband Dielectric/Impedance spectrometer set-up.

3. Results and Discussion

3.1. Low Temperature Processed TiO_x Interfacial Layer for Inverted p-i-n Perovskite Solar Cells

The results described in this section are published in: *RSC Advances*, 2018.

DOI: 10.1039/c8ra03993c

Authors: Bekele Hailegnaw, Getachew Adam, Herwig Heilbrunner, Dogukan H. Apaydin, Christoph Ulbricht, Niyazi Serdar Sariciftci and Markus C. Scharber

In this chapter, the role of a low temperature processed titanium oxide (TiO_x) interlayer between [6,6]-phenyl- C_{60} butyric acid methyl ester (PCBM) and back contact electrode (Al) was investigated for mixed-cation mixed-halide perovskite ($\text{CsFAMAPbI}_{3-x}\text{Br}_x$) devices. Devices were fabricated on PEDOT:PSS (Clevios FHc) and/or NiO_x HTLs as mentioned in the devices fabrication section and PCBM was used as an ETL on top of the photoactive perovskite layer. The control devices with an ITO/ NiO_x / $\text{Cs}_{0.05}(\text{FA}_{0.83}\text{MA}_{0.17})_{0.95}\text{PbI}_{3-x}\text{Br}_x$ /PCBM/Al structure, were completed via thermal evaporation of back metal contact (Al) on top of the ETL layer. Figure 3.1(a) shows the schematic diagram, and Figure 3.1(b) shows the cross-section SEM image of a device that was fabricated by the deposition of a TiO_x interlayer on top of the electron transport layer (PCBM), followed by thermal evaporation of the back metal contact. Figure 3.1 (c) shows the schematic energy band diagram of the different layers in the device.

The structure and lattice parameters of mixed-cation mixed-halide perovskite ($(\text{Cs}_{0.05}(\text{FA}_{0.83}\text{MA}_{0.17})_{0.95}\text{PbI}_{3-x}\text{Br}_x)$) films were characterized by X-ray powder diffractometer. Figure 3.1(d) shows the XRD spectra of a mixed-cation mixed-halide perovskite film deposited on a glass substrate. Films were deposited on oxygen plasma treated glass substrates using similar spin-coating parameters used for solar cells fabrication and annealed at 100 °C for 60 min inside the glove-box. The diffraction peaks at 14.7, 20.6, 25.2, 29.0 and 32.4° correspond to the characteristics diffraction peaks of tetragonal perovskite with (110), (112), (202), (220) and (310) lattice planes symmetry, respectively. The calculated lattice constants are about 8.6 Å and 12.6 Å for a and c, respectively.^[35,130]

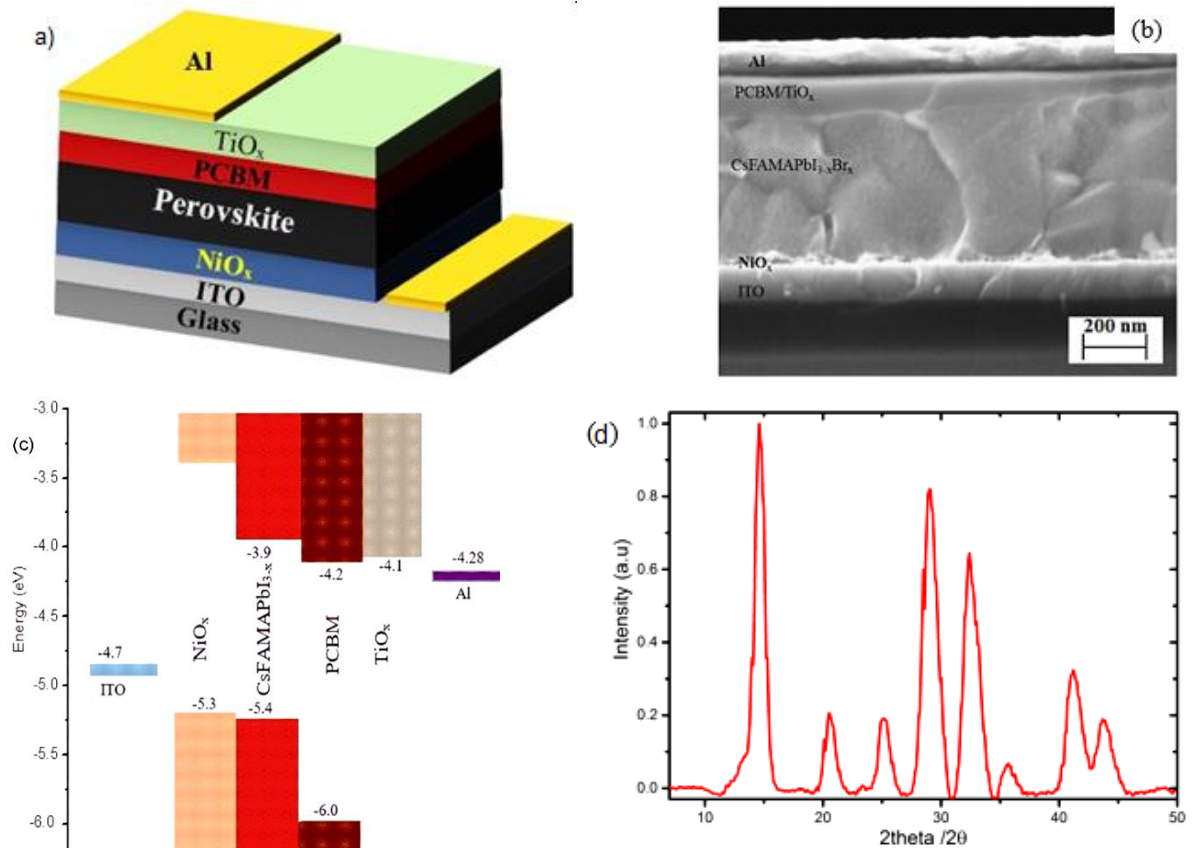


Figure 3.1. (a) Schematic overall structure, (b) cross-section SEM image of planar mixed-halide mixed-cation PSCs with TiO_x interlayer between PCBM and Al electrode, and (c) schematic energy band representation of the device. (d) Characteristics X-ray diffraction spectrum of mixed-halide mixed-cation perovskite film deposited on glass substrate.

3.1.1. Current Density-Voltage Response

Figure 3.2 shows the photocurrent density-voltage characteristics of the sample and control PSCs with NiO_x and PEDOT:PSS HTLs under 100 mW/cm^2 illumination (AM1.5 global spectrum). The recorded photovoltaic parameters are summarized in Table 3.1. The J-V response of the control devices (devices without TiO_x interlayer) displays less rectification as shown in Figure 3.2(a&b) and Table 3.1, resulting in low fill factors (FF) and power conversion efficiencies. Devices with TiO_x interlayer (PCBM/ TiO_x /Al interlayer) show higher FF and improved PCE. In addition, solar cells with a TiO_x interlayer show substantially lower hysteresis (Figure 3.2(a) and Table 3.1). Similarly, devices with TiO_x interlayer show lower characteristic resistance ($R_s \sim 16 \Omega$) compared to devices without TiO_x interlayer (ca. 380Ω) as shown in Table 3.1. The resistance value (R_s) is calculated from the slope of J-V curve by taking the last five points in the forward scan and the first five points in the reverse scan. The resistance value (R_p) of the devices is calculated from the slope of the J-V curve by taking the first five points in the forward scan and the last five points in the reverse scan. Calculated R_s and R_p values are presented in Table 3.1.

Figure 3.2(b) shows the J-V curves of devices with PEDOT:PSS as a HTL. Similar trends were observed for devices with PEDOT:PSS. Interestingly devices with PCBM/ TiO_x /Al interface show

improved FF of about 77.6 % (reverse), PCE of ~12.5 % (reverse) and reduced R_s (10Ω) compared to PCBM/Al interface-based devices, which exhibit a FF of about 61.2 % (reverse), PCE of ~9.7 % (reverse) and about 12-times higher R_s value of more than 130Ω (Table 3.1). This suggests that the TiO_x interlayer reduces the charge extraction barrier between PCBM and Al electrode. The observed high series resistance and S-shaped J-V curve for control devices might be correlated with corrosion of the Al electrode via halide ions diffused from the perovskite. As halide ions have a small migration activation energy, these ions could diffuse through PCBM and react with Al. This reaction causes the formation of a thin insulating layer at the interface.^[131] External quantum efficiency (EQE) and integrated current density calculations for both kind of devices (devices with and without TiO_x interlayer) show similar responses (see in Figure 3.2(c&d)). As can be seen, devices with PEDOT:PSS as a HTL show lower V_{OC} and J_{SC} compared to devices based on NiO_x HTL. As a result, further optimization was focused on devices with NiO_x HTL.

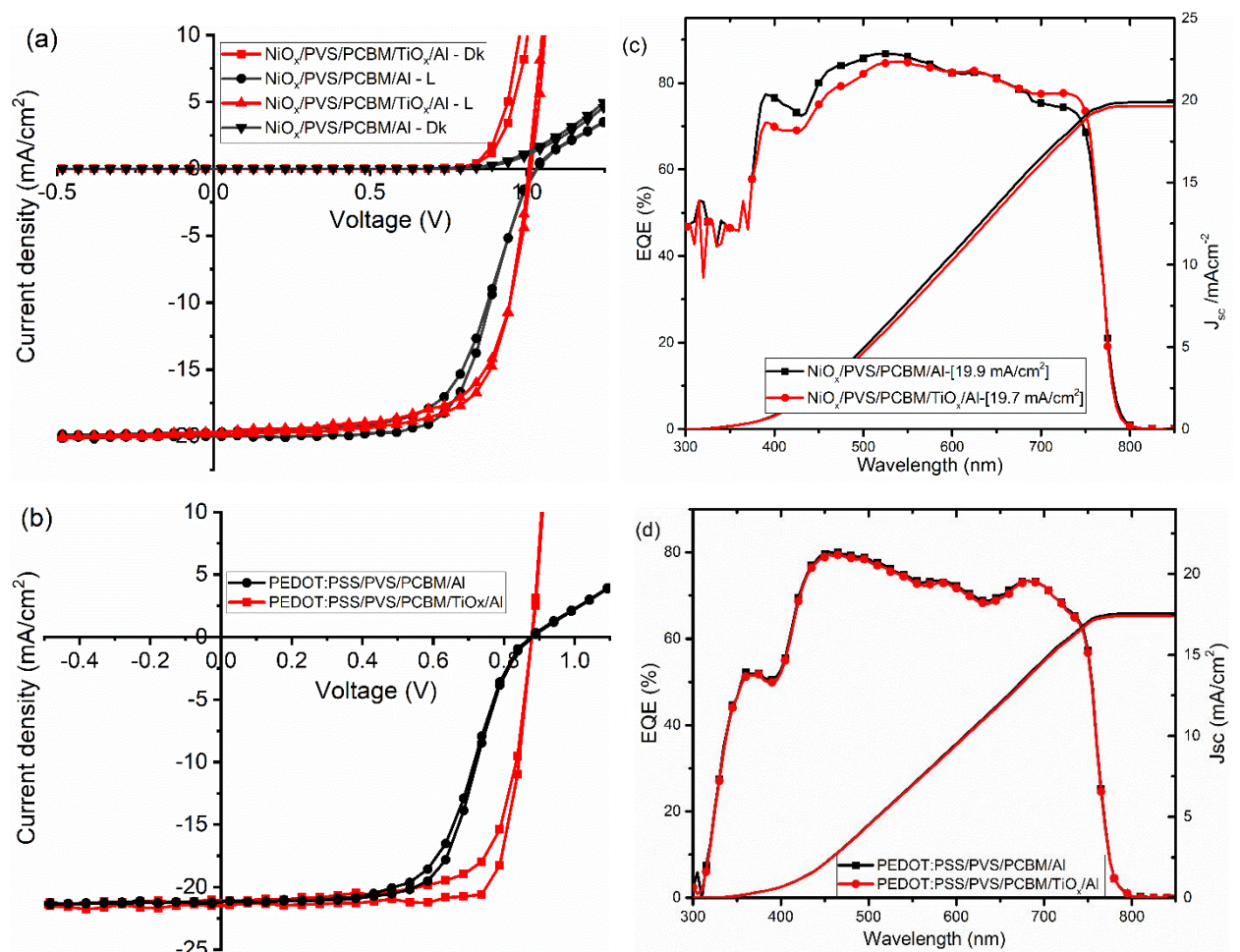


Figure 3.2. J-V characteristics of inverted mixed-cation mixed-halide PSCs on (a) NiO_x HTL, and (b) PEDOT:PSS HTL with TiO_x interlayer (PCBM/ TiO_x /Al interface) and control device (PCBM/Al structure) in dark (Dk) and under AM1.5 solar spectrum with 100 mW/cm^2 light intensity illumination (L). External quantum efficiency (EQE) of inverted PSCs with, (c) NiO_x HTL, and (d) PEDOT:PSS HTL with and without TiO_x interlayer on top of PCBM and the corresponding integrated current density from the EQE data.

	V_{oc} (V)	J_{sc} (mA/cm ²)	FF (%)	PCE (%)	R_p (Ω)	R_s (Ω)
Devices with NiO_x as HTL						
PCBM/Al - Rvs	1.03	20	65.6	13.5	14493	385
PCBM/Al - Fwd	1.03	19.7	61.9	12.6	8509	373
PCBM/TiO _x /Al - Fwd	1.04	20.1	66.2	13.9	5458	15
PCBM/TiO _x /Al - Rvs	1.03	20.3	69.4	14.6	1788	16
Devices with PEDOT:PSS as HTL						
PCBM/TiO _x /Al - Rvs	0.9	17.8	77.6	12.5	43437	10
PCBM/TiO _x /Al - Fwd	0.9	17.4	71	11	43061	8
PCBM/Al - Fwd	0.9	18	58.7	9.2	1419	133
PCBM/Al - Rvs	0.9	18.1	61.2	9.7	9145	169

Table 3.1. Summarized J-V characteristics (open-circuit voltage (V_{oc}), short-circuit current (J_{sc}), fill factor (FF), power conversion efficiency (PCE), parallel resistance (R_p) and serial resistance (R_s)) of PSCs with TiO_x interlayer (PCBM/TiO_x/Al) and control (PCBM/Al) on NiO_x and PEDOT:PSS (Clevios F HC) HTLs for forward (Fwd) and reverse scans (Rvs).

3.1.2. Topographic and Optoelectronic Results

Atomic force microscopy (AFM) and scanning electron microscopy (SEM) techniques were used to characterize the surface modifications induced by a TiO_x interlayer (PVS/PCBM/TiO_x interface). The perovskite films were deposited on NiO_x having identical stack in the solar cell. Figure 3.3(a&b) show the AFM and SEM images of mixed-cation mixed-halide perovskite film, respectively. A well packed, dense and pinhole-free film with grains size in the range of 50-500 nm is found. The root-mean-square (RMS) roughness of the studied film is about 21.9 nm. The surface morphological feature in the SEM topographic image is consistent with the AFM image. Figure 3.3(c&d) show the AFM and SEM images of perovskite films covered with about 80 nm of PCBM layer. The deposition of PCBM layer improves the smoothness of the surface and the average RMS roughness is reduced to about 6.93 nm. This suggests that PCBM covers the perovskite film effectively. This is crucial to avoid direct contact of the perovskite with the top electrode and surrounding ambient air solvent as it is more sensitive to polar solvents. Sample films with an approximately 15 nm TiO_x layer on top of PCBM deposited via spin-coating of TiO_x sol-gel at high speed show a smooth film with sparsely distributed nano-dot features on the surface as shown on Figure 3.3(e&f). The RMS roughness of the film covered with TiO_x thin-layer further decreased to 4.6 nm. This indicates that the TiO_x interface improves the surface smoothness and heals surface defects of PCBM film, and further reduces the probability of direct contact between the photoactive layer and the Al back electrode. Moreover, morphological improvement might modify the interfacial contact area which will have a significant effect on the charge extraction process across the interface.

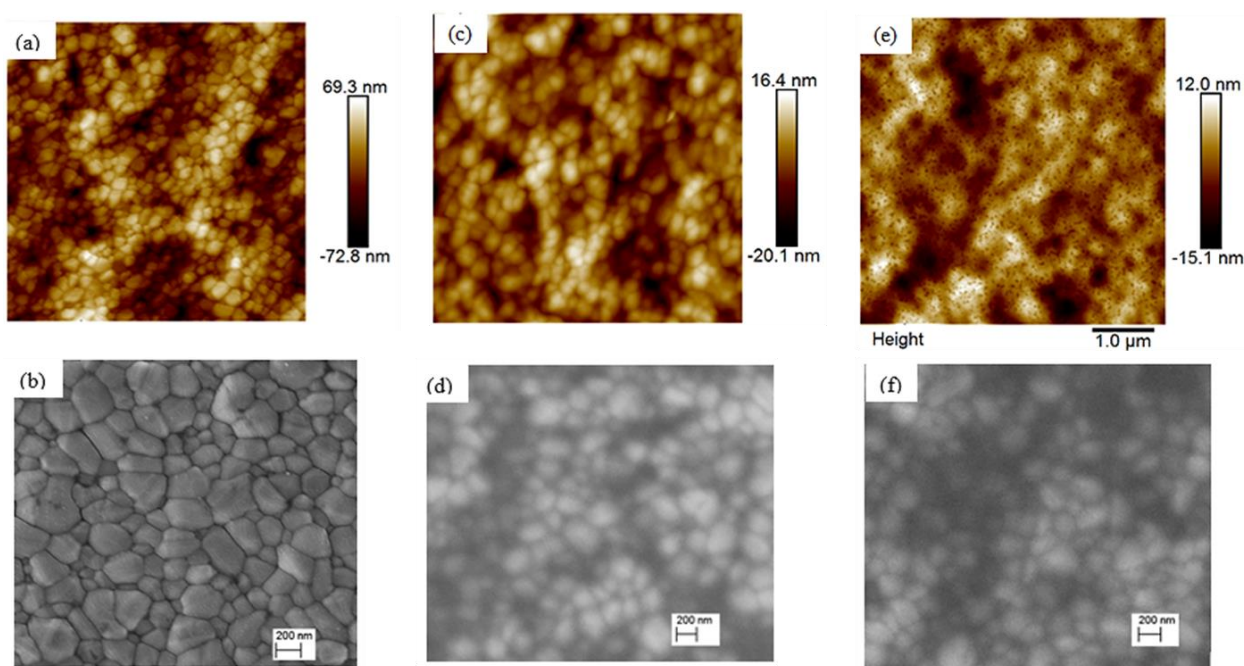


Figure 3.3. Atomic force microscopy (AFM, *left*) and scanning electron microscopy (SEM, *right*) images of mixed-cation mixed-halide perovskite films, (a) and (b), mixed-cation mixed-halide perovskite with PCBM on top, (c) and (d), and mixed-cation mixed-halide perovskite/PCBM with TiO_x on top, (e) and (f). The films are deposited on ITO substrate covered with NiO_x particles.

Furthermore, photoluminescence (PL) spectra of a perovskite film, perovskite films covered with PCBM (PVS/PCBM) and PCBM followed by TiO_x (PVS/PCBM/ TiO_x) on glass substrate were recorded (Figure 3.4(a)). Films with a TiO_x interlayer show stronger quenching compared to devices without TiO_x interlayer. Similarly, the photoluminescence decay spectra, shown in Figure 3.4(b), also displays faster PL decaying for the film with a TiO_x interlayer compared to the film without TiO_x interlayer. This indicates the charge carrier life-time decreases when a TiO_x layer is added on top of PCBM. This could be due to fast charge carrier transfer to the ETL and decreases the radiative recombination process occurring at a slow time scale (>50 ns). Also, as shown in the AFM images (Figure 3.3) a TiO_x layer could reduce the defect states at the perovskite/PCBM interface, which reduces the slow-time radiative process due to trapped charge carriers.

Furthermore, Figure 3.4(c) shows the electroluminescence (EL) of an encapsulated sample and control solar cells recorded at different applied voltages near the open-circuit. A voltage bias was applied via Keithley-2400 source meter, and the emitted photons were focused and passed through an optical fiber to a Shamrock SR-303i monochromator and detected by an AndorTM iDus Si-CCD detector. Solar cells with a TiO_x interlayer show stronger EL at a given applied voltage compared to the control devices. Analogously, the current density generated by the devices as a function of bias voltage plotted in Figure 3.4(d) indicates that the TiO_x interlayer boosts the charge carrier extraction process at the back electrode interface. This could be related to a reduction of

charge trapping and recombination channels at the ETL and back electrode interface and reduction of the charge extraction barrier between the ETL and Al electrode.

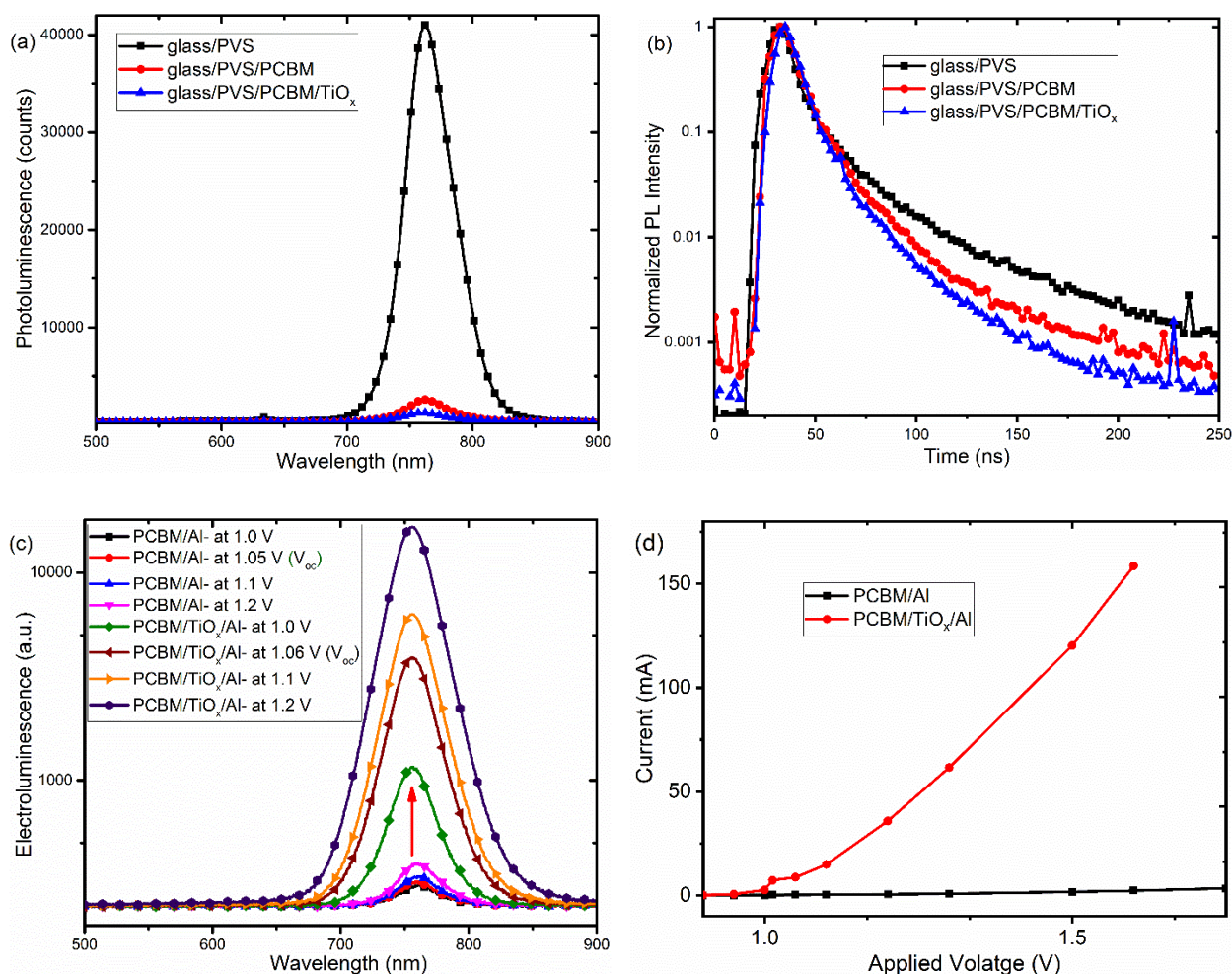


Figure 3.4. (a) Photoluminescence (PL) spectra, and (b) photoluminescence decay spectra of mixed-cation mixed-halide perovskite films (PVS), PVS covered with PCBM (PVS/PCBM) and with additional TiO_x top layer (PVS/PCBM/TiO_x). (c) Electroluminescence (EL) spectra as a function of voltage bias of p-i-n based mixed-cation mixed-halide perovskite SCs with TiO_x interlayer (PCBM/TiO_x/Al interfacing) and control device (PCBM/Al interfacing) under laser excitation (405 nm). The emitted radiation was collected through 250 μm slit with 1 s integration. (d) the J-V curve of the PSCs response at different bias under dark condition.

3.1.3. Impedance Spectroscopy (IS)

To examine the impact of the TiO_x buffer layer on the charge carrier dynamics across the bulk and interfaces of PSCs, electrochemical impedance spectroscopy (EIS) and intensity-modulated photovoltage (IMVS) characterization were applied. The EIS characteristics of an optimized PSCs with TiO_x interlayer and control devices were measured under short-circuit conditions with 10 mV AC-voltage in the frequency range between 1 MHz and 0.02 Hz under LED light ($\lambda = 590$ nm) illumination. The IMVS response of the same PSC used in the EIS experiments was measured at an open-circuit voltage in the frequency range between 1 MHz to 0.02 Hz under 8 mW/cm² LED irradiation ($\lambda = 590$ nm) with light intensity perturbation (10 % modulation amplitude).

Figure 3.5(a&b) show the Nyquist plots and the corresponding Bode plots of the EIS response, respectively. The EIS responses of devices with and without TiO_x buffer layer display two characteristic semi-circles in the Nyquist plot. The high-frequency (1 MHz-10 kHz) response is associated with charge carrier transport resistance (R_2), and the low-frequency (10 Hz-20 mHz) features are attributed to the impedance of ionic diffusion and trap-states (charge recombination) within the perovskite film and at the perovskite charge transport layer interfaces.^[30,112,132] Figure 3.5(c) shows the equivalent circuit model of the PSCs which was used to interpret the EIS responses. The fitting parameters derived using the suggested equivalent circuit for the EIS response of the sample and control devices are summarized in Table 3.2. The EIS responses show that devices with a TiO_x interlayer (PCBM/ TiO_x /Al) exhibit lower charge transport resistance (R_2) compared to the control device (PCBM/Al structure). This indicates TiO_x interlayer improves the charge transport process in the device which is in good agreement with the reduced serial resistance observed in the J-V response.

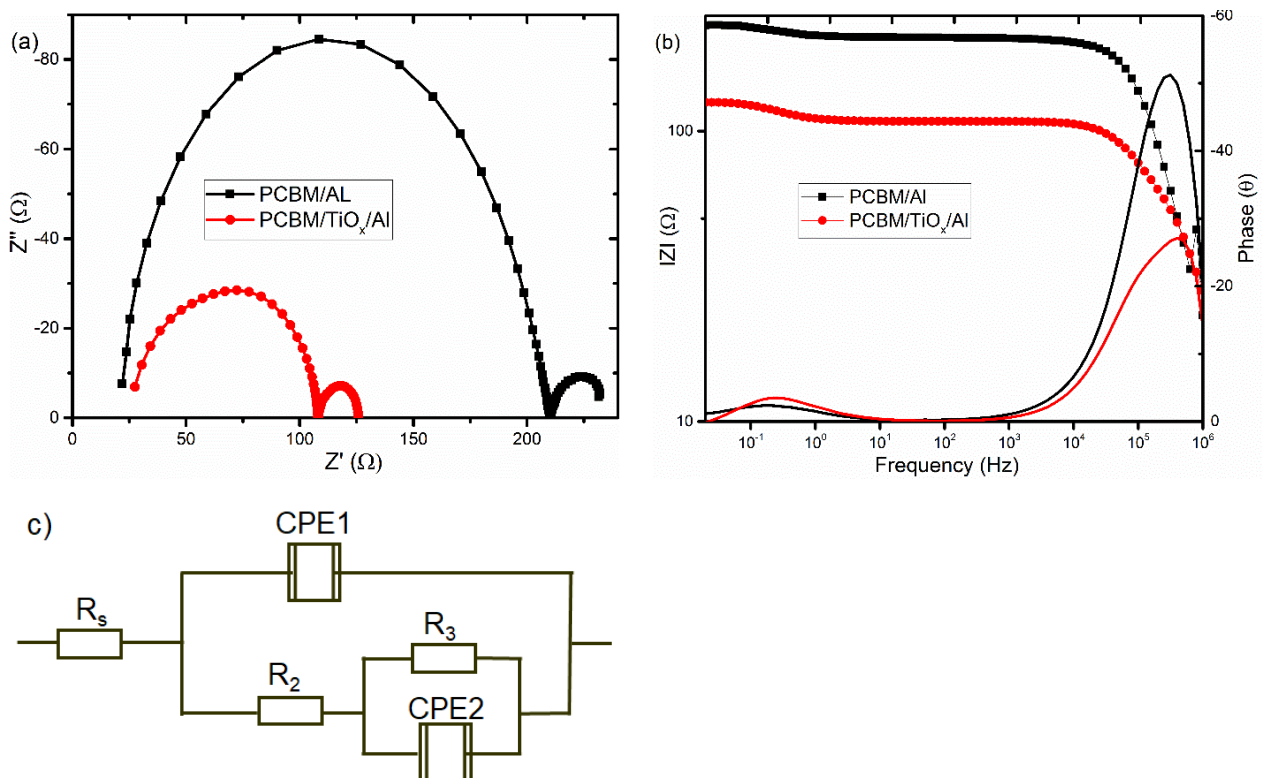


Figure 3.5. (a) Nyquist and (b) Bode plots of the characteristic electrochemical impedance spectroscopy (EIS) responses of PSC with TiO_x interlayer (PCBM/ TiO_x /Al) and control device (PCBM/Al) scanned in the frequency range of 1 MHz to 20 mHz and 10 % light modulation under 8 mW/cm^2 LED light intensity. (c) The equivalent circuit model for the PSCs.

Device structure	R _s (Ω)	R ₂ (Ω)	CPE1		R ₃ (Ω)	CPE2	
			T1	P1			
PCBM/AL	20	189	2.5×10 ⁷	0.925	23	20	189
PCBM/TiO _x /Al	22	38.5	2.0×10 ⁷	0.9	16	22	38.5

Table 3.2. Fitting parameters of the equivalent circuits for the characteristic EIS response of PSCs with TiO_x interlayer (PCBM/TiO_x/Al) and control devices (PCBM/Al).

Figure 3.6(a&b) show the intensity-modulated photovoltage spectroscopy responses of the sample and control devices displayed as Nyquist and Bode plots, respectively. The Nyquist plot (Figure 3.6(a)) shows two characteristic semicircles. The high-frequency semicircle is related to the charge recombination resistance (R_{rec}) in the device.^[133] The device with TiO_x interlayer (PCBM/TiO_x/Al) shows higher R_{rec} compared to the control device, which confirms that interfacing the ETL and back electrode (Al) with TiO_x improves the charge carrier extraction and overall performance. This is in a good correlation with the observed lower serial resistance value for devices with TiO_x interlayer in the J-V response (see in Table 3.1).

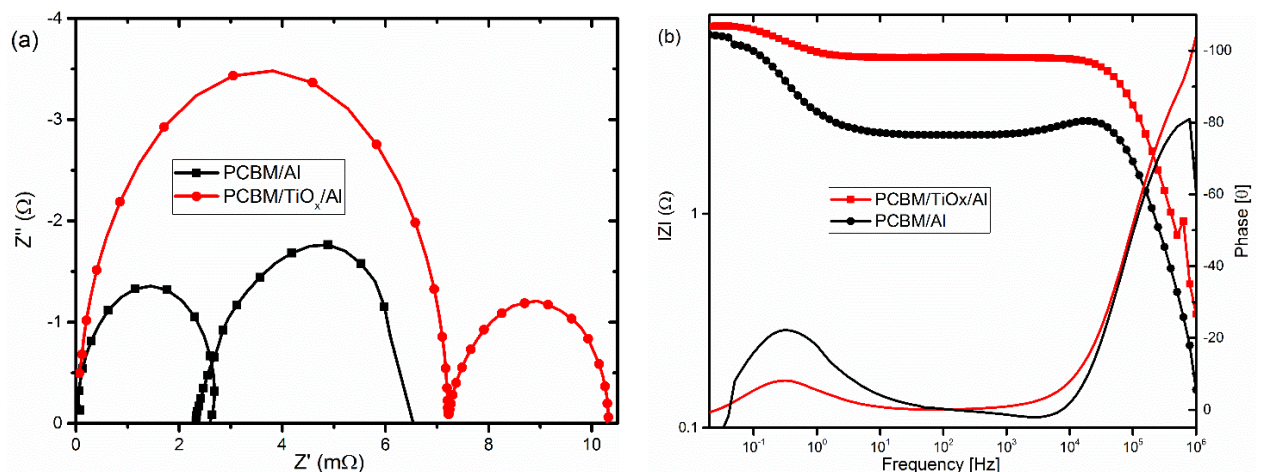


Figure 3.6. Intensity modulated photovoltage spectroscopy (IMVS) responses with (a) Nyquist plot, and (b) Bode plot of PSCs with TiO_x interlayer (PCBM/TiO_x/Al) and control device scanned in the frequency range of 1 MHz to 20 mHz with 8 mW/cm² LED light.

3.1.4. Device Optimization

To improve the device performance, optimizations of the different layers in the solar cells were conducted. Devices with different thickness of NiO_x as HTL were fabricated. Figure 3.7(a) shows the J-V response of devices with different thickness of NiO_x deposited with different spin-coating recipes (3000 rpm for 30 s; at 3000 rpm for 15 s and 4000 rpm for 15 s; at 4000 rpm for 30 s; and at 4000 rpm for 15 s and 5000 rpm for 15 s) followed by heat treatment at 140 °C for 20 min. Devices with the thinnest layer of NiO_x shows the highest J_{sc}, V_{oc} and overall performance.

To optimize the thickness of TiO_x interlayer, devices with TiO_x interlayer of different thickness were deposited by spin-coating (at 2000 rpm, 4000 rpm and 5000 rpm for 30 s) which resulted in about 35 to 40, 15 to 20 and 10 to 15 nm thick TiO_x layers, respectively. Figure 3.7(b) shows the J-V curves of devices with different thickness of TiO_x interlayer and devices with about 10 nm thick TiO_x interlayer shows the best photovoltaic parameters.

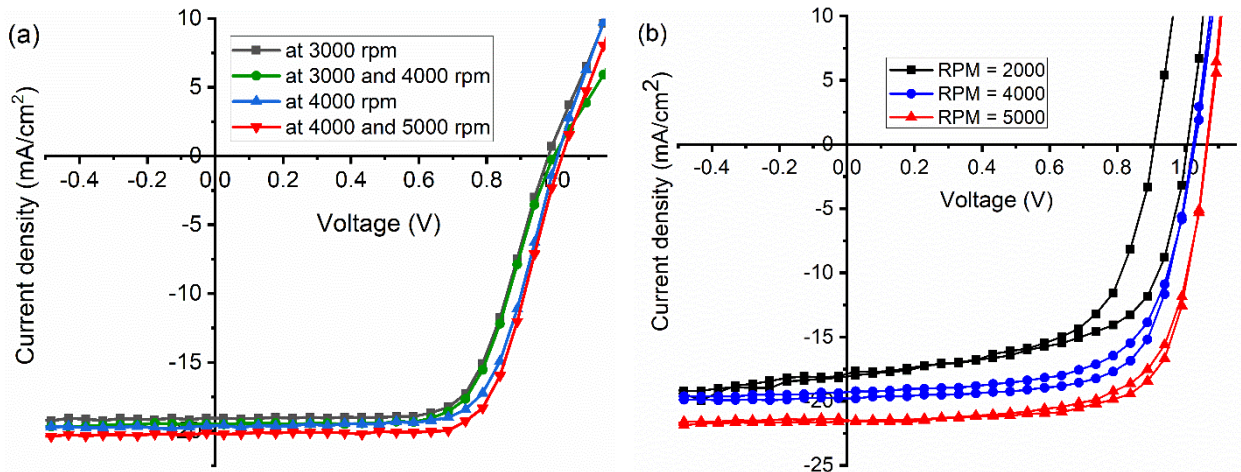


Figure 3.7. (a) J-V characteristics of PSCs with different thickness of NiO_x spin-coated at 3000 rpm for 30 s; at 3000 rpm for 15 s and 4000 rpm for 15 s; at 4000 rpm for 30 s; and at 4000 rpm for 15 s and 5000 rpm for 15 s. (b) J-V curves of PSCs with different thickness of TiO_x interlayer processed at various spin-coating speeds (i.e. 2000, 4000 and 5000 rpm).

After successive optimization of the processing conditions and thickness of different layers, an improved PSC with TiO_x interlayer with a V_{oc} of about 1.07 V, J_{sc} of 21.1 mA/cm², FF of 72.5 % and average PCE of 16.1 ± 0.2 % could be obtained (Figure 3.8(a&b)). The characteristic photovoltaic parameters of the best performing device are summarized in Table 3.3. Figure 3.8(c) show the EQE of the best device which is improved to about 85 % resulting in an integrated current density of 20.94 mA/cm². To show the reproducibility of the fabrication process and performance of our devices, the statistical histogram for PCE of 109 different solar cells was collected (Figure 3.8(d)). The histogram shows that the highest PCE is above 16 % with average device performance in the range of 14.5-15 %.

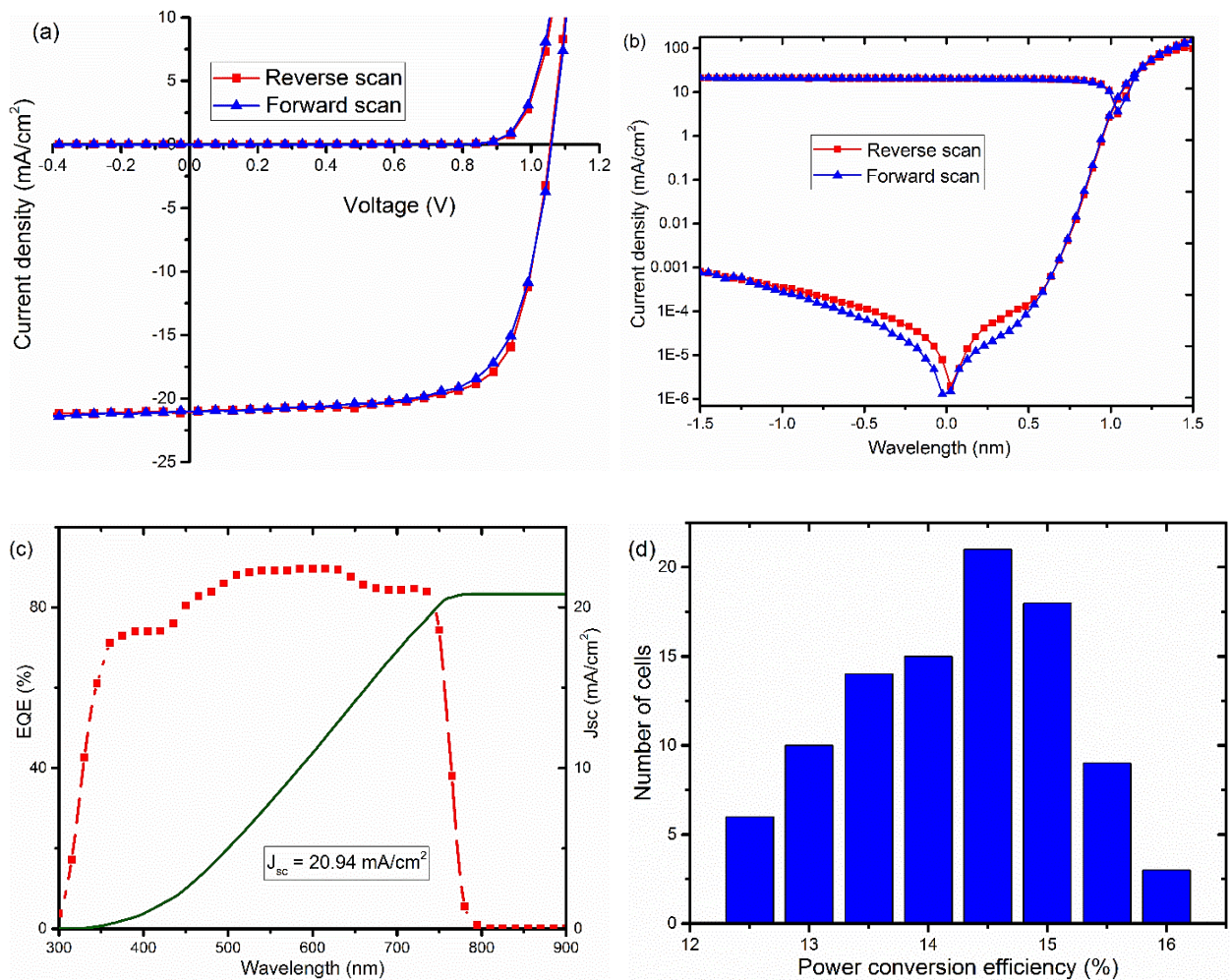


Figure 3.8. J-V curves (a) linear and (b) semi-log plots, of optimized solar cells, glass/NiO_x/Cs_{0.05}(FA_{0.83}MA_{0.17})_{0.95}PbI_{3-x}Br_x/PCBM/TiO_x/Al, recorded in dark (Dk) and under AM1.5 solar spectrum with 100 mW/cm² light intensity illumination (L). (c) External quantum efficiency (EQE) spectrum and the corresponding current density calculated from the EQE data, and (d) collective histogram of PCE distribution of PSCs with PCBM/TiO_x/Al interface structure.

	V _{oc} [V]	J _{sc} [mA/cm ²]	FF [%]	PCE [%]
Rvs-scan	1.07	21.1	72.4 ± 0.6	16.3 ± 0.2
Fwd-scan	1.07	21	70.7 ± 0.7	15.9 ± 0.2

Table 3.3. The characteristic J-V parameters (open-circuit voltage (V_{oc}), short-circuit current (J_{sc}), fill factor (FF), and power conversion efficiency (PCE) of an optimized mixed-cation mixed-halide PSCs with TiO_x interlayer (PCBM/TiO_x/Al) for the forward (Fwd) and revers scans (Rvs) under 100 mW/cm² light intensity illumination.

3.1.5. Stability Study

Device long-term stability is one of the main drawbacks challenging the shining promise of perovskite solar cells (PSCs). Although there are attempts to fabricate large scale perovskite photovoltaic modules, the issue of stability hampers the idea of large-scale fabrication. Hybrid organic-inorganic perovskite photoactive materials are prone to moisture, oxygen, UV light, and temperature degradation.^[51,134,135,136] Here, the stability of PSCs with and without TiO_x interlayer were studied to investigate the role of TiO_x interlayer on the device stability. Maximum power point (MPP) tracking measurement under the illumination of AM1.5, 100 mW/cm² intensity was applied to study the long-term stability of encapsulated devices under-continuous operation in ambient air. In parallel, long term storage stability study of devices in a glove box and under ambient conditions was conducted. Figure 3.9(a) shows the steady-state PCE and current density at MPP (J_{max}) of the sample and control devices under continuous illumination. The device with a TiO_x interlayer shows higher stability than a device without TiO_x interlayer. The device with a TiO_x interlayer shows only about 7 % and 10 % loss of J_{max} and PCE after 22 hrs continuous operation while the control device shows about 14 % and 15 % decrease in J_{max} and PCE, respectively.

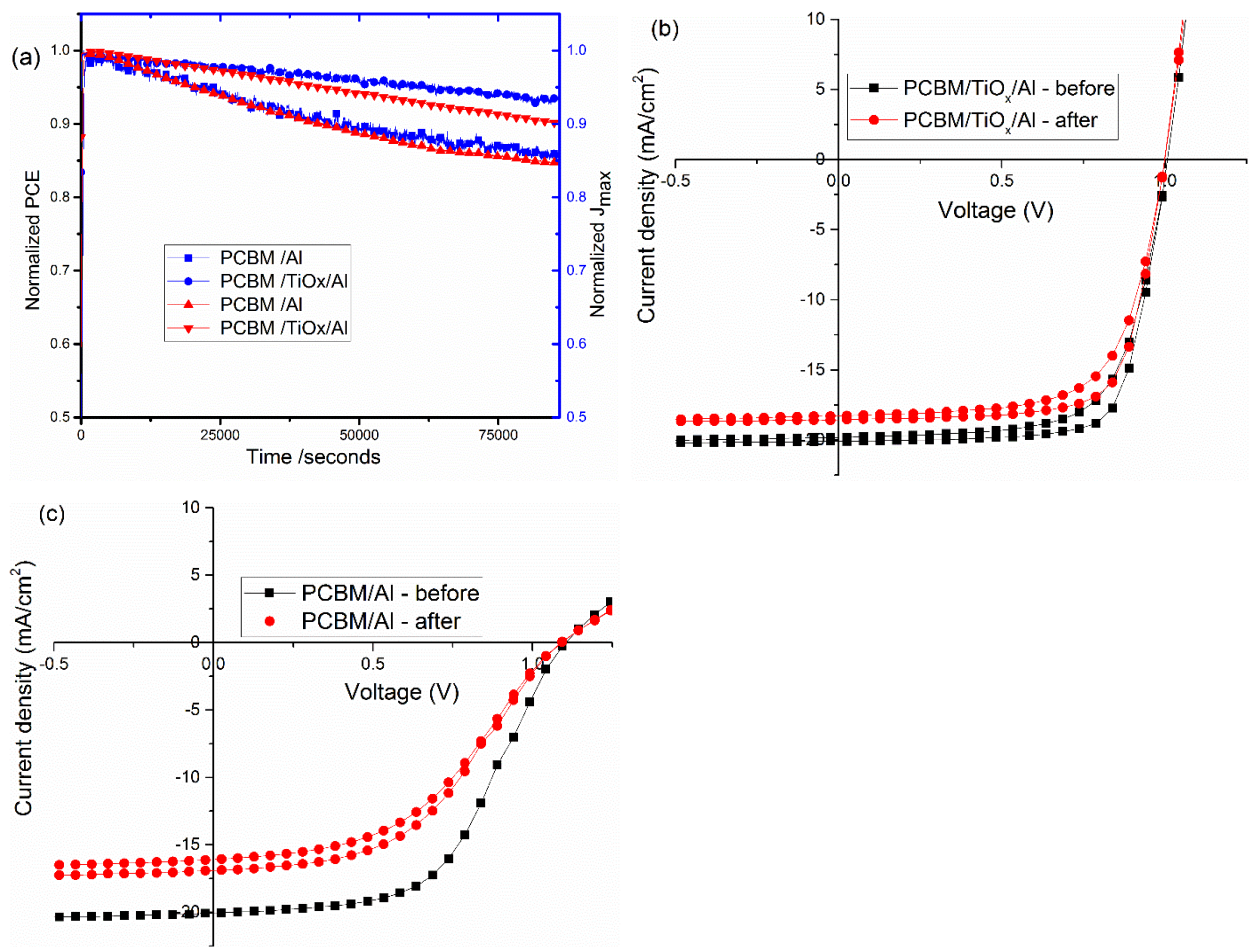


Figure 3.9. (a) The steady-state power conversion efficiency (PCE) and current density at MPP (J_{max}) under continuous illumination for about 22 hrs in ambient environment, and the J-V characteristics before and after continuous MPP-tracking for PSCs with (b) PCBM/TiO_x/AI and (c) PCBM/AI interfacings under 100 mW/cm² light intensity illumination.

ETL Interface	V_{oc} [V]	J_{sc} [mA/cm ²]	FF [%]	PCE[%]	R_p [Ω]	R_s [Ω]	Measured
PCBM/TiO _x /Al	1.01	23.9	70.1	16.9	10151	21	before
PCBM/TiO _x /Al	1	22.1	69	15.2	53588	20	after
PCBM/Al	1.09	20.5	53.3	11.9	19819	284	before
PCBM/Al	1.09	16.5	46.1	8.3	9049	366	after

Table 3.4. The average J-V characteristic of devices with TiO_x interlayer (PCBM/TiO_x/Al) and control (PCBM/Al) measured before starting maximum power tracking and after tracking for 22 hrs under 1 sun (100 mW/cm²).

The J-V characteristics of devices (Figure 3.9(b&c)) and summarized device parameters before and immediately after MPP tracking (Table 3.4) show both devices display reduced J_{sc} , FF, and PCE. The serial resistance of control devices under illumination increases from 253 Ω to 372 Ω after 22 hrs continuous MPP tracking in ambient air, while for the sample device, it is almost identical. This indicates the TiO_x interlayer helps to reduce ohmic loss in the device.

Figure 3.10 shows the stability of different devices which were stored 15 days in ambient air and another 15 days in a glob box. The device without a TiO_x interlayer shows a V_{oc} , FF, and PCE loss of about 11 %, 23 %, and 34 %, respectively. The device with TiO_x interlayer shows comparatively lower losses of V_{oc} , FF and PCE of about 4 %, 5 %, and 3 %, respectively.

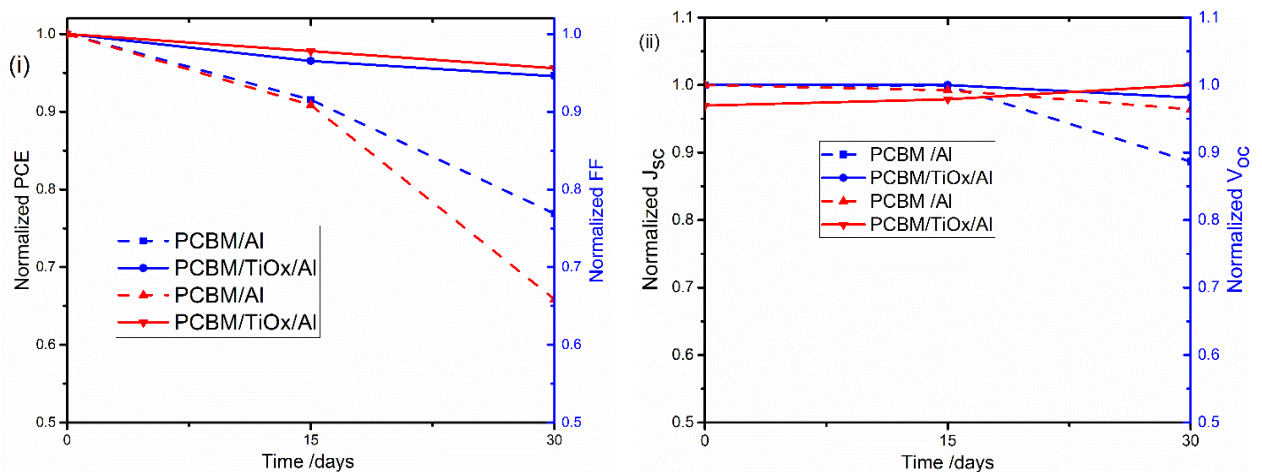


Figure 3.10. Comparative stability of PSCs with TiO_x interlayer (PCBM/TiO_x/Al) and control device (PCBM/Al structure); (i) normalized power conversion efficiency (PCE, red) and fill factor (FF, blue), and (ii) normalized open-circuit voltage (V_{oc} , blue) and short-circuit-current (J_{sc} , black) under 100 mW/cm² light intensity illumination. The devices were stored for 15 days in ambient air and another 15 days in a glob box.

Figure 3.11 shows the long-term storage stability of a device with a TiO_x interlayer stored in a glove box with oxygen and water level in the range of 0.1-10 ppm. The cell was stored for more than 90 days and its J-V characteristic was measured periodically. The device shows good stability with about 4.7 % of V_{oc} and 5 % of PCE decrease upon storage. This further indicates the stabilizing role of TiO_x interlayer.

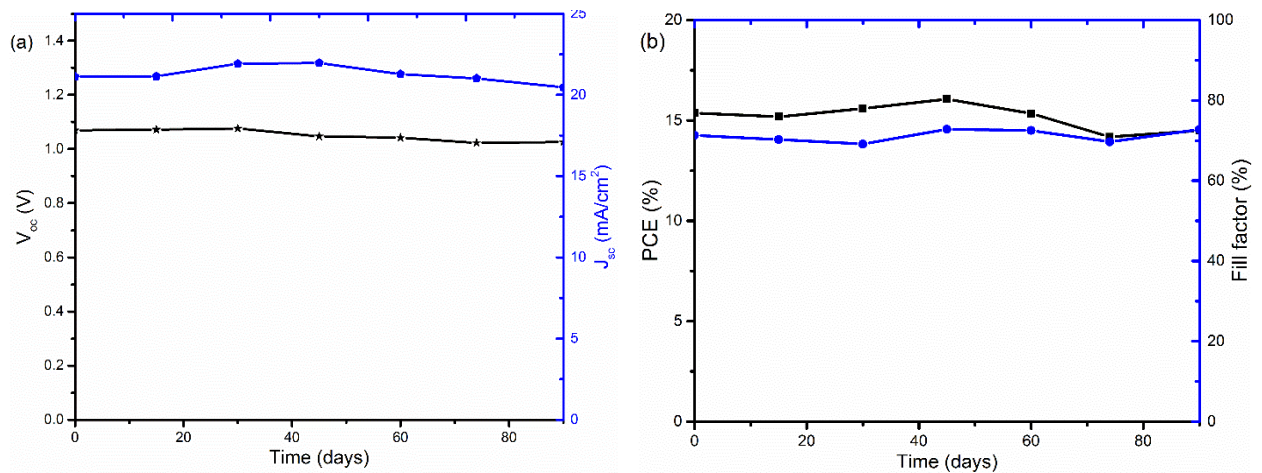


Figure 3.11. Stability of PSCs with ITO/NiO_x/Cs_{0.05}(FA_{0.83}MA_{0.17})_{0.95}PbI_{3-x}Br_x/PCBM/TiO_x/Al device structure under long term storage in a glob box, (a) open-circuit-voltage, V_{oc} (cube) and short-circuit-current, J_{sc} (sphere) , and (b) presents power conversion efficiency, PCE (cube) and fill factor (FF) (sphere) as a function of storage time.

In general, solar cells with TiO_x interlayer exhibit improved stability. The quick degradation of devices without TiO_x interlayer (Figure 3.9(a&c) and Figure 3.10) could be related to insufficient protection which leads liberation of MAI from the PVS to the PCBM/Al interface and rapid chemical reaction between the Al electrode and the perovskite and/or further exposure to the ambient environment.^[137,138] The other reason could be the degradation of the PCBM layer itself through adsorption of oxygen and water.^[139] But for devices with TiO_x already shown in the AFM observations (Figure 3.3(c)), the RMS roughness decreases when TiO_x interlayer is deposited on top of PCBM which indicate the improvement of surface smoothness and surface coverage. The TiO_x interlayer could heal pin-holes and surface defects on PCBM which might help to block direct infiltration of Al electrode to the perovskite layer. It could also reduce the probability of halide ions diffusion from the perovskite layer to the Al back electrode, and prevents corrosion of the electrode.^[131] Moreover, a TiO_x interlayer could protect the PCBM from ambient air and improve the stability. Overall, deposition of TiO_x interlayer between PCBM and Al electrode plays a dual role by reducing the energy barrier for carrier extraction and improving the stability of the solar cells.

3.1.6. Conclusion

In summary, low-temperature sol-gel processed TiO_x interlayer has proven to be a promising approach to improve device performance and stability. Devices with TiO_x interlayer show lower serial resistance (in the range 5 to 30 Ω), improved rectification in the J-V curve, and improved FF and PCE. Microscopic characterizations illustrate that the TiO_x interlayer on top of PCBM induces modification of the surface morphology and improves the surface smoothness.

EIS and IMVS measurements show higher charge transport impedance for devices without TiO_x interlayer and higher recombination impedance for devices with TiO_x interlayer. PL and EL characterizations show the improvement of charge carrier extraction process for devices with PCBM/ TiO_x /Al interfacing compared to the control devices (PCBM/Al). Moreover, devices with TiO_x interlayer show improved stability under continues operation in ambient air and long term storage in the glove box.

3.2. The Role of Polyphosphazene Buffer Layer in Inverted Mixed-Cation Mixed-Halide Perovskite Solar Cells

The findings presented in this section are published in: *Physica Status Solidi A*, 2019.

DOI: 10.1002/pssa.201900436.

Authors: Bekele Hailegnaw, Vanessa Poscher, Christoph Ulbricht, Hathaichanok Seelajaroen, Ian Teasdale, Yolanda Salinas, Niyazi Serdar Sariciftci, and Markus Clark Scharber

Polyphosphazenes are a family of inorganic/organic molecular hybrid polymers with a covalently linked phosphorus-nitrogen backbone having a general structure shown in Figure 3.12. The backbone is functionalized with two (commonly organic) substituents on the phosphorus atoms to give poly(organo)phosphazenes.^[140] The wide possible window of using different organic substituents enables the synthesis of various polyphosphazenes with different properties. Poly(organo)phosphazenes represent a versatile family of polymers with a diverse array of properties and hence applications ranging from biodegradable materials for tissue engineering^[141] and drug delivery through polymer electrolyte membranes,^[142,143] flame retardant composites or as stimuli-responsive materials have been suggested.^[144,145]

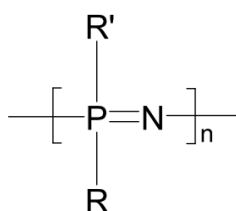


Figure 3.12. generic structure of Polyphosphazene; R can be either an alkoxy, or aryloxy, or amino group.

In this study, for the first time, a thin layer of polyphosphazene derivatives was used as a buffer layer between PCBM and back metal contact in perovskite solar cells (PSCs). Three polyphosphazene derivatives, namely poly[bis(allylamino)phosphazene] ($n \sim 5$ and $n \sim 50$) and cyclic hexa(allylamino) cyclotriphosphazene were used as an ETL interlayer for mixed-cation mixed-halide perovskite ($\text{Cs}_{0.5}(\text{FA}_{83}\text{MA}_{17})_{0.95}\text{PbI}_{3-x}\text{Br}_x$) solar cells.

3.2.1. Cyclic Voltammetry and Optical Characterization

Figure 3.13(a) shows the molecular structure of poly[bis(allylamino)phosphazene] ($n \sim 5$). Cyclic voltammetry and UV-Vis absorption techniques were used to estimate the bandgap and band energetics of poly[bis(allylamino)phosphazene] ($n \sim 5$, called “PPz5” here after). Thin-films of PPz5 on ITO coated glass substrates were deposited from 10 mg/mL of PPz5 solution (in isopropanol) followed by annealing at 100 °C for 3 min. Figure 3.13(b&c) show the cyclic voltammograms (CVs) of PPz5 which were recorded at potentials between 0 to -1.0 V in the cathodic range, and from 0 to 2.0 V in the anodic range with a scan rate of 10 mV/s. Acetonitrile containing 0.1 M tetrabutylammonium hexafluorophosphate was used as a supporting electrolyte and experiments

were performed under N₂-saturated condition. A three-electrode set-up was equipped with an ITO-coated glass as a working electrode, a Pt plate counter electrode, and a Ag/AgCl quasi-reference electrode.

The onset potentials were calibrated with a ferrocene/ferrocenium couple using 0.69 V vs. normal hydrogen electrode (NHE)^[146] and the equations 3.1 and 3.2 were used to estimate the highest occupied molecular orbital (HOMO) and the lowest unoccupied molecular orbital (LUMO) energy levels (E_{HOMO} and E_{LUMO}).^[147,148] The results suggest E_{HOMO} at around -6.5 eV, and E_{LUMO} in the range of -4.2 ± 0.1 eV. Figure 3.16(b) shows the band diagram of PPz5 together with the investigated device structure. The E_{LUMO} value suggests that PPz5 is a suitable material to be applied from the ETL side in the device specifically at the interface between the PCBM and the top contact.

$$E_{HOMO} = -(E_{[ox,onset-vs-NHE]} + 4.75) \text{ eV} \quad (3.1)$$

$$E_{LUMO} = -(E_{[red,onset-vs-NHE]} + 4.75) \text{ eV} \quad (3.2)$$

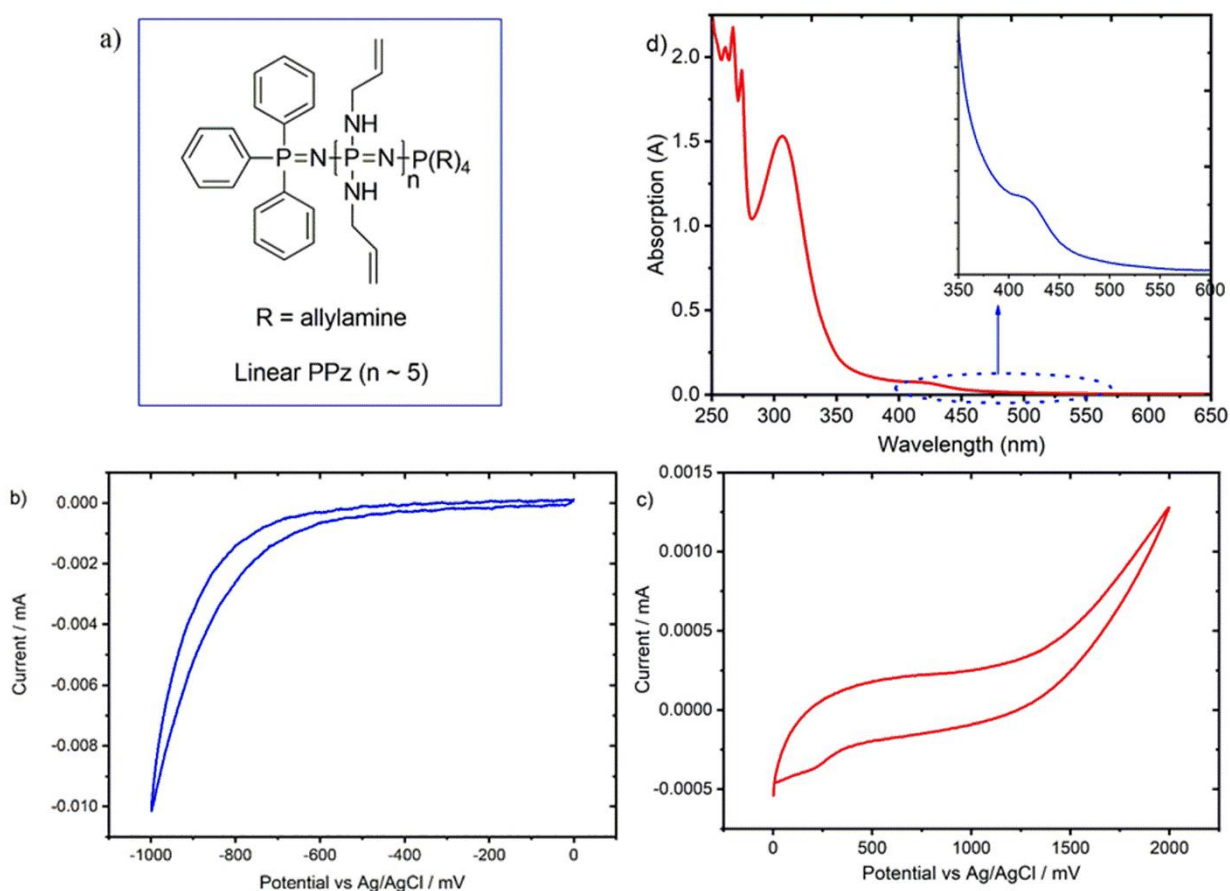


Figure 3.13. a) Chemical structure of linear poly[bis(allylamino)phosphazene] (PPz5). (b) Reductive and (c) oxidative cyclic voltammogram of PPz5 in acetonitrile (4 mg/mL) containing tetrabutylammonium hexafluorophosphate (0.1 M) as a supporting electrolyte using ITO as working electrode, Ag/AgCl reference electrode and Pt counter electrode. d) UV-Vis absorption spectrum of PPz5 solution in IPA.

The UV-Vis absorption spectrum of a PPz5 thin-film deposited on a glass substrate from isopropanol (IPA) solution is shown in Figure 3.13(d). The spectrum shows an onset wavelength around 500 nm which is in a reasonable agreement with the calculated band-gap energy obtained from the cyclic voltammogram.

To study the impact induced by the PPz5 interlayer on the charge carrier dynamics, the photoluminescence (PL) and photoluminescence decay (PLD) response of perovskite films with and without PCBM and PPz5 layers was investigated. The perovskite films were deposited on glass substrates. One film was used as a perovskite reference, another (control) was covered with PCBM and the third one (the sample) was covered with PCBM followed by PPz5 in a layer stack PVS/PCBM/PPz5. Figure 3.14(a) compares the PL spectra of different layer stacks. The film PVS/PCBM/PPz5 shows the weakest photoluminescence. This could be due to fast charge carrier transfer to the ETL, decreasing the radiative recombination process. This suggests that the deposition of PPz5 thin-layer boosts the charge carrier transfer dynamics from the photoactive layer to the ETL side. Similarly, in the PLD spectra (Figure 3.14(b)), films with PPz5 interlayer show faster PL decay as compared to films without PPz5 interlayer. This might indicate the reduction of charge trapping states at the ETL interface which reduces the slow-time radiative process (>150 ns) due to trapped charge carriers.

The bias dependent PL of PSCs with a PPz5 interlayer was measured at different applied voltages while excited by a 532 nm laser (Figure 3.14(c)), and the corresponding current-voltage (I-V) curve recorded at each voltage is shown in Figure 3.14(d). Under forward bias, the recombination current is proportional to $\exp\left(\frac{qV}{nk_B T}\right)$, where n is the ideality factor of the solar cell. The PL and the current increases moderately up to 700 mV in forward bias and exponentially at higher applied voltages. This suggests good charge carrier extraction dynamics in the device.

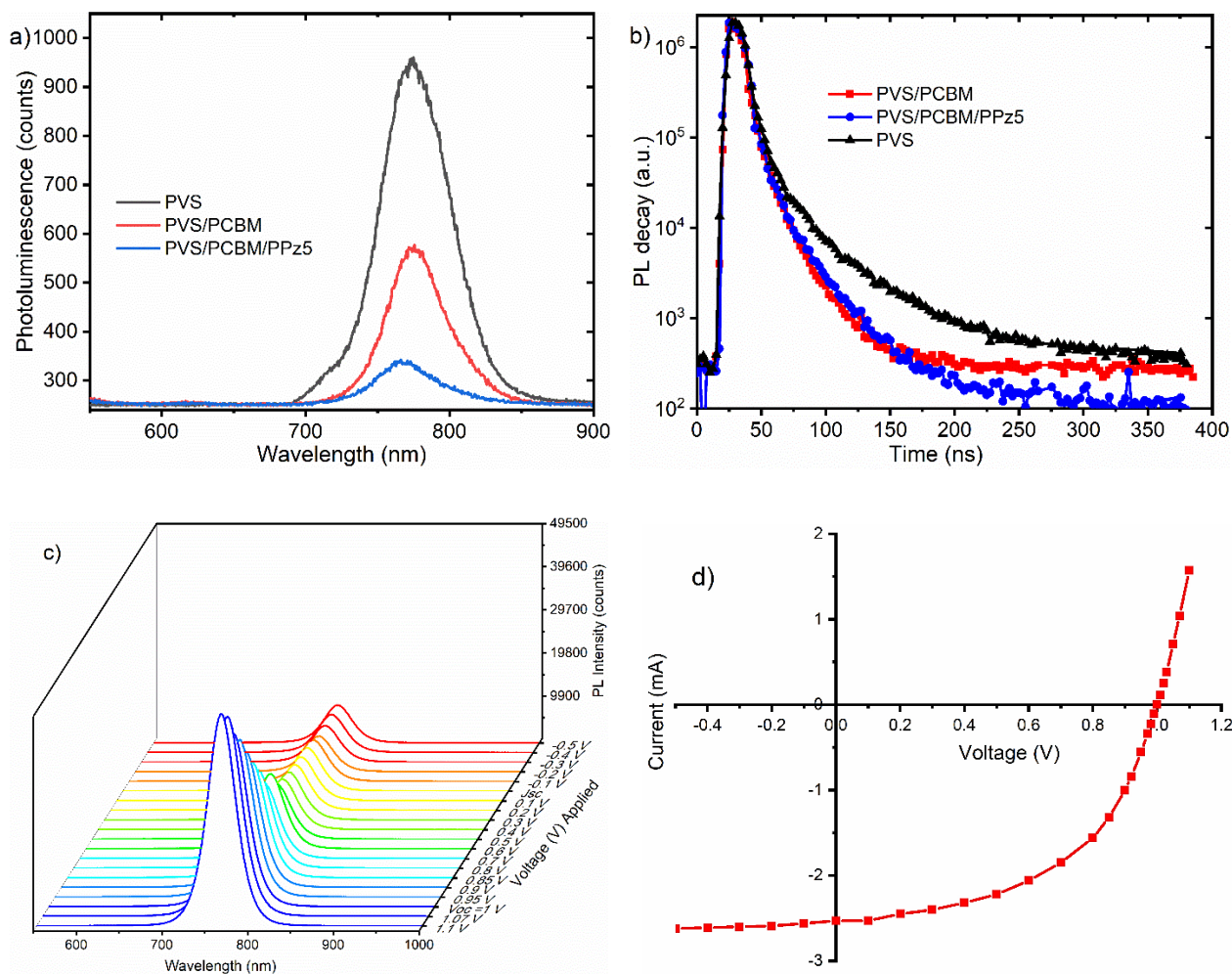


Figure 3.14. (a) Photoluminescence and (b) photoluminescence decay spectra of mixed-cation mixed-halide perovskite (PVS) film, PVS covered with PCBM (PVS/PCBM) and PVS/PCBM covered with PPz5 on top (PVS/PCBM/PPz5), and (c) Bias dependent photoluminescence of PSCs with ITO/NiO_x/PVS/PCBM/PPz5/Al structure at different bias conditions and under laser excitation (532 nm), and (d) I-V curve extracted from the PL response measurement in (c).

Topographic Profile

Figure 3.15 shows AFM topographic images of a mixed-cation mixed-halide perovskite (PVS) film, a PVS coated with PCBM and a mixed-cation mixed-halide perovskite film/PCBM stack covered with PPz5. The films were deposited on ITO coated glass substrates covered with NiO_x thin-films to mimic the interfaces in the PSCs. The perovskite film covered with PCBM (Figure 3.15(b)) shows improved surface smoothness compared to pristine perovskite films (Figure 3.15(a)). The root-mean-square (RMS) roughness (R_q) value of the film covered with PCBM is ca. 7 nm compared to 57 nm the pristine perovskite film. Further deposition of PPz5 on top of PCBM induces some morphological changes and with slight change of the RMS roughness (R_q) value to around 6.6 nm (Figure 3.15(c)). A qualitative analysis of the topographic feature of the films with PPz5 layer indicates the formation of a homogenous overcoat on top of PVS/PCBM which could cover the pin-holes of PCBM film and reduces the probability of direct contact between the photoactive layer and the back electrode.

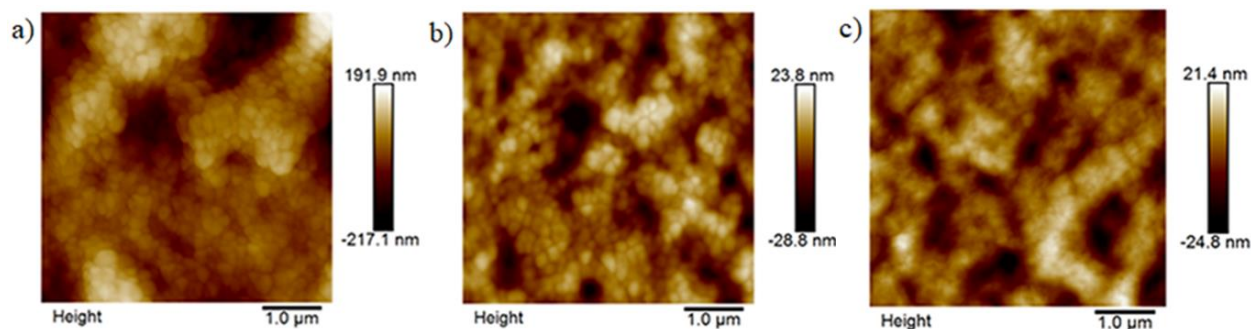


Figure 3.15. Atomic force microscope topographic images of (a) mixed-cation mixed-halide perovskite films, (b) mixed-cation mixed-halide perovskite covered with PCBM, and (c) mixed-cation mixed-halide perovskite/PCBM coated with PPz5. The films are deposited on ITO coated glass substrate covered with NiO_x nanoparticles.

3.2.2. Current Density-Voltage Response

Figure 3.16(a&b) show the schematic architecture and energy diagram of the respective layers of an inverted (p-i-n) PSCs with PPz5 (0.5 mg/mL in IPA) interlayer between the ETL (PCBM) and the back metal contact. The photocurrent density-voltage (J-V) characteristic of devices with and without PPz5 buffer layer was measured under 100 mW/cm² light intensity (AM1.5 global spectrum) (Figure 3.16(c)) and under dark conditions (Figure 3.16(d)). The photovoltaic parameters of perovskite devices are summarized in Table 3.5.

Devices with a PPz5 interlayer show improved photovoltaic properties with an average open-circuit voltage (V_{OC}) of about 1.02 V, short-circuit current density (J_{SC}) of around 20 mA/cm², fill factor (FF) of around 77 %, and power conversion efficiency (PCE) of ~16.5 %. While devices without PPz5 interlayer exhibit an average V_{OC} of about 1.01 V, J_{SC} of around 20 mA/cm², FF of about 69 % and PCE of ~12 %. As can be seen, the dark J-V curve (Figure 3.16(d)) shows that device with PPz5 interlayer exhibit improved rectification, and reduced series resistance (R_s) and leakage current. The serial resistance (R_s) and parallel resistance (R_p) values extracted from the current-voltage curves (in Figure 3.16(c)) are summarized in Table 3.5. A smaller R_s and a larger R_p values of PSC with PPz5 interlayer are consistent with the observed enhancement of device photovoltaic parameters.

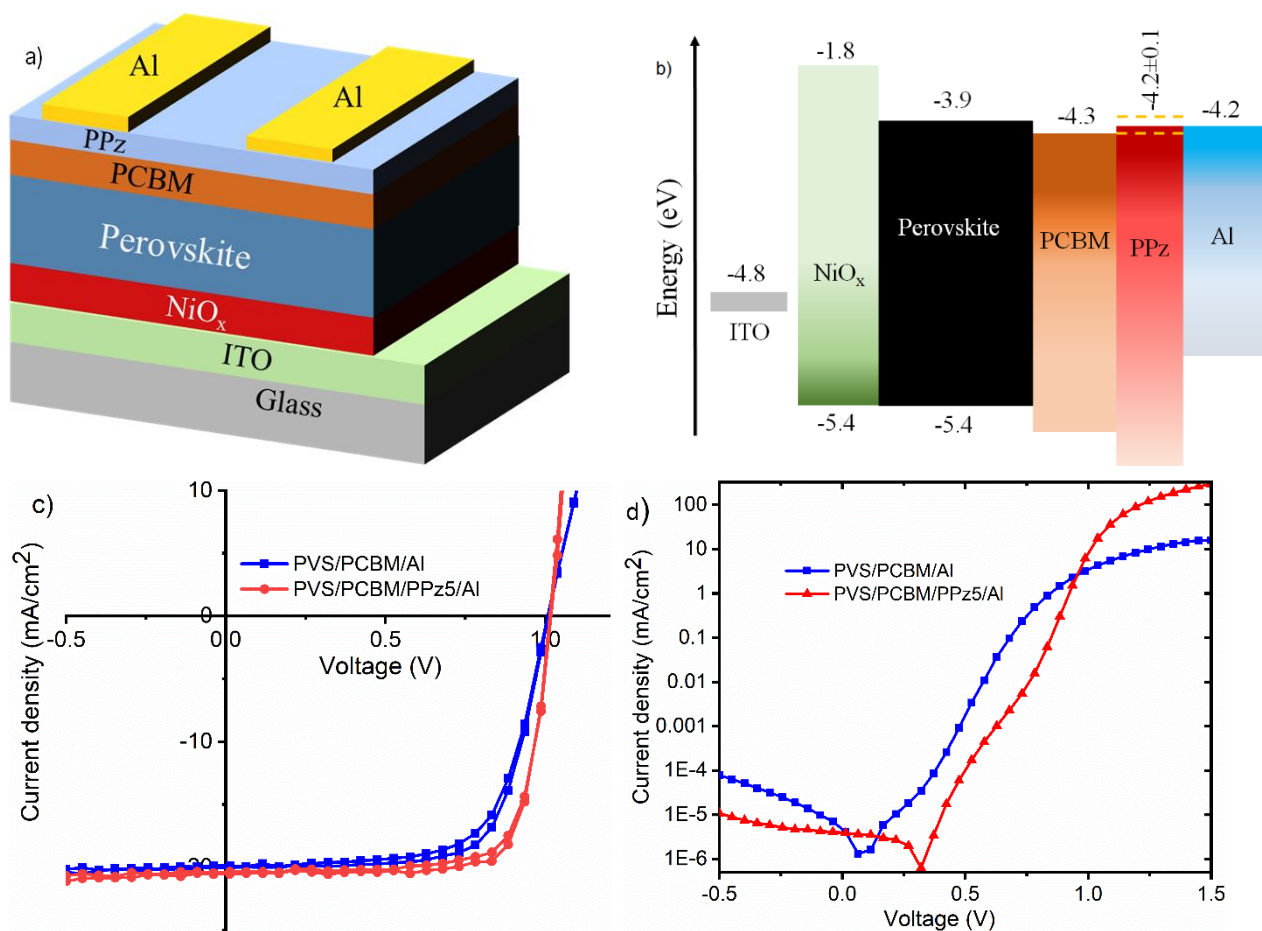


Figure 3.16. (a) Schematic structure of PSCs with polyphosphazene interlayer and (b) corresponding energy diagram of the respective layers in the cells.^[81,149] Characteristic current density-voltage (J-V) response of PSCs with (red) and without (blue) PPz5 interlayer, (c) under 1 sun light (AM1.5 solar spectrum) illumination and (d) in the dark (semi-log plot).

Type of PSCs	Scan	V _{oc} (V)	J _{sc} (mA/cm ²)	FF (%)	PCE (%)	R _s (Ohm/cm)	R _p (Ohm/cm)
PCBM/Al	Fwd	1.01	19.8	67.6	11.7	56	3862
	Rvs	1.01	20.2	70.5	12.3	58	2644
PCBM/PPz5/Al	Fwd	1.015	20.4	75.8	15.9	17	10699
	Rvs	1.016	20.5	78.7	16.9	17	5576

Table 3.5: Summarized photovoltaic parameters (i.e. V_{oc}, J_{sc}, FF, PCE, R_p and R_s) of PSCs with PPz5 interlayer (PCBM/PPz5/Al) and control devices without PPz5 interlayer (PCBM/Al) for forward (Fwd) and revers scans (Rvs) under 100 mW/cm² light intensity illumination.

3.2.1. Poly[bis(allylamino)phosphazene] ((PPz5) Thickness Optimization

The thickness of PPz5 interlayer was optimized by using different concentrations of the precursor solution. PPz5 interlayers with different thickness ranging from 5 to 30 nm were achieved via spin-coating different concentrations of PPz5 (0.25, 0.5, 1, 2, and 5 mg/mL in IPA) on top of PCBM. Figure 3.17(a) shows the J-V curves of perovskite devices with different thicknesses of a PPz5

interlayer. Devices based on 1 and 2 mg/mL PPz5 exhibit the highest J_{SC} , FF, and hence the best PCE. As the thickness of the PPz5 interlayer increases the V_{OC} of the solar cell decreases. The external quantum efficiency (EQE) spectra also confirm that a device with about 10 nm PPz5 interlayer shows the highest EQE and integrated J_{SC} (Figure 3.17(b)).

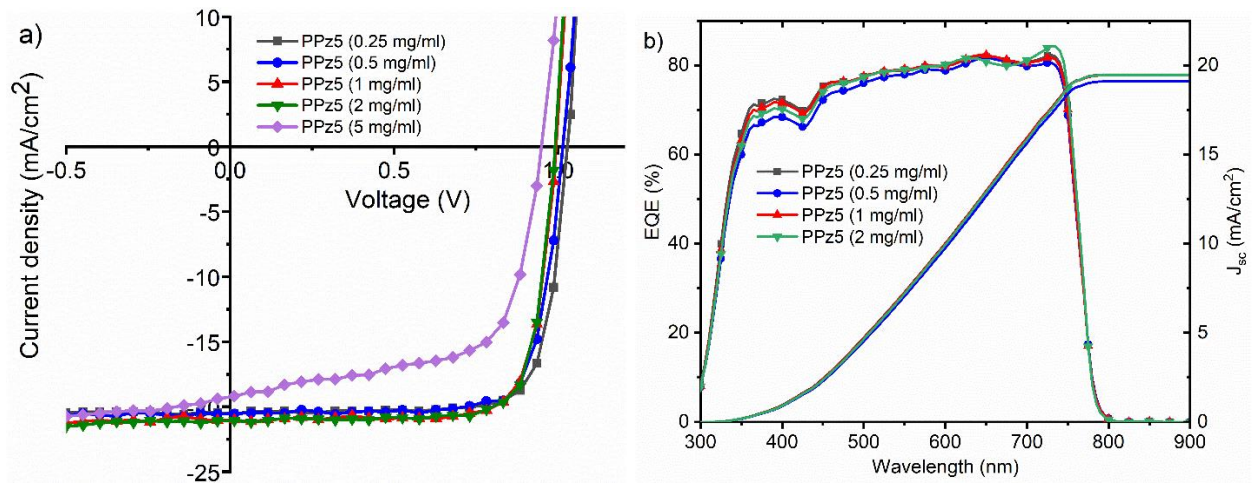


Figure 3.17. Optimization of PPz5 concentration (in mg/mL); (a) current density-voltage (J-V) characteristic of PSCs prepared with 0.25, 0.5, 1, 2 and 5 mg/mL PPz5 solutions, and (b) external quantum efficiency and integrated J_{sc} calculated from the EQE data.

Figure 3.18 shows J-V characteristics of the devices with 1, 2, and 5 mg/mL PPz5 interlayer, after one-night storage in a nitrogen glove-box. Devices based on 1 mg/mL PPz5 (which has a PPz5 layer thickness of about 10 to 15 nm) remained stable. However, solar cells with thicker PPz5 buffer layer show a substantial loss in J_{SC} , FF and overall efficiency. This indicates 1 mg/mL is the optimum concentration for our processing condition and this concentration was used hereafter.

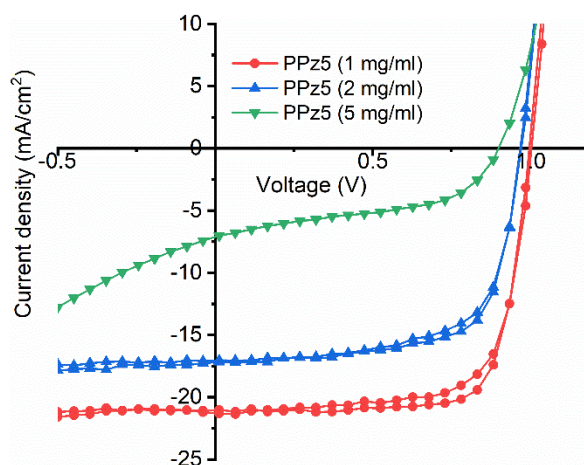


Figure 3.18. Characteristic photocurrent density-voltage (J-V) curves of mixed-cation mixed-halide perovskite solar cells (PSCs) with PPz5 interlayer (with 1, 2 and 5 mg/mL PPz5 in IPA) under simulated AM1.5 solar spectrum, 100 mW/cm² light intensity illumination. The devices were aged for 1 day in the glove-box before measurement.

The choice of a back contact electrode is another important aspect to consider while fabricating a solar cell. A good back contact electrode should be stable, economically feasible and form a suitable interface with the bottom layer for efficient charge carrier extraction. There are different choices of metals which can be applied as a back contact electrode for p-i-n PSCs. Here, the compatibility of PPz5 buffer layer with three commonly used back metal electrodes (i.e. Al, Au, and Cu) is investigated. Figure 3.19(a) shows the J-V characteristics of PSCs with PPz5 interlayer and different back metal electrodes. The current density is corrected by the active area of the cells. Devices with Al, Au, and Cu back electrodes show virtually similar photovoltaic behavior with only slight deviations in the V_{OC} . This suggests that PPz5 interlayer forms a suitable cathodic interface with these metal electrodes.

Perovskite solar cells with different PPz buffer layers (PPz5, Poly[bis(allylamino)phosphazene] (n~50) and hexa(allylamino)cyclotriphosphazene) between PCBM and Al back electrode were fabricated following the same procedure. All interlayers are processed from 1 mg/mL solution in IPA which is the optimized concentration for PPz5 as mentioned before. Figure 3.19(b) shows the J-V characteristics of PSCs with these PPz interlayers between PCBM and Al contact. PSCs with PPz5 show the highest fill factor (FF) and overall PCE. Devices with PPz50 show improvement of device V_{OC} upon repeating the J-V measurement cycle. From this, it can be concluded that, with this concentration and processing condition, PPz5 shows the best performance. However, it would be necessary to optimize the thickness of PPz50 and cyclic PPz interlayers for a comprehensive comparison.

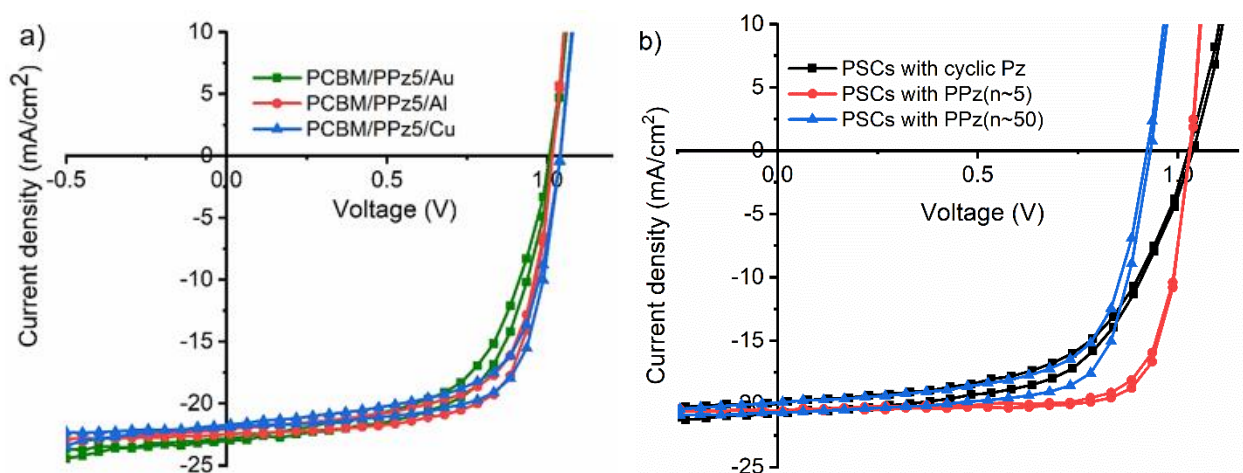


Figure 3.19. J-V curves of PSCs; (a) with different metal contact electrodes on top of PPz5 buffer layer (i.e. gold (cube), aluminum (sphere) and copper (triangle)), and (b) with allylamino cyclic phosphazene (cyclic PPz, cube), PPz5 (sphere), and linear poly[bis(allylamino)phosphazene] (n ~ 50, triangle) interlayer under 100 mW/cm² light intensity illumination.

After subsequent optimization of the processing conditions, PSCs with improved photovoltaic parameters were fabricated. Figure 3.20(a) shows the J-V curve of a PSC with PPz5 buffer layer and Table 3.6 summarizes the photovoltaic parameters calculated from the J-V data. The device exhibits a considerably low hysteresis and a power conversion efficiency of about 17.3 % under

1 sunlight (AM1.5 solar spectrum) illumination. Figure 3.20(b) shows the EQE spectrum of the best PSC with integrated short-circuit-current density (J_{sc}) of about 21.2 mA/cm². The PCE distribution of a series of samples and control devices was compared using a statistical PCE histogram. Figure 3.20(c) shows the PCE histogram for 129 PSCs with PPz interlayer and 97 PSCs without PPz interlayer which fit well with the Gaussian distribution. It shows that the average PCE of sample devices is enhanced by about 15 % compared to the control devices.

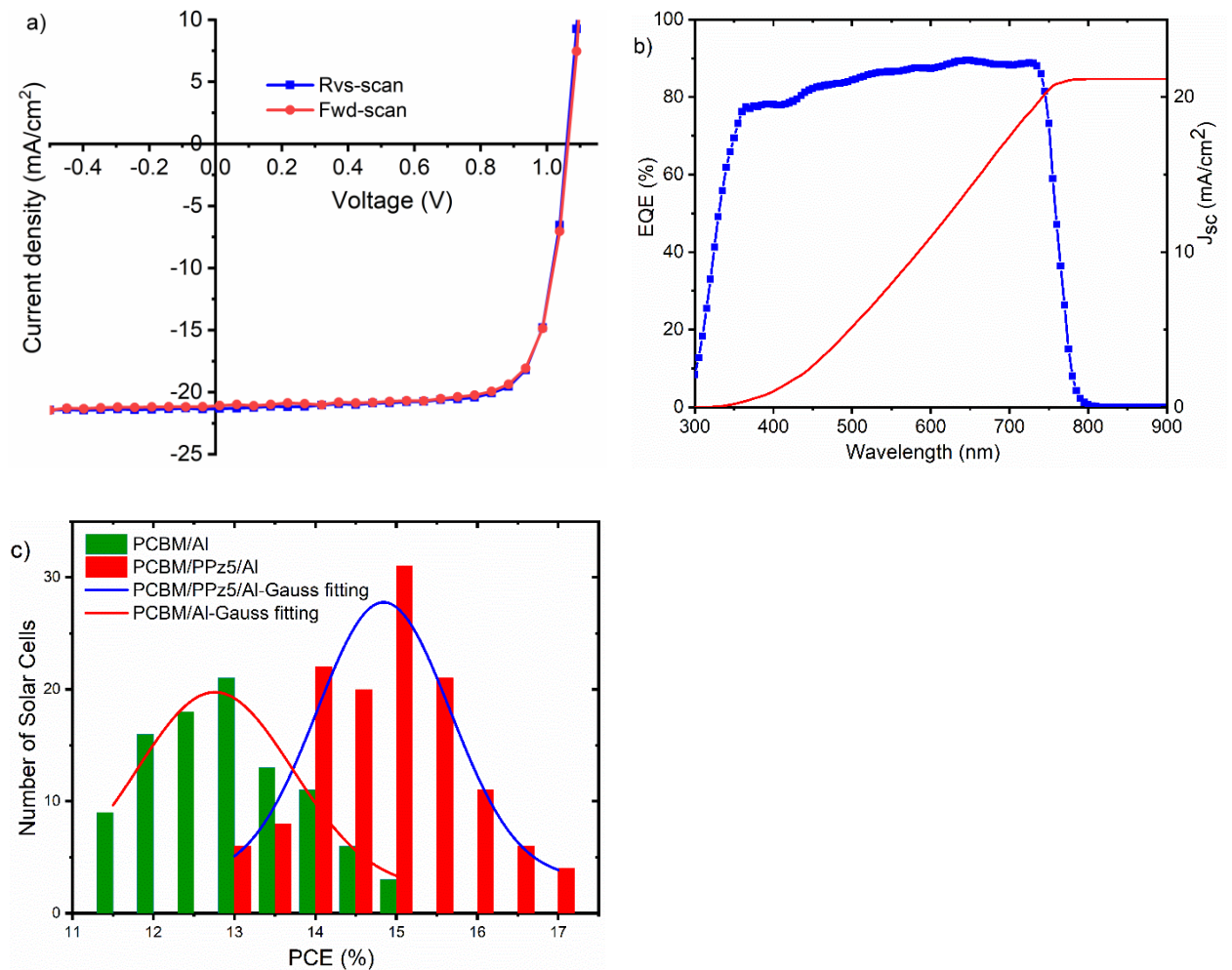


Figure 3.20. (a) J-V characteristics under AM1.5 solar spectrum (100 mW/cm² light intensity) illumination, and (b) the EQE spectrum and the corresponding integrated J_{sc} of an optimized PSCs with glass/ITO/NiO_x/Cs_{0.05}(FA_{0.83}MA_{0.17})_{0.95}PbI_{3-x}Br_x/PCBM/PPz5/AI structure. (c) The statistical power conversion efficiency (PCE) histogram of 129 devices with PPz interface (PCBM/PPz/AI) and 97 control devices (PCBM/AI).

Scan Direction	V_{oc} (V)	J_{sc} (mA/cm ²)	FF (%)	PCE (%)
Rvs-Scan	1.06	21.4	76.4	17.3
Fwd - Scan	1.06	21.1	76.3	17.1

Table 3.6: Photovoltaic parameters (V_{oc} , J_{sc} , FF and PCE) of an optimized PSCs with PPz5 interlayer (PCBM/PPz5/AI) in forward (Fwd) and revers scans (Rvs) under 100 mW/cm² light intensity illumination.

The steady-state power output of the PSC with PPz5 was studied using a MPP-tracking measurement under 100 mW/cm² simulated AM1.5 illumination. Figure 3.21(a) shows the normalized steady-state PCE and normalized current density at MPP (J_{max}) of the device under 1 sunlight illumination for 8 hrs in a N₂ glove-box. Figure 3.21(b) shows the normalized voltage at MPP (V_{max}) and the delivered electrical power output (P_{max}) of the same device. The device shows good stability over the entire recording period which indicates that PPz5 interlayer contributes to improve the device stability.

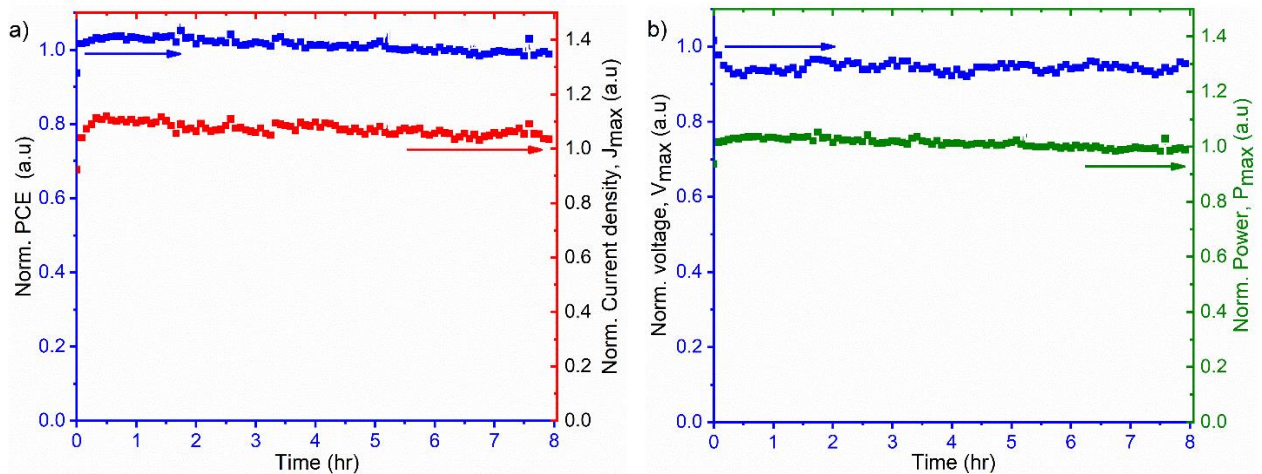


Figure 3.21. Maximum power point (MPP) tracking of PSCs with PPz5 interlayer; (a) normalized steady-state power conversion efficiency (PCE, *blue*) and normalized maximum current density (J_{max} , *red*), and (b) normalized maximum voltage (V_{max} , *blue*) and normalized fill factor (FF, *green*) under 100 mW/cm² light intensity continuous illumination inside a glove-box (N₂).

3.2.1. Impedance Spectroscopy

Further investigation of PPz5 buffer layer and its impact on the charge carrier dynamics across the interfaces of PSCs was done using a light modulated EIS and IMVS. The EIS and IMVS response of an optimized PSC with PPz (1 mg/mL) interlayer and PSC without PPz interlayer (control device) were measured in the frequency range between 1 MHz to 0.02 Hz. The EIS response of devices with PPz interlayer and control devices were measured at short-circuit condition (0 V DC voltage) and 10 mV AC-voltage under 8 mW/cm² LED light ($\lambda = 590$ nm) illumination. The IMVS responses of the same devices were measured at open-circuit voltage conditions under 8 mW/cm² LED irradiation with light intensity perturbation (10 % modulation amplitude).

Figure 3.22(a) shows the Nyquist plots of the EIS characteristics of an optimized PSC with PPz and without PPz5 interlayer, and Figure 3.22(b) represents the corresponding Bode plots. Both devices show two characteristic features in different frequency regions. The high-frequency (1 MHz-10 kHz) response is associated with the charge carrier transport resistance (R_2) across the devices, and the low-frequency (10 Hz-20 mHz) features (R_3) are associated to the impedance

of ionic diffusion and trap-states (charge recombination) at the interface of the charge transport layers.^[127,133,150,151] An equivalent circuit that describes the device structure and the EIS responses is suggested in Figure 3.22(c). The EIS response of each device was fitted using the suggested equivalent circuit to extract the fitting parameters for each circuit element. Table 3.7 summarizes the calculated fitting parameters for the sample and the control device. The result shows that PSCs with PPz5 interlayer exhibit reduced charge transport resistance ($R_2 = 44.1 \Omega$) compared to the control devices (187.5Ω). Moreover, devices with PPz interlayer show higher capacitive elements in both frequency regions, and reduced characteristic low-frequency resistance (R_3).

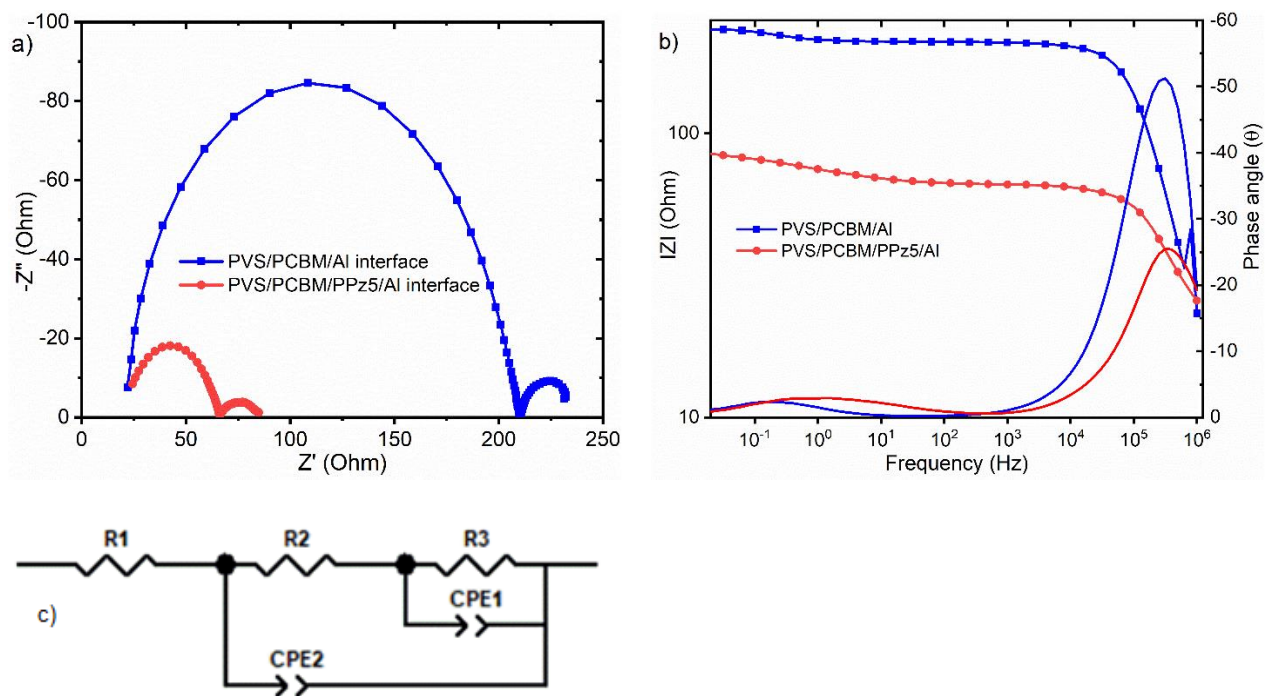


Figure 3.22. (a) Nyquist plots and (b) Bode plots of the electrochemical impedance spectroscopy (EIS) response of a PSC with PPz5 buffer layer (PCBM/PPz5/AI, *red*) and control device (PCBM/AI, *blue*), scanned in the frequency range of 1 MHz to 20 mHz with 10 % light intensity modulation amplitude under 8 mW/cm² LED light intensity. (c) Equivalent circuit model for the solar cells.

	R_s (Ω)	R_2 (Ω)	CPE2		R_3 (Ω)	CPE1	
			T2(F)	P2		T1(F)	P1
PVS/PCBM/AI	21.2	187.5	2.48e-8	0.93	23.6	0.02897	0.9
PVS/PCBM/PPz5/AI	21.2	44.1	1.05e-7	0.88	21.4	0.235	0.47

Table 3.7: Equivalent circuit fitting parameters; series resistance (R_s), geometric resistance ($R_2 = R_{tr}$), constant-phase element (CPE2) corresponding to the bulk, resistance related to interface (R_3) and interface related constant-phase element (CPE1), extracted from the fitting of EIS response of PSCs with and without PPz5 interlayer.

Figure 3.23(a&b) show the Nyquist plots and the complex transfer function versus frequency curve for the IMVS response of PSCs with and without a PPz5 interlayer. A device with a PPz5 interlayer shows a larger high-frequency semicircle which is associated with the recombination resistance.^[133] This indicates devices with PPz5 interlayer exhibit a larger recombination

resistance which could result in a reduction of recombination pathways. This can contribute to increase the charge carrier recombination time-constant and improves the probability of charge carrier extraction. Figure 3.23(c) shows the charge carrier recombination lifetime (τ_{rec}), as a function of V_{OC} which was calculated from the complex transfer function versus frequency responses of the devices at different LED light intensities (0.16, 0.8, 1.6, 3.2, 4, 4.8, 6.4, and 8 mW/cm^2). As can be seen devices with PPz5 buffer layer show longer charge carrier recombination lifetimes compared to devices without PPz5 layer.

The critical frequency which is the maximum of the complex transfer function versus frequency plot at high-frequency, is related to critical time by, $f_c = 1/2\pi\tau_c$. Moreover, the EIS response and IMVS results suggest that the presence of PPz5 buffer layer reduces the charge carrier transport resistance and enhances the recombination resistance, leading to longer charge carrier lifetimes and improved photovoltaic performance.

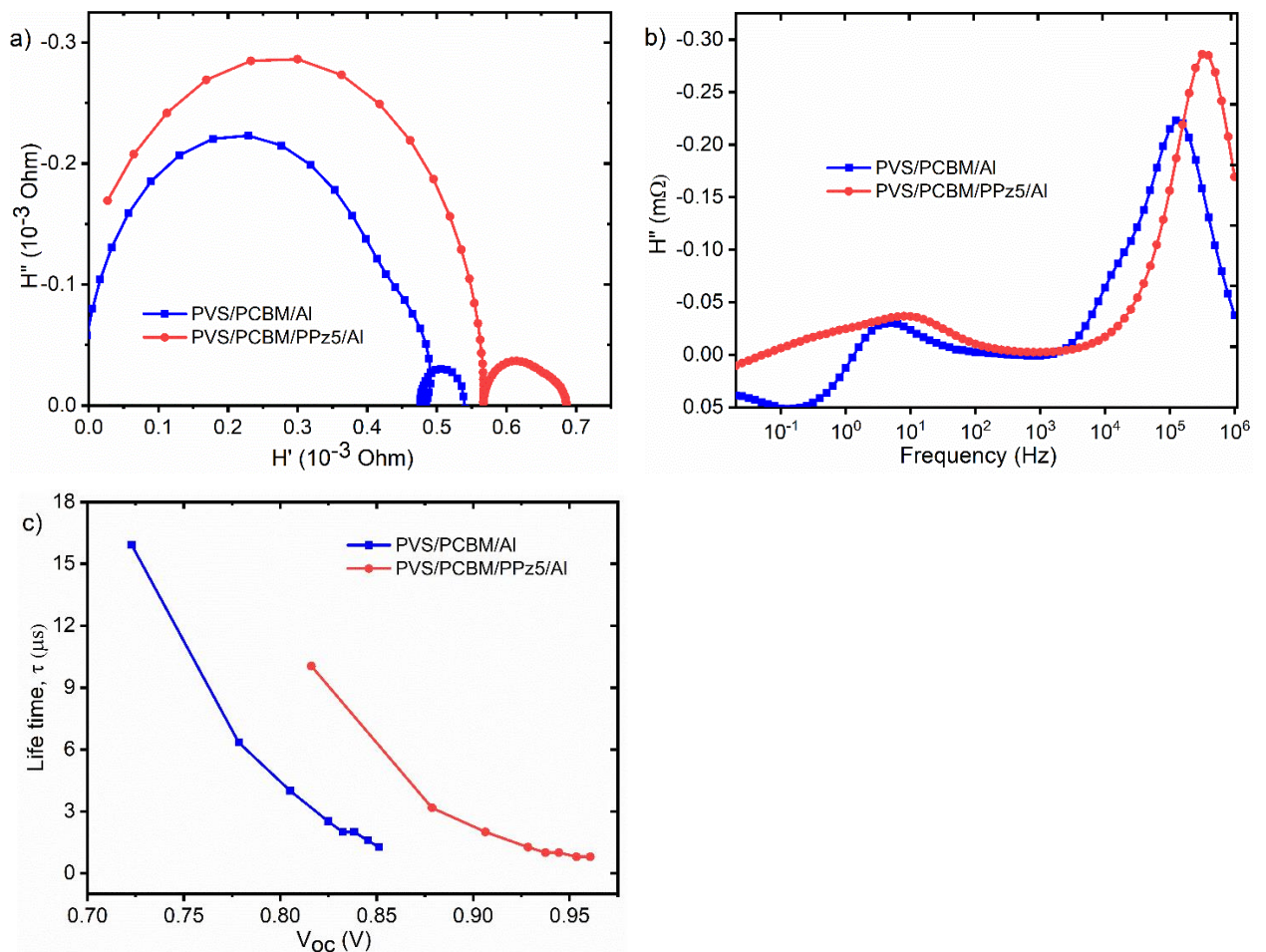


Figure 3.23. (a) The Nyquist plot, (b) complex transfer function versus frequency of the intensity modulated photovoltage spectroscopic (IMVS) response of PSCs with and without PPz5 interlayer scanned in the frequency range of 1 MHz to 20 mHz with 10 % intensity modulation amplitude under 8 mW/cm^2 LED light intensity, and (c) charge carrier life time in the PSCs as a function of open-circuit voltage extracted from IMVS response of PSCs with and without PPz5 interlayer at different LED intensities.

3.2.2. Organic Solar Cells

Further investigations on the charge carrier selectivity of PPz5 have been performed by inserting a PPz5 interlayer between the cathode/photoactive layer or anode/photoactive layer in organic solar cells. An inverted (n-i-p) configuration P3HT:PCBM based bulk-heterojunction solar cells (BHJSCs) was fabricated in which PPz5 was used as a cathodic interface as schematically depicted in Figure 3.24(a). For comparison devices with a polyethyleneimine (PEI) were prepared. Figure 3.24(b&c) show the J-V curves of BHJSCs with PPz5, PEI or PEI/PPz5 as a cathodic interlayer. All devices show reasonable J-V characteristics, suggesting that PPz5 works as a buffer layer between the photoactive organic semiconductor and the cathode.

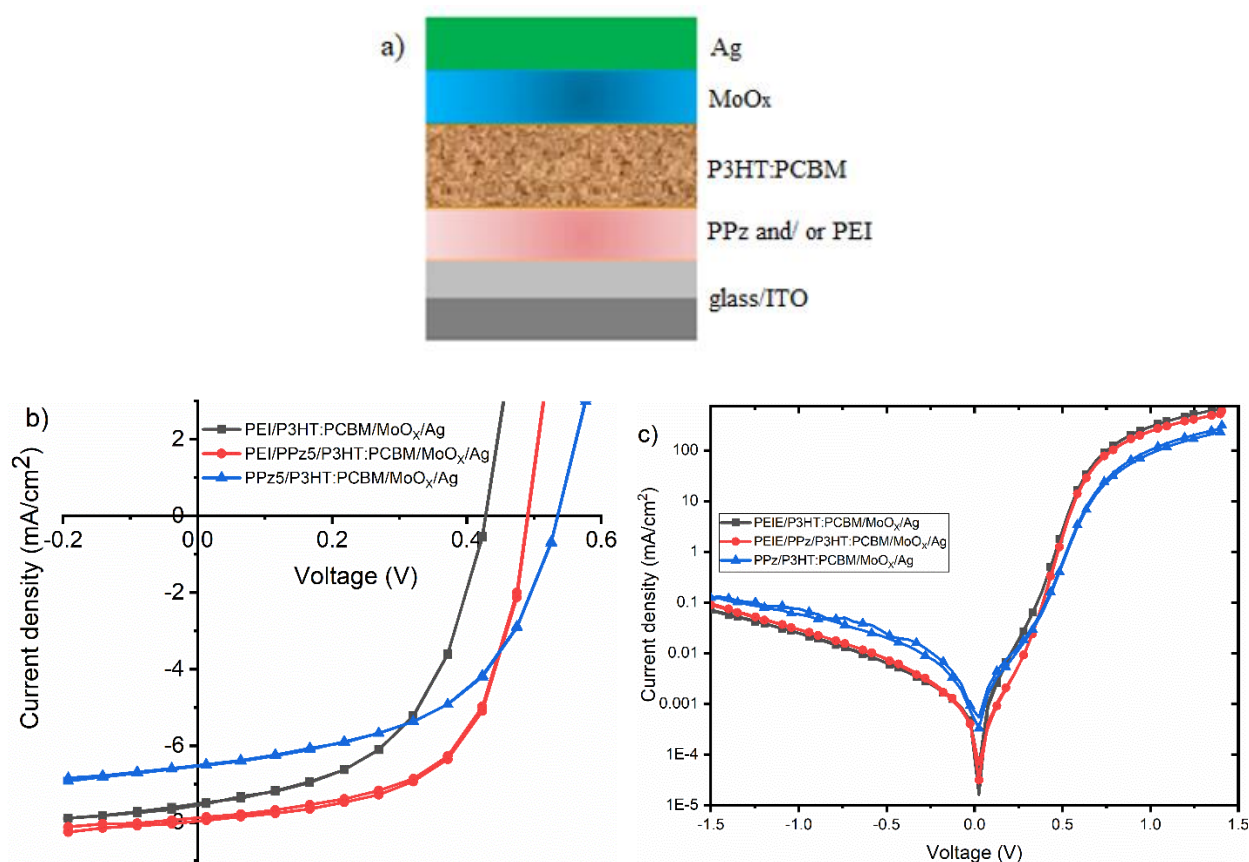


Figure 3.24. (a) Schematic representation of n-i-p bulk-heterojunction solar cells with PPz5 and/ or PEI as a cathodic interlayer. (b) linear and (c) semi-log J-V characteristics of P3HT:PCBM based BHJSCs using PPz5, PEI or PEI/PPz5 interlayers under 1 sun light illumination.

P3HT:PCBM BHJSCs in the normal (p-i-n) configuration were fabricated using PPz5 or PEDOT:PSS deposited on ITO coated glass substrates (Figure 3.25(a)). Figure 3.25(b) shows the J-V curves of BHJSCs with PPz5 and PEDOT:PSS interlayer as HTL. Devices with PEDOT:PSS HTL shows the expected photodiode behavior. However, devices with PPz5 do not show any photovoltaic behavior suggesting that PPz5 is not a good buffer layer between the absorber layer and the anode electrode.

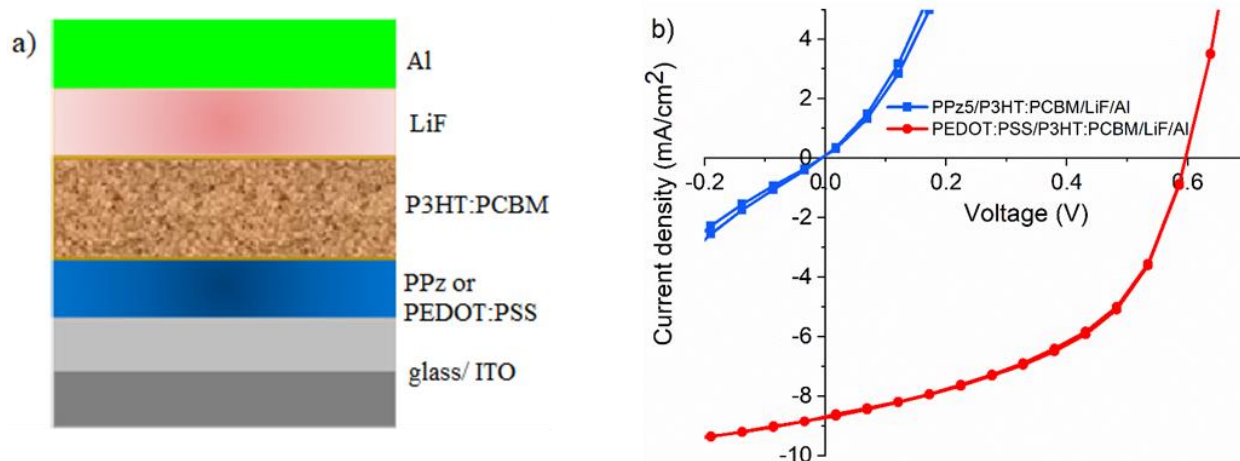


Figure 3.25. (a) Schematic representation of p-i-n BHJSCs with PPz5 or PEDOT: PSS as a hole transport layer (HTL), and (b) characteristic J-V curves of P3HT:PCBM based BHJSCs with PPz5 or PEDOT: PSS as HTLs under 1 sun light illumination.

3.2.3. Conclusion

In summary, these experiments illustrate the role of a thin layer of polyphosphazene derivatives, as a buffer layer between PCBM and back metal-contact in mixed-cation mixed-halide perovskite solar cells (PSCs). PSCs with PPz5 interlayer show an enhanced rectification in the J-V curves with reduced hysteresis and improved photovoltaic properties. The thickness of the PPz5 interlayer was optimized, and the best PSC shows an average V_{oc} of ~ 1.06 V, J_{sc} of ~ 21.4 mA/cm², FF of ~ 76.4 %, and PCE of ~ 17.3 % for the forward and reverse scan under AM1.5 solar spectrum (100 mW/cm²) illumination. PL and PL-decay investigations reveal the improvement of charge carrier transfer in the presence of a PPz interlayer. The EIS responses of devices with PPz interlayer show lower charge transport resistance compared to devices without PPz interlayer. Analogously, solar cells with PPz interlayer show larger recombination impedance in the IMVS measurements compared to devices without PPz interlayer. This suggests that the presence of PPz interlayer in the device helps to improve the charge transport process and to reduce the recombination paths. This improves the charge carrier extraction process across the ETL interfaces. Moreover, the application of PPz5 in organic solar cells indicates that a PPz interfacial layer supports preferentially the electron extraction process at the cathode. Furthermore, the merit of applying PPz5 interlayer extends to the possibility of using different metals (such as aluminum, gold, copper, and silver) as a top contact electrode. This investigation reveals that the application of a PPz derivative as an interlayer material is a promising approach to improve the interface between the ETL/metal electrode and to improve the performance and stability of PSCs.

3.3. Solvent Additive In Mixed-Halide Perovskite Solar cells

Results and findings described here are published in: *ACS Journal of Physical Chemistry C*, 2019.

DOI: 10.1021/acs.jpcc.9b05058

Authors: Bekele Hailegnaw, Getachew Adam, Dominik Wielend, Johannes David Pedarnig, Niyazi Serdar Sariciftci and Markus Clark Scharber

As mentioned in the introduction, compositional engineering, interfacial engineering, modifying the processing conditions, and applying different additives are among the different approaches used to maximize the photophysical properties, and improve the PCE and stability of PSCs.^[152-155] The additive approach involves the application of a solvent additive and/or a compositional additive to modify the crystallization and film formation process of the photoactive layer.^[69,156] Solvent Additive is one of the most commonly applied and investigated method which has proven to be a promising and easy approach to improve the perovskite film morphology, charge transport, excitonic and optical behaviors, and to boost the performance of PSCs.^[71,74,155,157]

3.3.1. Acetylacetone Solvent Additive

Acetylacetone (AA) is an organic compound with the molecular formula $\text{CH}_3\text{COCH}_2\text{COCH}_3$. It is a class of 1,3-diketone which exists in equilibrium with its keto-enol tautomer ($\text{CH}_3\text{C}(\text{O})\text{CH}=\text{C}(\text{OH})\text{CH}_3$). It is an important bidentate ligand in coordination chemistry which can form complexes with most transition metals. Herein, the effect of AA as a solvent additive for $\text{MAPbI}_{3-x}\text{Cl}_x$ perovskite is presented.

3.3.2. Crystallographic and Optical Results

Figure 3.26(a) shows the images of $\text{MAPbI}_{3-x}\text{Cl}_x$ films with and without AA additive. Figure 3.26(b) shows the structural formula of AA additive. Comparing the two images qualitatively, $\text{MAPbI}_{3-x}\text{Cl}_x$ films with AA additive appear more black and shiny compared to the control film. This might be related to the fact that AA forms a complex with the Pb^{2+} cation and form coordination via two keto-oxygen ligands to yield bis(acetylacetonato)lead(II) complexes.^[158,159] Formation of such complex intermediate could regulate the crystal growth kinetics and hence the perovskite film formation similar to DMSO-PbI_2 complex.^[101] Such coordination could improve the complete conversion of the perovskite with enhanced crystalline uniformity.

X-ray diffraction (XRD, Bruker D8 XRD system) employing Cu-K α radiation source ($\lambda = 1.5418 \text{ \AA}$) at 40 kV and 20 mA power source was used to characterize the perovskite films with and without AA additive. Figure 3.26(c) shows the XRD spectra of $\text{MAPbI}_{3-x}\text{Cl}_x$ films with and without AA additive deposited on glass substrates. The diffraction spectra of both $\text{MAPbI}_{3-x}\text{Cl}_x$ films show similar diffraction peaks at about 15° , 25° , 29.5° , and 32.5° which corresponds to the diffraction peaks of (110), (202), (220) and (310) crystal planes of the tetragonal $\text{MAPbI}_{3-x}\text{Cl}_x$ phase,

respectively.^[160-163] The lattice parameters of MAPbI_{3-x}Cl_x films are around $a \approx 8.4$ and $c \approx 13.4$ Å. This could indicate that the additive involves in the crystal growth and escapes during the heat treatment which is in good agreement with the suggested hypothesis above.

To check the energetics of the film with AA additive in comparison with the control film UV-Vis transmittance measurements were used. Figure 3.26(d) shows that the transmittance spectra of MAPbI_{3-x}Cl_x films with and without AA additive deposited on glass substrates. Both films display comparable responses, though films with AA additive show more transmittance in the longer wavelength (above 800). This negligible variation could be related to reflection and refraction. From this, it can be concluded that incorporation of AA additive does not modify the band-gap of the resulting perovskite films.

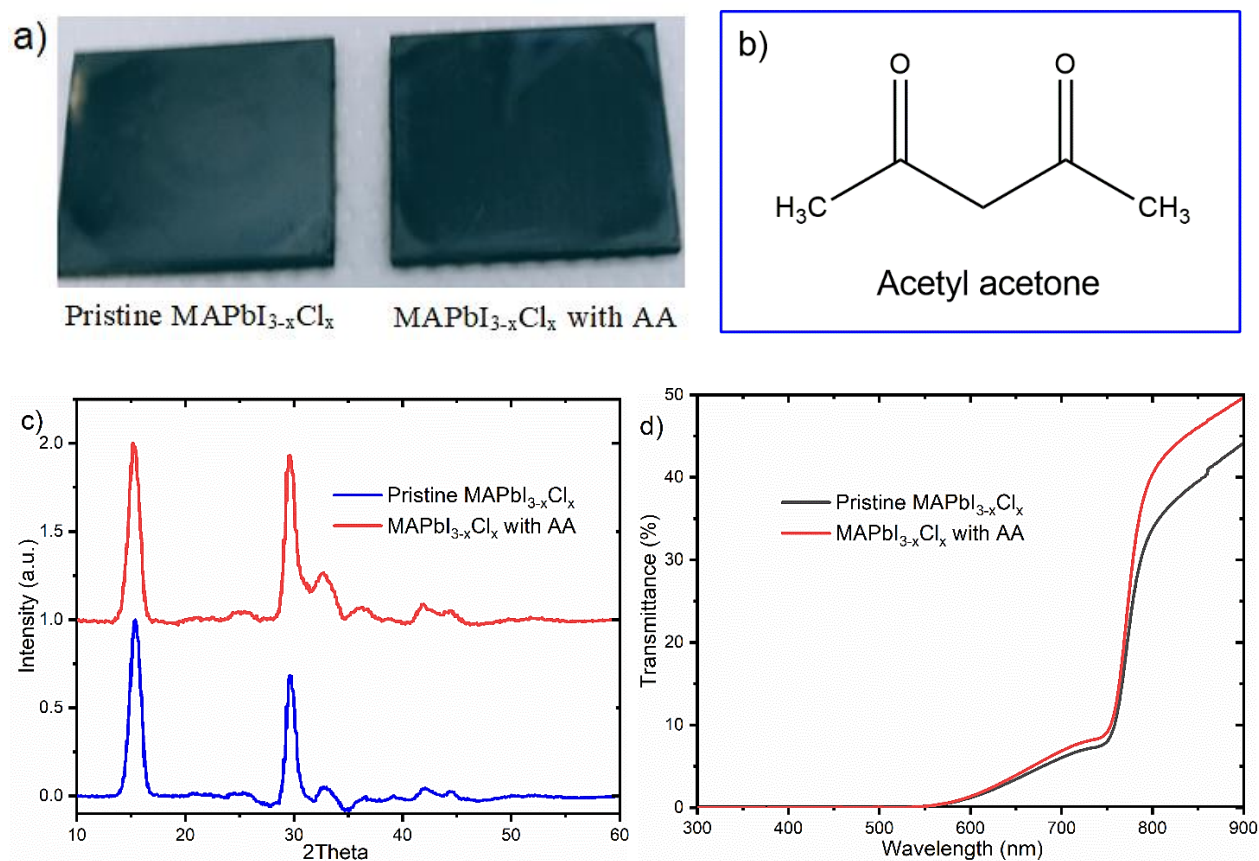


Figure 3.26. a) Picture of MAPbI_{3-x}Cl_x perovskite films with and without AA additive, and b) the molecular structure of acetylacetone (AA). c) X-ray diffraction spectra and d) UV-Vis transmittance spectra of MAPbI_{3-x}Cl_x films with and without AA additive.

Photoluminescence (PL) Spectra

To verify the effect of acetylacetone (AA) additive on the photoexcited charge carrier dynamics and recombination, the photoluminescence (PL) of MAPbI_{3-x}Cl_x films processed with and without the additive was evaluated. Figure 3.27(a&b) show the PL spectra of MAPbI_{3-x}Cl_x films with the same layer thickness which were deposited on ITO, and glass/PEDOT:PSS substrates.

Regardless of the substrates, MAPbI_{3-x}Cl_x films with AA additive exhibit higher photoluminescence intensities compared to the control films. This suggests that AA additive plays a vital role to improve the film quality and to reduce the trap density and recombination channels in the film. This reduces the non-radiative recombination process, and enhances the radiative recombination and hence increases the PL intensity. As the defect density decreases, the photon energy utilization in the PSCs could increase, and hence improve the open-circuit voltage (V_{OC}), short-circuit current density (J_{SC}) and overall device performance.

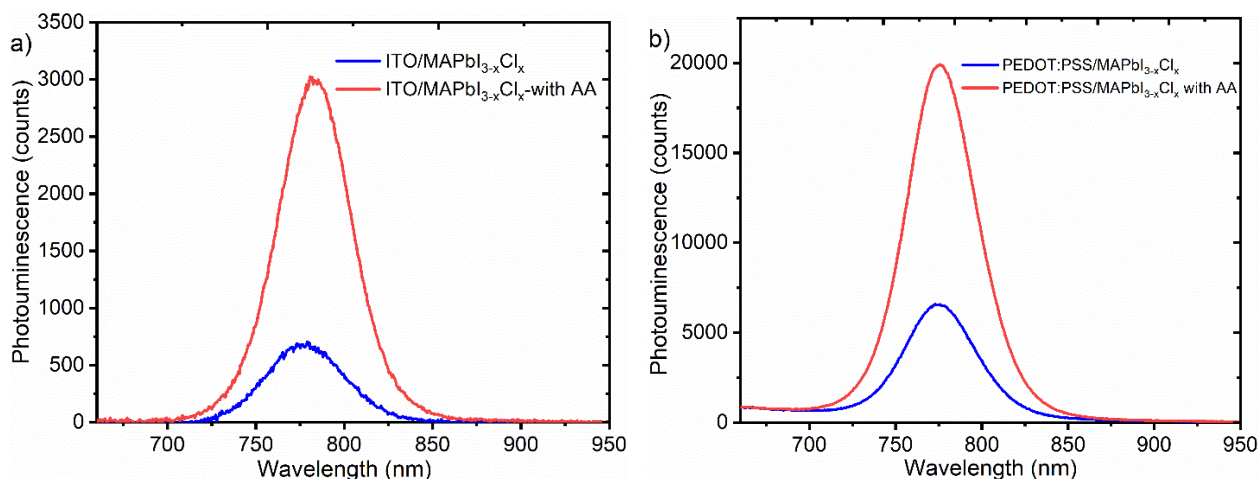


Figure 3.27. The photoluminescence of MAPbI_{3-x}Cl_x perovskite films with AA additive (red) and without AA additive (blue) deposited on; (a) indium tin oxide coated glass substrates, and (b) PEDOT:PSS coated glass substrates.

Topographic Profile

Atomic force microscopy and scanning electron microscopy imaging were applied to investigate the morphological changes in the MAPbI_{3-x}Cl_x films due to the AA additive. MAPbI_{3-x}Cl_x films with 10 % (v/v) AA and MAPbI_{3-x}Cl_x (pristine) films were deposited on ITO coated glass substrates covered with PEDOT:PSS. Figure 3.28(a&c) show the topographic and corresponding tapping forward AFM images of MAPbI_{3-x}Cl_x perovskite film, and Figure 3.28(b&d) show the topographic and tapping forward AFM images of MAPbI_{3-x}Cl_x film with AA additive, respectively. Figure 3.29(a&b) show SEM images of MAPbI_{3-x}Cl_x perovskite (pristine) films and MAPbI_{3-x}Cl_x perovskite films with AA additive, respectively. As one can see MAPbI_{3-x}Cl_x films with AA additive show enhanced crystallinity and clear grain boundaries compared to the MAPbI_{3-x}Cl_x films processed without AA additive. The root-mean-square (RMS) roughness (R_q) calculated from AFM data shows that the additive improves the surface smoothness of the films. The RMS value for MAPbI_{3-x}Cl_x films with AA additive is reduced to about 38.5 nm compared to 47.9 nm for films processed without additive. The SEM images show that films with AA additive show comparatively medium crystal domains with symmetric size and shape distribution, and with reduced surface defects which is in a good correlation with the AFM data.

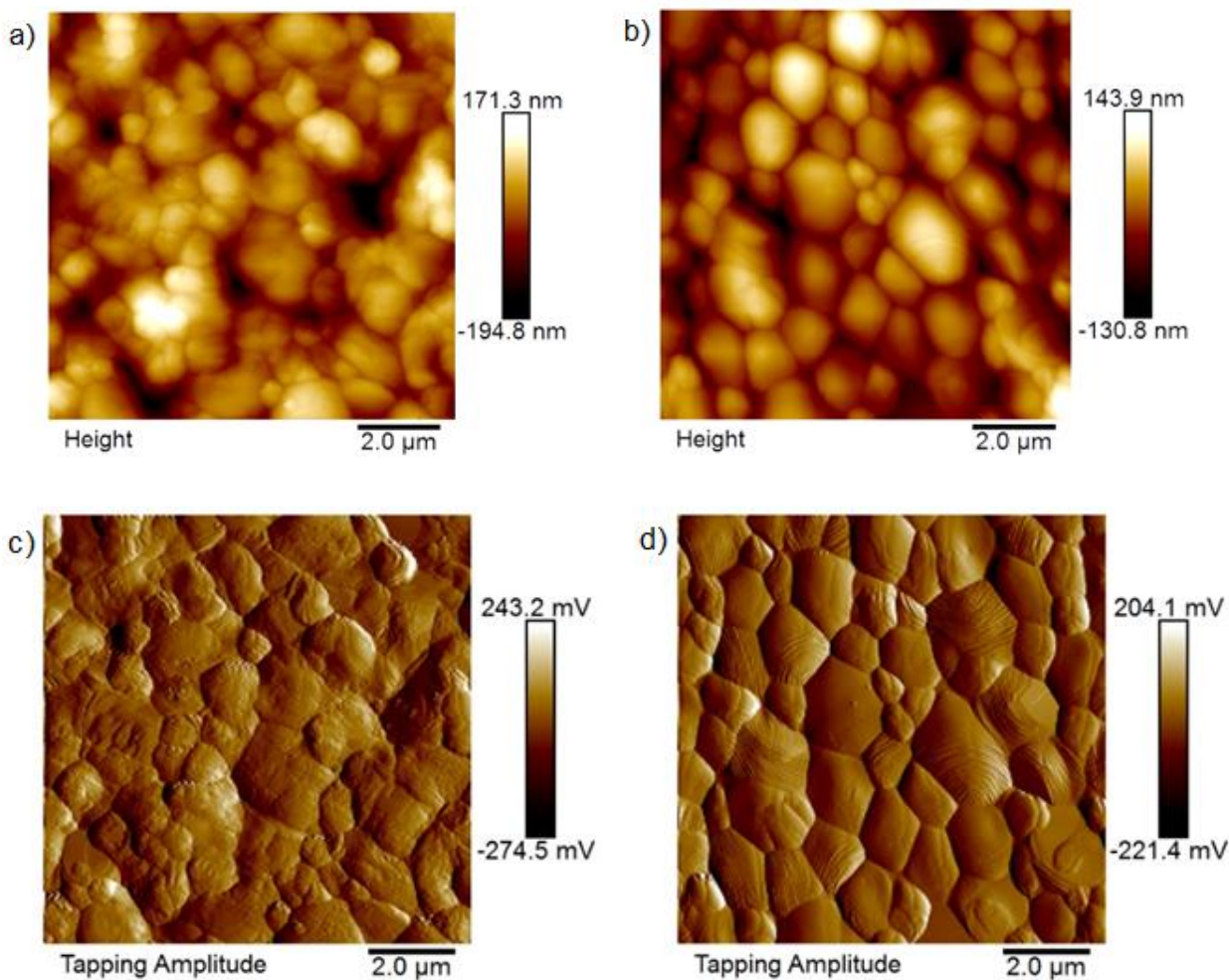


Figure 3.28. Atomic force microscope images; topographic images of a) pristine $\text{MAPbI}_{3-x}\text{Cl}_x$ and b) $\text{MAPbI}_{3-x}\text{Cl}_x$ with AA additive films, and tapping images of perovskite films, c) pristine and d) $\text{MAPbI}_{3-x}\text{Cl}_x$ with AA additive. The films are deposited on ITO coated glass substrate covered with PEDOT:PSS.

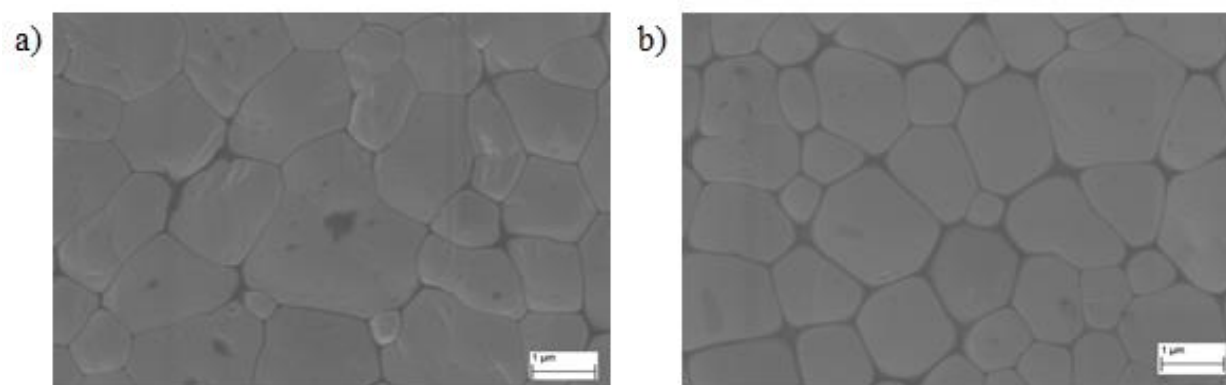


Figure 3.29. Scanning electron microscope (SEM) topographic images of a) $\text{MAPbI}_{3-x}\text{Cl}_x$ (pristine) and b) $\text{MAPbI}_{3-x}\text{Cl}_x$ with AA additive films deposited on top of PEDOT:PSS thin film on indium tin oxide coated glass substrates (glass/ITO/PEDOT:PSS).

3.3.3. Space-Charge-Limited Current (SCLC)

The space-charge-limited current technique was utilized to estimate the trap-state density in MAPbI_{3-x}Cl_x perovskite films processed with and without AA additive. Hole only devices were fabricated via sandwiching the MAPbI_{3-x}Cl_x perovskite films between ITO/PEDOT:PSS and PEDOT:PSS/Au contacts (Figure 3.30(a)). Figure 3.30(b) shows the photocurrent density-voltage (J-V) curves of the prepared hole only devices. As mentioned above (section 2.4.5.4.), the trap-space-charge regime is identified by its dramatic increase of the current injection in the range of 1.9 to 4 V bias. To calculate the hole-trap density in the devices equation 2.1 was applied using the dielectric constant of 32.5 and thickness of 500 nm for MAPbI_{3-x}Cl_x perovskite films. The calculated hole-trap density for MAPbI_{3-x}Cl_x perovskite with AA is about $2.4 \times 10^{16} \text{ cm}^{-3}$, which is lower compared to the control device (MAPbI_{3-x}Cl_x perovskite without additive which is around $4.3 \times 10^{16} \text{ cm}^{-3}$). This suggests that AA additive plays a vital role to fabricate MAPbI_{3-x}Cl_x films with improved film quality and reduced trap-state density. This is in good agreement with the improved photoluminescence response observed for films with AA additive.

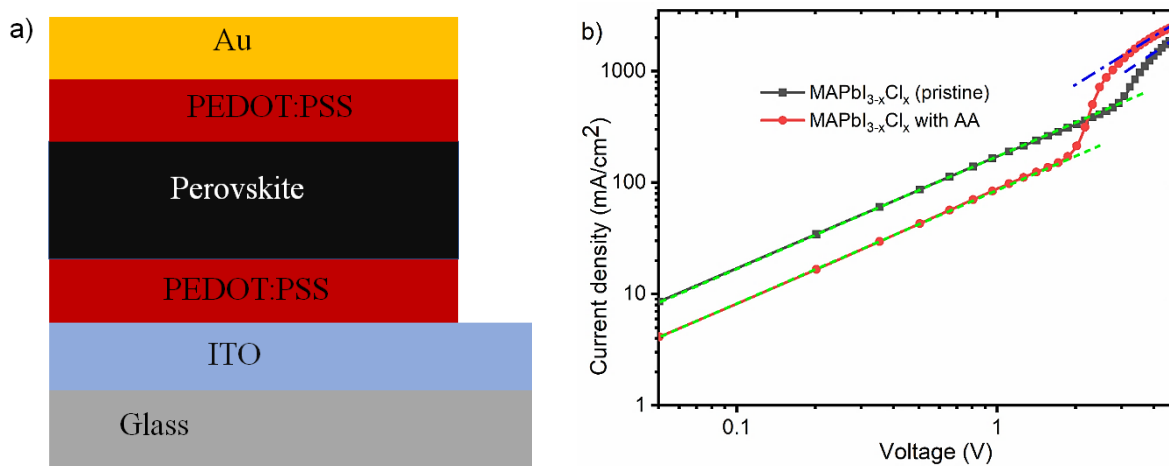


Figure 3.30. (a) Hole only device structure, and (b) J-V curves of hole only devices MAPbI_{3-x}Cl_x perovskite with and without AA additive in which the ohmic regions (fitted by green lines), the space charge limited current regions (fitted with blue lines) and in between the trap-filled regions.

3.3.4. Current Density-Voltage Response

Figure 3.31(a) shows a schematic representation of a p-i-n PSC. Figure 3.31(b) displays the photovoltaic properties of PSCs with an active area of 0.16 cm² processed from MAPbI_{3-x}Cl_x precursor solutions containing different percent concentrations (0, 5, 10, 15 and 20 vol %) of AA solvent additive. As can be seen, the device with 10 vol % AA additive shows the best J_{SC}, FF and PCE. The external quantum efficiency (Figure 3.31(c)) depicts that, the device with 10 vol % AA additive shows the highest EQE and integrated J_{SC} followed by devices with 15, 20, and 5 vol% AA additive in decreasing order.

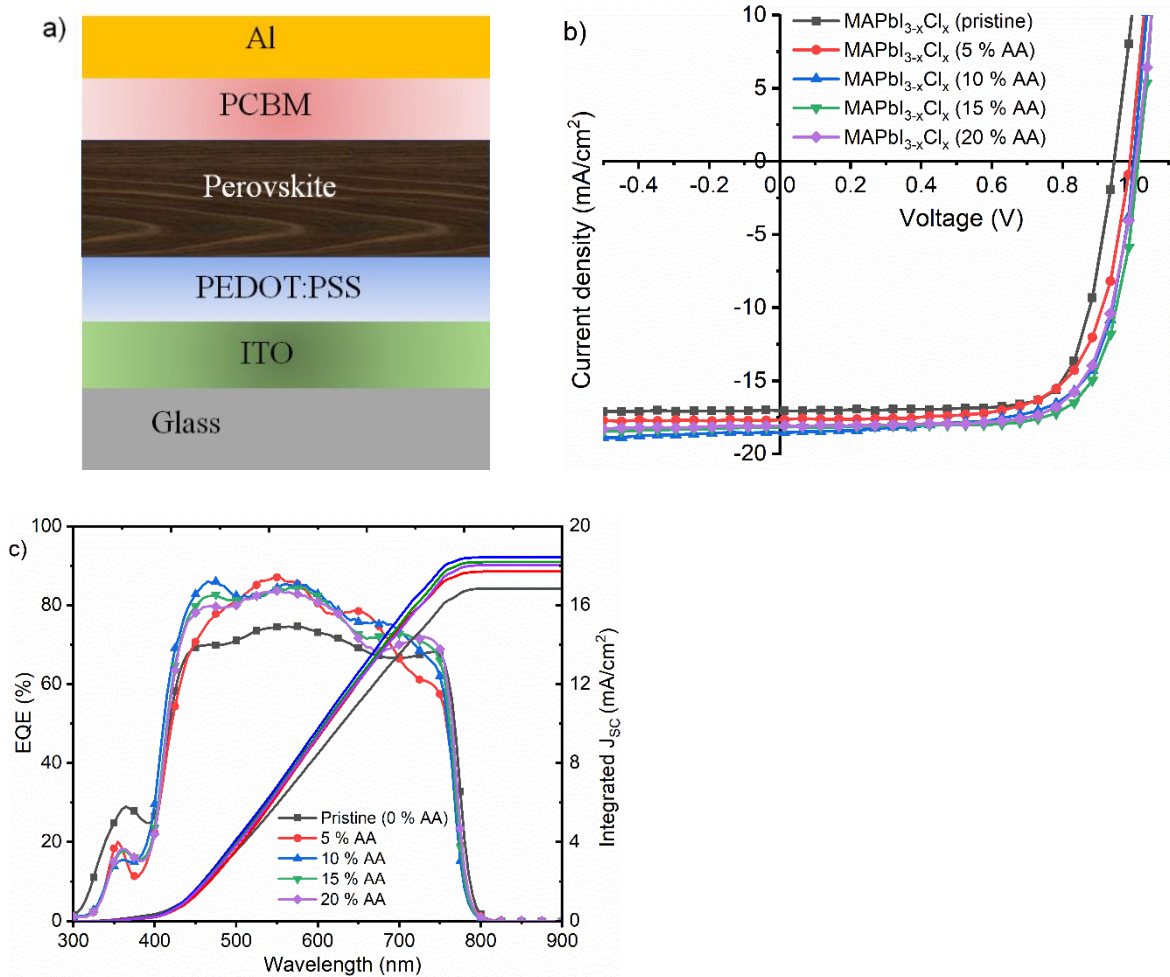


Figure 3.31. a) Schematic structure of p-i-n PSCs. (b) Photocurrent density-voltage (J-V) characteristics, and (c) external quantum efficiency (EQE) and integrated J_{sc} of MAPbI_{3-x}Cl_x PSCs with 0 vol% (pristine), 5, 10, 15 and 20 vol% of AA additive.

To improve the photo-current density of the PSCs, PSCs with two different thickness of PEDOT:PSS HTL were fabricated. Figure 3.32(a) shows the J-V characteristics of MAPbI_{3-x}Cl_x solar cells with 10 vol % AA additive, deposited on a 110 nm and 130 nm thick PEDOT:PSS layers. Devices processed on a thinner PEDOT:PSS show larger J_{sc} , enhanced V_{oc} , and higher PCE.

Figure 3.32(b&c) show the J-V curves of MAPbI_{3-x}Cl_x PSCs with 10 vol % AA and without additive, fabricated on optimized PEDOT:PSS layers measured under 100 mW/cm² light intensity illumination and under dark condition, respectively. The EQE and integrated short-circuit current of the sample and control devices are displayed in Figure 3.32(d). Table 3.8 summarizes the calculated photovoltaic parameters from the J-V data. PSCs with 10 vol % AA exhibit enhanced V_{oc} of about 0.99 V, J_{sc} of ca.18.5 mA/cm² and PCE of about 14 %. Moreover, as can be seen from the semi-log J-V characteristic (Figure 3.32(c)), the sample device displays reduced series resistance of about 14 Ω compared to the control device (24 Ω) in the range of 1 V to 1.5 V which could attribute for the improvement of devices photovoltaic properties.

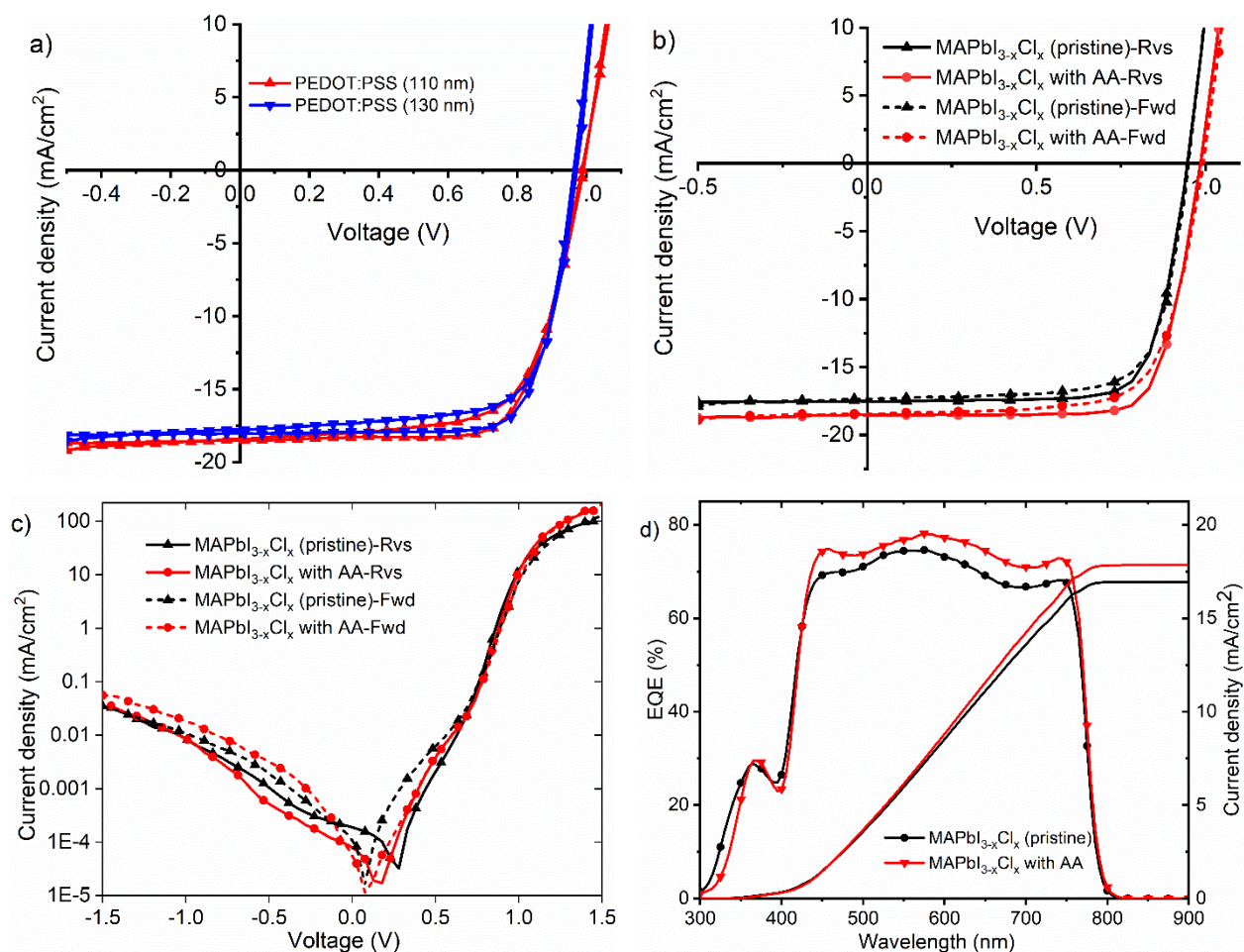


Figure 3.32. a) J-V characteristics of MAPbI_{3-x}Cl_x PSCs with 10 vol % AA additive processed on a 110 nm (red) and a 130 nm (blue) thick PEDOT:PSS HTL. J-V curves of PSCs with 10 vol% AA additive (red, round) and without (black, triangle) for the forward (Fwd, short line) and reverse (Rvs, solid line) scans; b) under 1 sun light (AM1.5 solar spectrum) illumination and c) in the dark (semi-log plot). d) External quantum efficiency and integrated J_{sc} calculated from the EQE data of PSCs with 10 vol% AA additive (red, triangle) and without (black, round).

Cell	Scan	V _{oc} (V)	J _{sc} (mA/cm ²)	FF (%)	PCE (%)
Without AA	Fwd	0.95	17.4	73	12.1
	Rvs	0.95	17.4	75.6	12.5
With AA	Fwd	0.99	18.5	73.1	13.4
	Rvs	0.99	18.5	76.3	14

Table 3.8: Summarized photovoltaic parameters (i.e. V_{oc}, J_{sc}, FF, and PCE) of MAPbI_{3-x}Cl_x PSCs with and without AA additive for the forward (Fwd) and reverse scans (Rvs) under 100 mW/cm² light intensity illumination.

3.3.5. Capacitance-Voltage (C-V) and Mott-Schottky Plot

For a further investigation of the effect of AA additive on the trap density in the photoactive layers, Mott-Schottky and capacitance-voltage (C-V) analysis were applied. Figure 3.33(a) illustrates the capacitance responses of MAPbI_{3-x}Cl_x perovskite solar cells with and without AA additive as a function of frequency (with 0, 0.2, 0.4, 0.5, 0.6 and 0.7 V DC applied voltage) recorded in the dark

at room temperature. The capacitance spectrum shows three distinct regions that are associated with different phenomena that occur in the devices. At high-frequency, the capacitive response decreases which is related to series resistance. The low-frequency capacitance response is associated with a capacitance caused by electrode polarization phenomena (C_s). Between the high and low-frequency, the intermediate, constant plateau capacitive response is related to geometrical capacitance (C_g). This region can contain additional contributions from the depletion layer capacitance (C_{dl}).^[164,165] To study the depletion layer and defect density in the devices, a Mott-Schottky analysis was applied, and the C-V response measurement was made in the constant capacitance plateau region at 10 kHz.

Figure 3.33(b) illustrates the C-V curves and Mott-Schottky plots of perovskite devices with and without AA additive measured at 10 kHz with 10 mV AC voltage in the bias range -0.5 to 1.5 V (forward bias) under dark condition. The defect density of the solar cells is extracted from the slope of a Mott-Schottky plot ($slope = \frac{-2}{\epsilon_r \epsilon_0 q A^2 N_t}$) in the depletion region ($V < V_{bi}$) which is derived from equation 2.17. The calculated trap-density (N_t) for the sample device and control devices is about $1.3 \times 10^{16} \text{ cm}^{-3}$ and $2.2 \times 10^{16} \text{ cm}^{-3}$, respectively. Here, the charge transport layers (HTL and ETL) and electrodes used in both kinds of devices are identical. From this, it can be understood that the changes found in the Mott-Schottky analysis are mainly related to the photoactive perovskite layer. This indicates that the incorporation of AA additive helps to reduce the trap densities in the perovskite film. This is in good agreement with the result obtained from SCLC. Both, SCLC and Mott-Schottky analysis show devices with AA additive exhibit lower trap-state density. Although there is a considerable difference in the magnitude, this could be related to differences in the device structure and measurement principles. The presence of more trap-states in the control film increases non-radiative recombination pathways which decreases the PL intensity and increases the leakage current loss in the device. This is in good agreement with the PL measurement. Analogously, reduced defect-states leading to improved radiative pathways and device characteristics, and consequently larger V_{oc} .

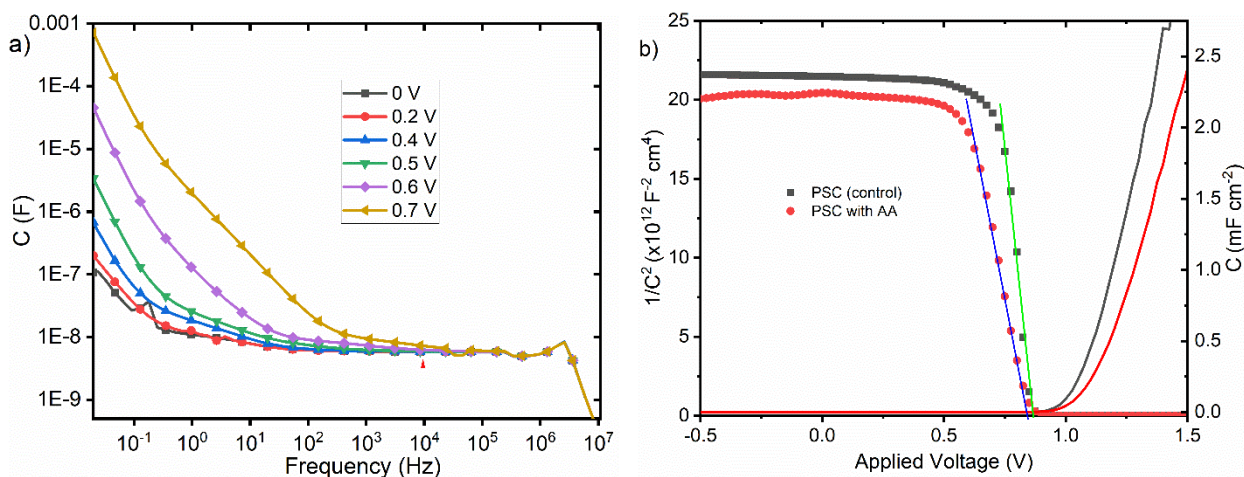


Figure 3.33. (a) Capacitance versus frequency (C-F) responses of MAPbI_{3-x}Cl_x perovskite solar cell at different DC applied voltage (0, 0.2, 0.4, 0.5, 0.6, and 0.7 V) under dark condition. (b) Mott-Schottky plots (C²-V) and capacitance-voltage (C-V) curves of MAPbI_{3-x}Cl_x perovskite solar cells with and without AA additive measured at 10 kHz with 10 mV AC voltage oscillation in forward bias (applied voltage range of -0.5 to 1.5 V) under dark condition.

Furthermore, optimization of the PSCs was achieved by tuning the thickness of the photoactive layer. PSCs with three different thickness of 570 nm, 500 nm, and 400 nm were fabricated by applying different spin-coating speed; 1000 rpm, 1500 rpm and 2000 rpm, respectively. Figure 3.34(a) shows the J-V characteristics of PSCs with different thicknesses. Devices' photovoltaic parameters are summarized in Table 3.9. PSCs deposited at 1500 rpm (500 nm thick perovskite) show the highest V_{OC} of about 1.02 V and J_{SC} of around 18.8 mA/cm² measured for the batch. However, PSC with 570 nm MAPbI_{3-x}Cl_x film shows the highest average FF of about 72 % and PCE of above 13 %.

In section 3.1, it was shown that applying a low temperature processed TiO_x interlayer between PCBM layer and a back metal electrode is important to improve the performance and stability of the PSCs.^[166] Figure 3.34(b) shows the J-V characteristics of PSCs processed with AA additive, and with and without TiO_x interlayer. The device with TiO_x interlayer shows improved rectification in the J-V curve and higher FF.

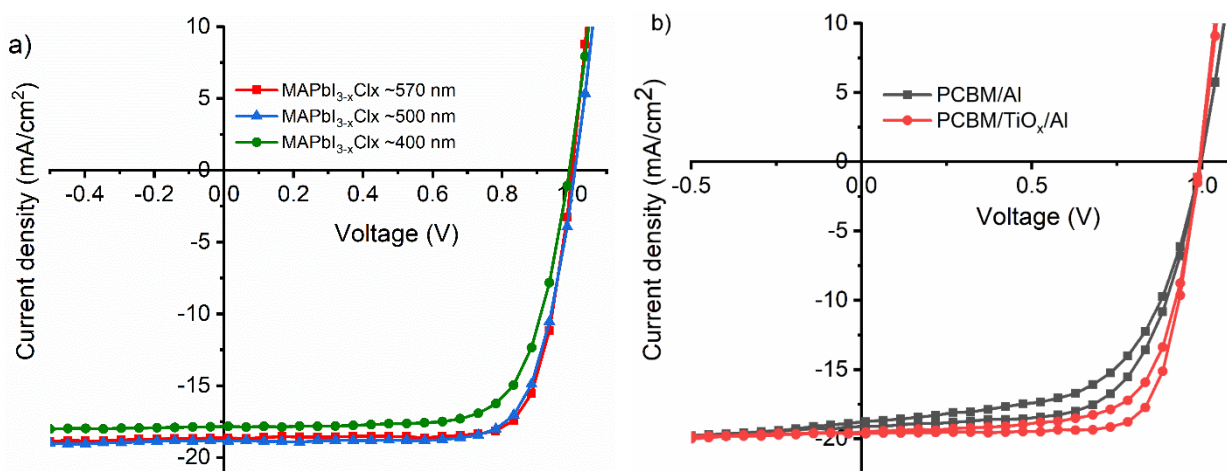


Figure 3.34. J-V characteristics of MAPbI_{3-x}Cl_x PSCs with 10 vol% AA additive; (a) having different photoactive layer thickness, 400 nm (round, green), 500 nm (triangle, blue), and 570 nm (cube, red), (b) with (round, red) and without (square, black) TiO_x interlayer under 1 sun light (AM1.5 solar spectrum) illumination.

Thickness	Scan	V _{oc} (V)	J _{sc} (mA/cm ²)	FF (%)	PCE (%)
~ 400 nm	Rvs	0.99	17.8	71.8	12.7
	Fwd	1	17.8	61.9	11
~ 500 nm	Rvs	1.02	18.8	72	13.8
	Fwd	1.02	18.8	63.5	12.2
~ 570 nm	Rvs	1.01	18.6	77.4	14.5
	Fwd	1	18.6	67.4	12.5

Table 3.9: Summarized photovoltaic parameters (i.e. V_{oc}, J_{sc}, FF and PCE) of PSCs with different thickness, 400 nm, 500 nm and 570 nm, of MAPbI_{3-x}Cl_x films for the forward (Fwd) and reverse scans (Rvs) under 100 mW/cm² light intensity illumination.

The current density-voltage (J-V) characteristic of the best device with [glass/ITO/PEDOT:PSS/MAPbI_{3-x}Cl_x/PCBM/TiO_x/Al] device stacking processed from MAPbI_{3-x}Cl_x perovskite with 10 vol% AA additive is shown in Figure 3.35(a). The device (having 0.16 cm² pixel area) exhibits considerably low hysteresis with a V_{oc} of about 1.02 V, J_{sc} of about 18.7 mA/cm², FF of around 78 %, and PCE of about 14.8 % for the reverse scan, and a V_{oc} of about 1.02 V, J_{sc} of about 18.7 mA/cm², FF of around 74 %, and PCE of about 14.1 % in the forward scan direction under AM1.5 solar spectrum (100 mW/cm² light intensity) illumination (Table 3.10). Figure 3.35(b) shows an EQE spectrum with a maximum of around 80 % resulting in an integrated short-circuit-current density (J_{sc}) of 18.5 mA/cm². As can be seen clearly from the EQE spectrum, there is a photocurrent loss in the range between 300-400 nm. This could be related to the absorption of high energy photons by the HTL (PEDOT:PSS) and the transparent electrode (ITO), decreasing the number of photons reaching the photoactive perovskite layer.

Figure 3.35(c) shows the PCE histogram of 135 PSCs with AA additive and 89 PSCs without AA additive. Gaussian distribution of the PCEs of the prepared solar cells is found. The average PCE of the sample devices (devices with AA additive) and the control devices is about 14 and 12 %, respectively. This indicates that the PCE of devices with AA additive improved by about 17 % compared to control devices

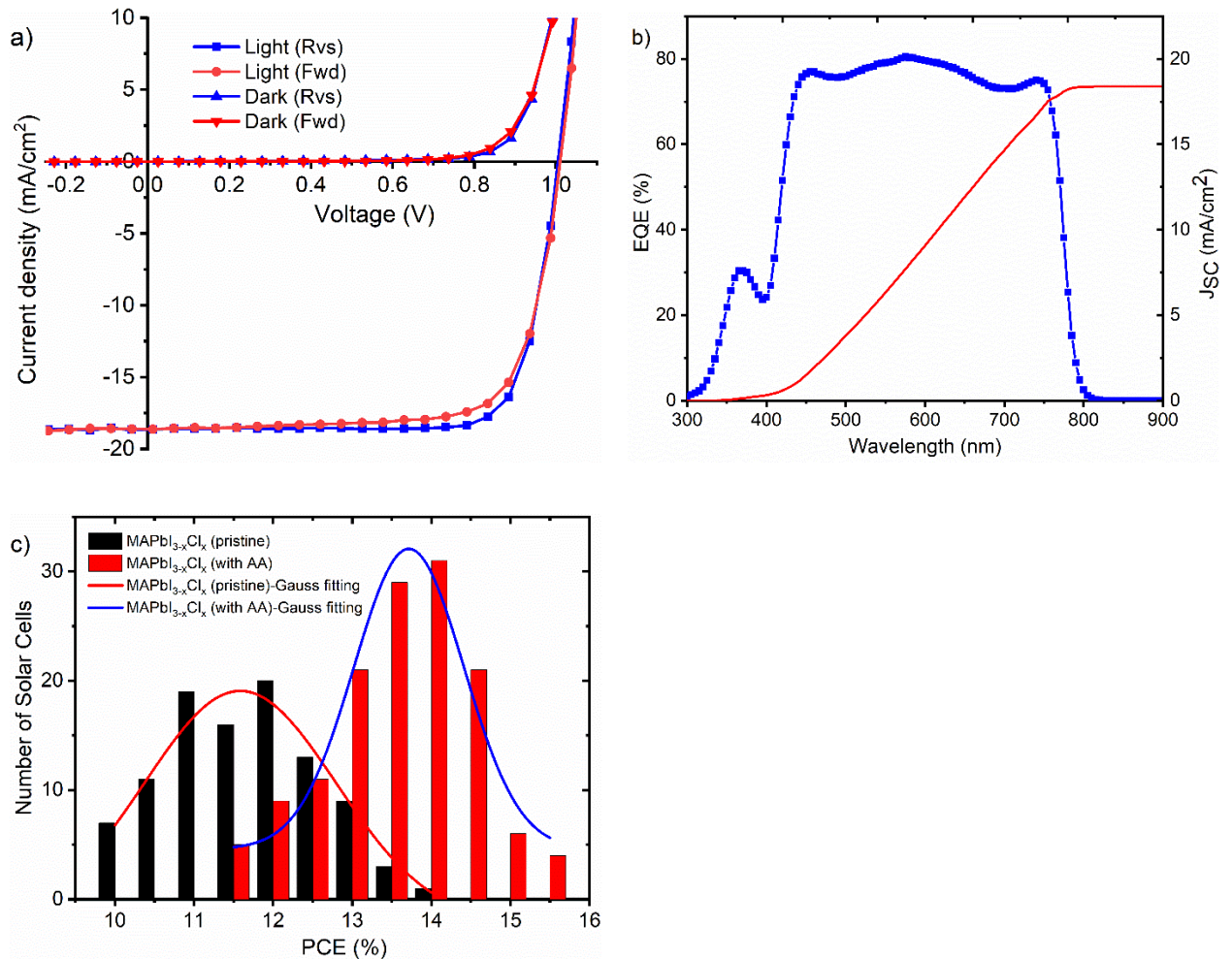


Figure 3.35. a) J-V curves of optimized PSCs with, [glass/ITO/PEDOT:PSS/MAPbI_{3-x}Cl_x/PCBM/TiO_x/Al] device structure under AM1.5 solar spectrum (100 mW/cm² light intensity) illumination. (b) EQE spectrum and the corresponding integrated J_{sc}. (c) PCE histogram of 135 devices with 10 vol% AA additive and 89 control devices under AM1.5 solar spectrum (1 sun light) illumination.

Scan Direction	V _{oc} (V)	J _{sc} (mA/cm ²)	FF (%)	PCE (%)
Rvs-Scan	1.02	18.7	78	14.8
Fwd - Scan	1.02	18.7	74.1	14.1

Table 3.10: Summarized photovoltaic parameters (V_{oc}, J_{sc}, FF and PCE) of an optimized PSCs with, glass/ITO/PEDOT:PSS/MAPbI_{3-x}Cl_x/PCBM/TiO_x/Al device structure processed from MAPbI_{3-x}Cl_x perovskite with 10 vol% AA additive for the forward (Fwd) and revers scans (Rvs) under 100 mW/cm² light intensity illumination.

3.3.6. Stability Study

The steady-state stability of an optimized, encapsulated PSC with AA additive (having device structure: glass/ITO/PEDOT:PSS/MAPbI_{3-x}Cl_x/PCBM/TiO_x/Al) was studied via MPP tracking measurement under AM1.5 solar spectrum illumination in ambient air. The device shows an initial V_{OC} of about 1.03 V, J_{SC} of 18.8 mA/cm², FF of about 76 % and PCE of 14.7 % under 100 mW/cm² light intensity illumination. Figure 3.36(a) shows the steady-state PCE and the current-density at the MPP (J_{max}) of an optimized sample PSC. Figure 3.36(b) shows the voltage at the MPP (V_{max}) and the maximum electrical power output (P_{max}) of the same device. The device shows good stability and maintains about 94 % of its initial photovoltaic properties after continuous operation for 20 hrs.

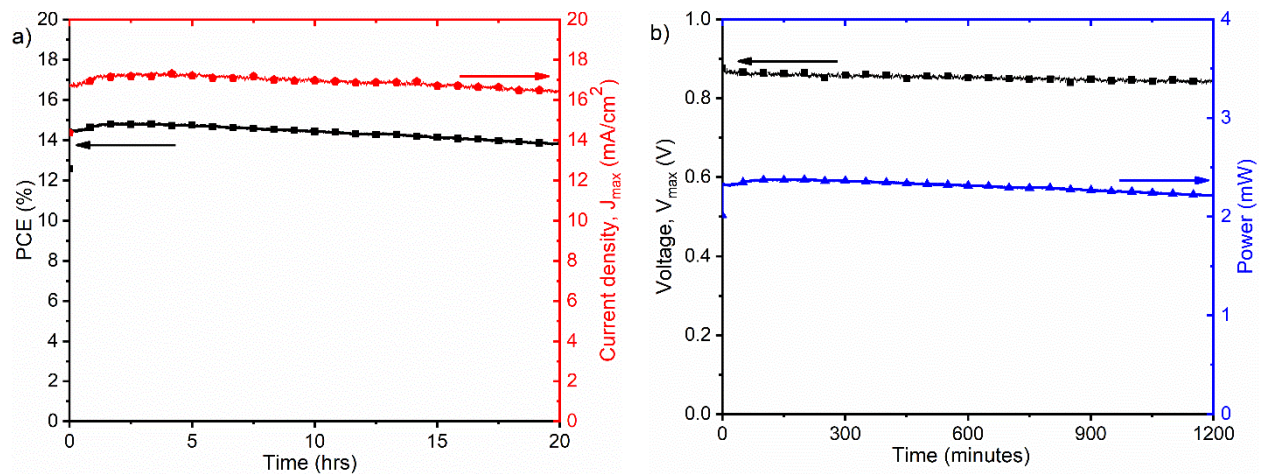


Figure 3.36. Maximum power point (MPP) tracking of encapsulated PSC with AA additive; (a) steady-state power conversion efficiency (PCE) and current density at maximum power (J_{max}), and (b) voltage at maximum power (V_{max}) and maximum power output (P_{max}) under 100 mW/cm² light intensity continuous illumination in ambient air.

The normalized steady-state PCE, current density at MPP (J_{max}), voltage at MPP (V_{max}), and maximum power output (P_{max}) of an encapsulated PSCs with AA additive and without (pristine) are shown in Figure 3.37 (a,b,c&d), respectively. A device with AA additive shows good stability, maintaining about 96 % of its initial current density and above 94 % of initial PCE, while the control device exhibits about 11 % loss of current density and nearly 13 % decrease in PCE after continuous operation for 20 hrs under the same condition. From this, it can be concluded that incorporation of AA additive improves the stability of MAPbI_{3-x}Cl_x PSCs, and is a promising approach to fabricate stable and large area PSCs in ambient air.

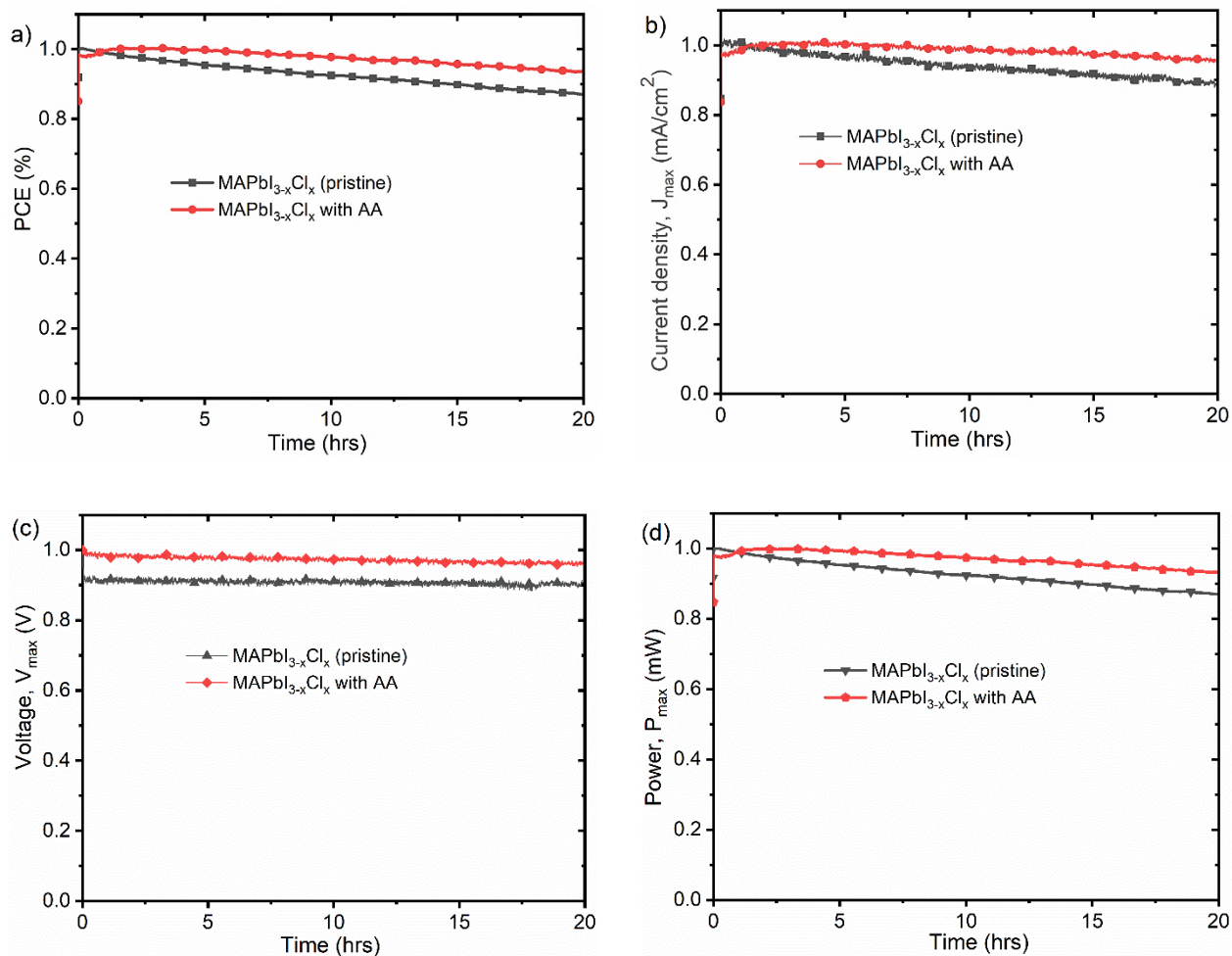


Figure 3.37. Comparative maximum power point (MPP) tracking of encapsulated MAPbI_{3-x}Cl_x PSCs with AA additive (red) and without (black); (a) normalized steady-state power conversion efficiency (PCE), (b) normalized current density at MPP (J_{max}), (c) voltage at MPP (V_{max}), and (d) normalized maximum power (P_{max}) under 100 mW/cm² light intensity continuous illumination in ambient air.

3.3.7. Impedance Spectroscopy

Intensity-modulated photovoltage spectroscopy characteristics of PSCs were measured at open-circuit DC voltage to examine the effect of AA additive on the charge recombination dynamics in perovskite devices. IMVS responses were measured in the frequency range between 1 MHz to 0.02 Hz under LED light ($\lambda = 590$ nm) illumination with light intensity perturbation. Figure 3.38(a&b) show the Nyquist plot and imaginary transfer function (H'') of IMVS characteristics of PSCs with 10 vol% of AA additive and without under 8 mW/cm² LED light ($\lambda = 590$ nm) illumination with 10 % light intensity modulation amplitude. The high-frequency arc in the IMVS response is associated with the recombination resistance.^[133] The IMVS response of MAPbI_{3-x}Cl_x device with AA additive exhibits a wider high-frequency semicircle, implying the sample device exhibits higher recombination resistance compared to the control device. This could be attributed to improved V_{OC} of PSCs with AA additive.

The IMVS spectra of both the sample and control devices were measured under different light intensity (1.6, 3.2, 4.8, 6.4, 8 mW/cm²) LED light ($\lambda = 590$ nm) with identical modulation amplitude. Figure 3.38(c) shows the open-circuit voltage of the devices as a function of light intensity. At a given light intensity, PSC with AA shows higher V_{OC} than the control PSC which is in a good agreement with the J-V observations. Both kinds of devices show nearly identical dependency trends on the light intensity with an ideality factor of about 1.17 and 1.36 for devices with and without AA additive, respectively. Ideality factor of the devices and the intensity of photons are related by

$$\frac{\partial V_{OC}}{\partial \ln I} = \frac{mk_B T}{q}$$

Where m is the ideality factor, k_B is the Boltzmann constant, T is the temperature during the measurements, and q is the elementary charge.

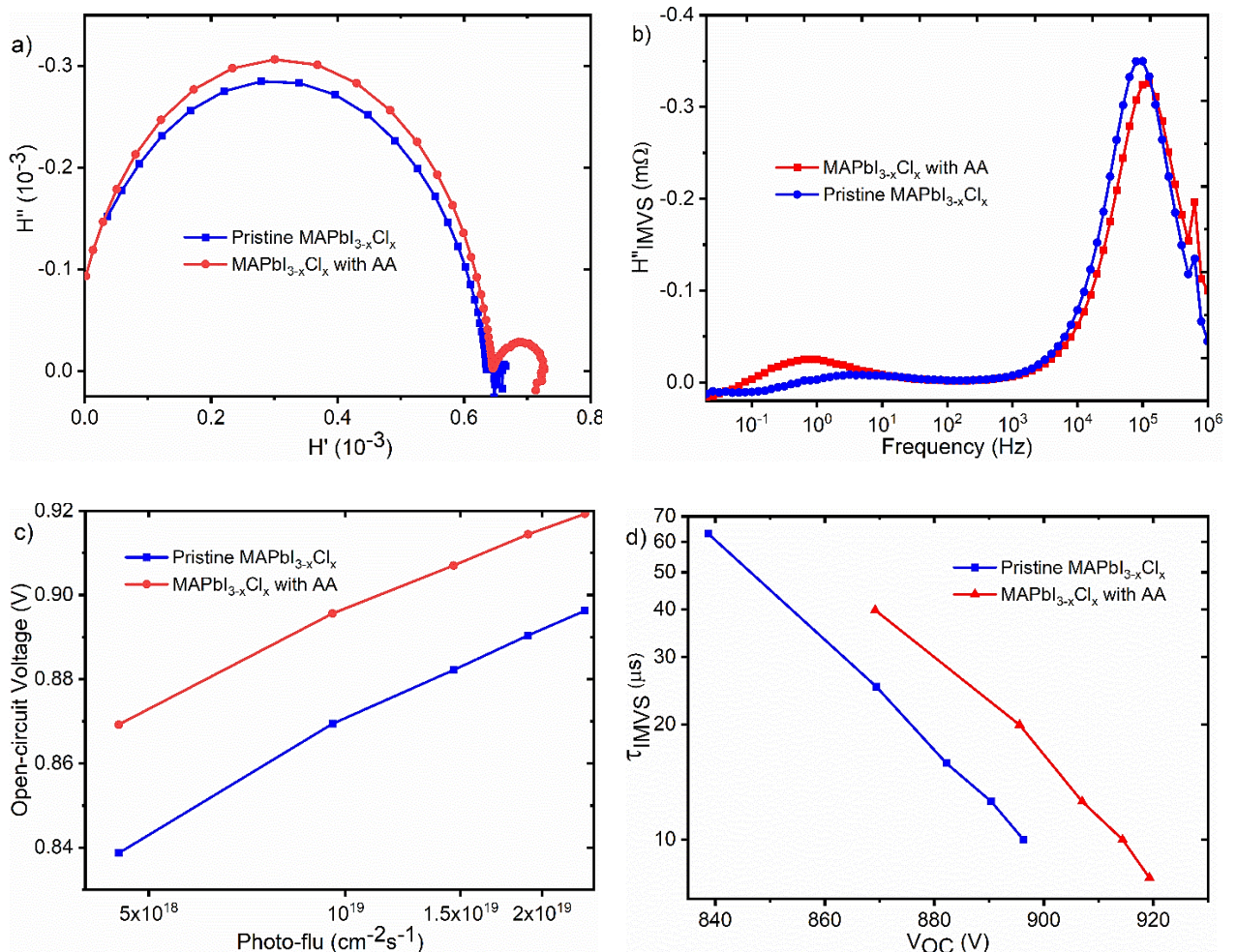


Figure 3.38. Intensity modulated photovoltage spectroscopy (IMVS) characteristics in a) Nyquist plots and b) imaginary transfer function (H'')-versus-frequency plots of PSC with AA additive (*red*) and PSC without AA additive (*blue*), scanned in the frequency range of 1 MHz to 20 mHz with 10 % light intensity modulation amplitude under 8 mW/cm² LED light intensity. (c) Open circuit voltage (V_{OC}) as a function of photon flux (cm⁻² s⁻¹) intensity, and d) the charge carrier recombination time-constant (τ_{IMVS}) as a function of the V_{OC} of the PSC with AA additive (*red*) and PSC without AA additive (*blue*).

Figure 3.38(d) displays the charge carrier recombination time-constants (τ_{IMVS}) as a function of the V_{OC} of the PSCs with (red) and without AA additive (*blue*). The recombination time-constants are extracted from the maximum of the imaginary transfer function (H'') responses of the devices at different LED light intensity scanning. In the IMVS response, the critical frequency, corresponding to the maximum of H'' at high-frequency, is related to critical time by, $f_c = 1/2\pi\tau_c$. At a given V_{OC} , devices with AA additive show longer charge carrier lifetime compared to a device without additive. This indicates the incorporation of AA additive reduces charge carrier recombination and enhances device performance.

Electrochemical impedance spectroscopy characterization was applied to investigate the impact of AA additive on the charge transport dynamics, the charge transfer processes in the bulk and across the interface in $\text{MAPbI}_{3-x}\text{Cl}_x$ devices. The devices were tracked at short-circuit conditions with 10 mV AC voltage in the frequency range between 1 MHz to 0.02 Hz under 8 mW/cm^2 LED irradiation ($\lambda = 590 \text{ nm}$).

Figure 3.39(a&b) show the EIS characteristics at 0 V DC voltage of $\text{MAPbI}_{3-x}\text{Cl}_x$ PSCs with and without AA additive. Both devices show two characteristic semicircles in the Nyquist plots; the high-frequency component is related to the charge transfer resistance (R_2), and the low-frequency one is associated with recombination resistance, ions diffusion, and interface phenomenon.^[133,151]

Figure 3.39(c) shows the equivalent circuit suggested to interpret the EIS responses of the studied devices structure. Table 3.11 summarizes the fitting parameters of the sample and control devices which are calculated from the fitting of devices EIS characteristics using the suggested equivalent-circuit. Devices with AA additive show reduced characteristic charge transfer resistance (R_2). In this investigation, both the sample and control devices have identical device structure and interfacing with the exception that the photoactive layer of the sample device is processed from perovskite solution with AA additive while the control device is without additive. This suggests that the possible deviation observed for the two sets of samples seemingly related to the incorporated AA additive.

The charge transport resistance (R_2) of both kind of devices, obtained from the EIS response fitting, show a strong dependency on the light intensity (Figure 3.39(d)). Devices with AA additive exhibit reduced R_2 at a given photon flux, though both types of devices (sample and control) show analogous dependency on the light intensity. It is obvious that as the charge transport impedance decreases the charge transport process across the device increases and the charge extraction probability increases. This could account for the observed high photocurrent in devices with AA additive compared to the devices without additive.

Perovskite solar cells with AA additive show longer charge carrier recombination lifetimes and reduced transport resistance compared to devices without AA additive. Overall, combining the impedance observation suggests that the addition of AA additive into $\text{MAPbI}_{3-x}\text{Cl}_x$ precursor

solution reduces the charge carrier transport resistance and improves the recombination resistance leading to longer charge carrier lifetimes and improved photovoltaic behaviors.

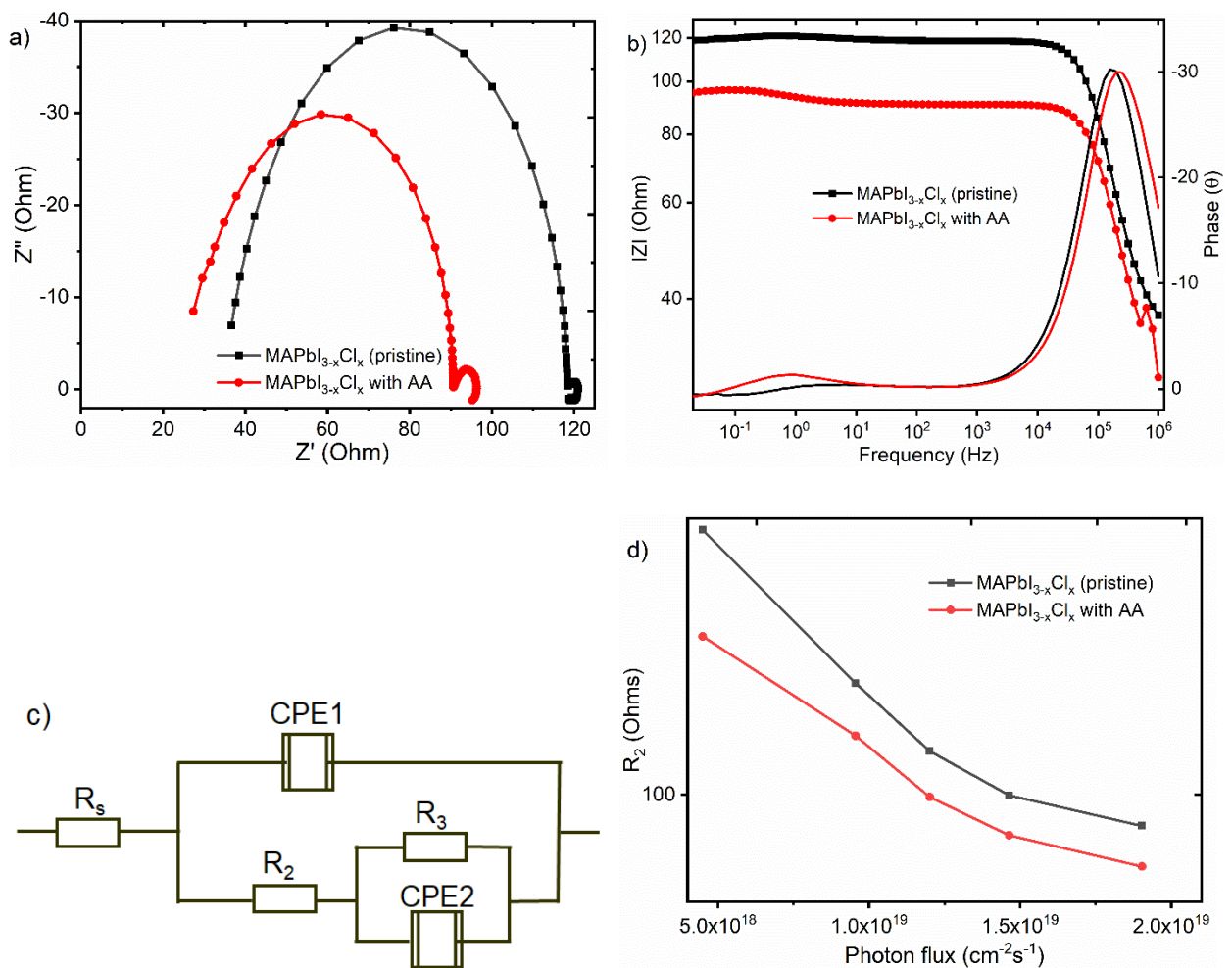


Figure 3.39. (a) Nyquist plots and (b) Bode plots of the electrochemical impedance spectroscopy (EIS) response of a PSC with 10 vol% AA additive (*red*) and PSC without AA additive (*blue*), scanned in the frequency range of 1 MHz to 20 mHz with 0 V DC voltage and 10 mV AC-voltage under 8 mW/cm² LED light intensity. (c) Equivalent circuit model for the solar cells, and d) the charge carrier transfer resistance (R_2) as a function of photon flux (cm⁻²s⁻¹) intensity shine on the cells.

PSCs	R_1 (Ω)	R_2 (Ω)	CPE1		R_3 (Ω)	CPE2	
			T(F)	P		T(F)	P
PVS (pristine)	36.8	81.7	2.66E-8	0.98	2.5	1.75E-2	0.85
PVS with AA	28.1	62.9	2.98E-8	0.97	5.1	3.6E-2	0.93

Table 3.11: Equivalent circuit fitting parameters; series resistance (R_1), transfer resistance (R_2), constant-phase element (CPE1) corresponding to the bulk, resistance related to interface (R_3) and interface related constant-phase element (CPE2), extracted from the fitting of EIS response of PSCs fabricated from MAPbI_{3-x}Cl_x (pristine) and MAPbI_{3-x}Cl_x with AA additives.

3.3.8. Conclusion

In conclusion, this work studies the impact of acetylacetone used as a solvent additive on the performance of $\text{MAPbI}_{3-x}\text{Cl}_x$ perovskite solar cells processed in ambient air. PSCs with AA additive show enhanced photovoltaic properties. The percent composition of AA was optimized by using perovskite precursor solution containing (5, 10, 15 and 20 vol%) of AA additive. The optimized PSC containing 10 vol% of AA additive shows improved average V_{OC} of about 1.02 V, J_{SC} of around 20 mA/cm^2 , Fill factor (FF) of $\sim 76 \%$, and PCE of about 15.5 %. AFM topographic imaging depicts that $\text{MAPbI}_{3-x}\text{Cl}_x$ films with AA additive show improved surface smoothness. EIS and IMVS investigations depict that incorporation of AA additive results in the decrease of charge transport impedance and improved charge recombination impedance, respectively. Moreover, $\text{MAPbI}_{3-x}\text{Cl}_x$ films with AA additive exhibit stronger photoluminescence compared to the pristine $\text{MAPbI}_{3-x}\text{Cl}_x$ films. This appears to confirm that AA solvent additive plays a vital role to reduce the trap-states and recombination conduits across the film, which improves radiative recombination in the perovskite volume. This is in good agreement with SCLC and Mott-Schottky analysis results, in which the trap-states density of devices with AA additive is reduced by about 40 % compared to devices without AA additive. This suggests that AA additive is a highly practical and viable option to fabricate and optimize large-area thin-film perovskite solar cells in an ambient environment.

3.4. Stability Study of Mixed Halide PSCs Using Impedance Spectroscopy

3.4.1. Introduction

Long-term stability is one of the main issues challenging the process of commercializing perovskite solar cells. The instability of PSCs is mainly originating from the degradation of the perovskite semiconductor and the degradation of the interfacial and electrode materials.^[167,168] There are both intrinsic and extrinsic factors affecting the stability, for example, the exposure to UV-light, sensitivity to moisture and oxygen, thermal instability, ion migration or chemical instability.^[169-172] Remarkable improvements have been achieved through compositional modification of the perovskite materials, structural modifications, and interfacial engineering of the perovskite layers.

Applying device encapsulation plays a vital role to protect the solar cell from environmental moisture and oxygen.^[170,173] Interface engineering by applying stable and hydrophobic inorganic and organic HTLs and ETLs, and engineering interfacial contacts can improve the lifetime of PSCs.^[82,174,175,176] A-cation compositional tuning has proven to be a vital approach to enhance the mechanical robustness, thermal and moisture stability of the perovskite materials.^[19,169,170,173,177] The issue of ion migration is another factor affecting the device long-term stability which can be overcome by using appropriate contacts, and modifying the morphology and composition of the perovskite by A-site alkali doping and replacement, multi-dimensional (2D/3D) perovskites engineering, and applying molecular additives.^[63,170]

A detailed understanding of the changes in the materials and the device structure, and processes that occur in the devices under real world conditions is required to alleviate the issues of stability. Many efforts have been devoted in this aspect in the past few years. W. Tress et al. (2019)^[171] studied the effect of light intensity and temperature on the PCE and long-term stability of PSCs under simulated ambient condition and found reversible and irreversible degradation during the course of one year operation. However, little is known about what happens inside the device structure causing the degradation upon continuous operation. To get insight about these issues, it is necessary to apply different characterization techniques which provide direct or indirect information about the degradation processes in the bulk, electrodes and interfaces of the devices.

In this work, impedance techniques were applied to study the electrical and ionic dynamics in the absorber layer and interfaces of PSCs before and after continuous operation under solar illumination. The goal of this investigation was to follow the changes in the EIS response of the PSCs and to identify the processes and mechanisms responsible for the reduction of device performance over time. PSCs with device structure [ITO/PEDOT:PSS/PVS/PCBM/TiO_x/Al] were fabricated following the procedure given in the experimental section. Devices were encapsulated and MPP-tracking measurements were conducted for 48 hrs under AM1.5 (1 sun) illumination in

ambient air. In parallel, the device J-V characteristic and electrochemical impedance responses were measured before and immediately after the MPP tracking.

Figure 3.40(a) shows the schematic diagram of the investigated devices structure. The photocurrent density-voltage (J-V) characteristics (Figure 3.40(b)) illustrate an increase in the device hysteresis and a decrease of the V_{OC} and FF, leading to an overall decrease of the PCE after continuous operation for 48 hrs. Figure 3.40(c) shows MPP-tracking characteristics, the PCE and current density at MPP (J_{max}) of an encapsulated PSC under 1 sun light illumination. The evolution of maximum power and the corresponding voltage at MPP (V_{max}) are shown Figure 3.40(d). The device degraded by about 8 % from its initial performance after continuous operation for 48 hrs.

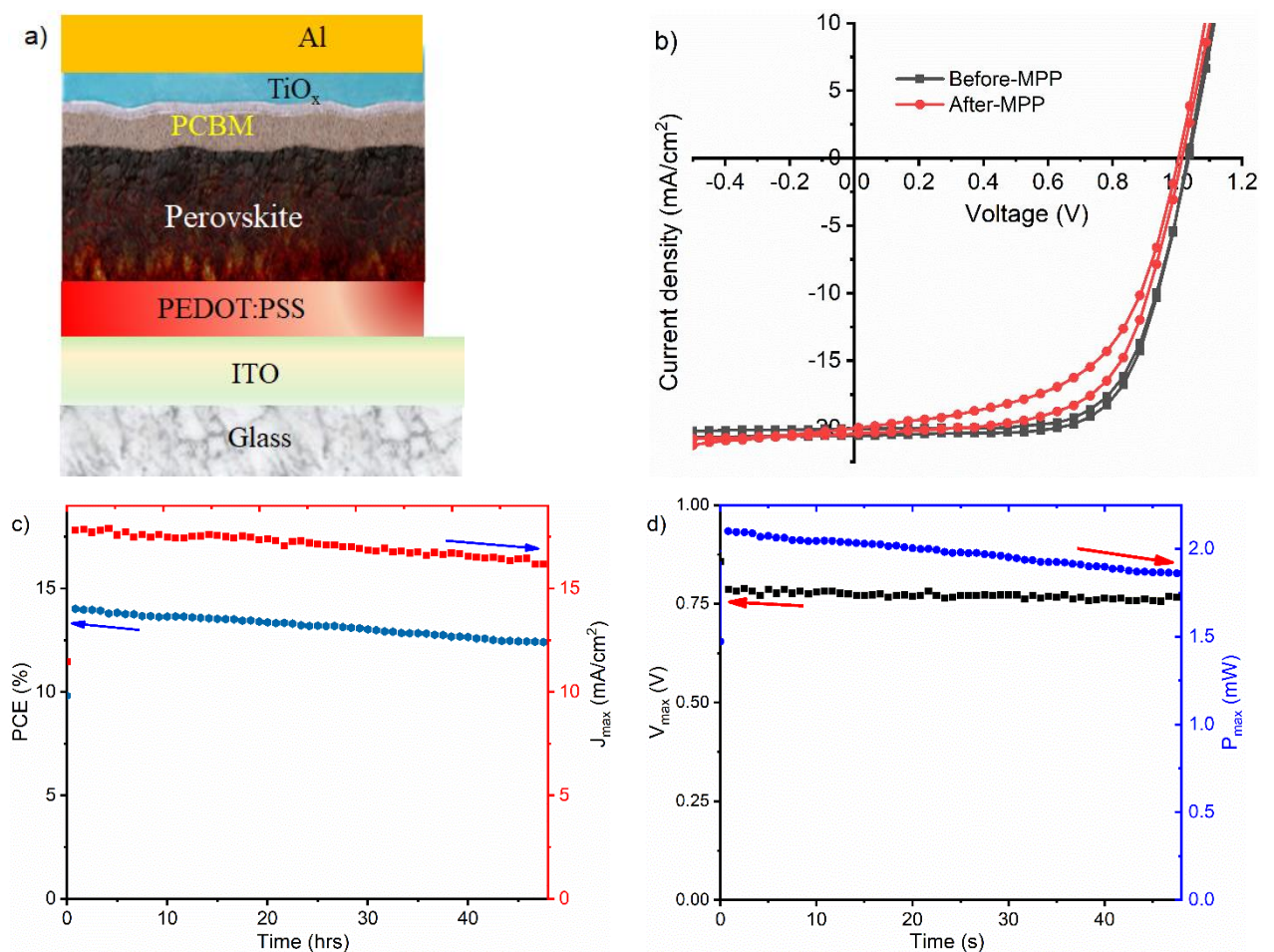


Figure 3.40. a) Schematic diagram of the perovskite solar cell used. (b) Photoinduced current density-voltage (J-V) characteristics of PSC before and after MPP-tracking under AM1.5 solar spectrum ($100\text{ mW}/\text{cm}^2$ light intensity) illumination. Maximum power point (MPP) tracking of an encapsulated PSC; (c) steady-state power conversion efficiency (PCE, hexagon) and current density at maximum power (J_{max} , cube), and (d) voltage at maximum power (V_{max} , cube) and maximum power (P_{max} , sphere) under $100\text{ mW}/\text{cm}^2$ light intensity continuous illumination in ambient air.

3.4.2. Electrochemical Impedance Spectroscopy (EIS) Results

The electrochemical impedance spectroscopy response of the device was measured before and after the MPP-tracking experiment. Figure 3.41(a&b) shows the corresponding Nyquist and Bode plots. The EIS was recorded at short-circuit conditions with 10 mV AC-voltage under LED light ($\lambda = 590$ nm) illumination in the frequency range between 1 MHz to 0.02 Hz. The Nyquist plots (Figure 3.41 (a)) show two semi-circles in two distinct frequency regions which represent different processes in the device. The high-frequency semi-circle is associated with the charge transport resistance, and the low-frequency response is related to the recombination resistance, and interfacial phenomena.^[151,178,179,180] As mention above, an equivalent circuit model with two time-constants was suggested according to Garcia-Belmonte et al.^[126] to interpret the EIS responses in Figure 3.41(c). Table 3.12 summarizes the fitting parameters of each circuit element for the corresponding EIS response.

An analysis of the EIS response under 8 mW/cm² light illumination shows that after 48 hrs of continuous operation the transport resistance (R_2) increases, while the interface related resistance (R_3) shows negligible change. The constant phase element-1 (CPE1), related to the dielectric properties of the perovskite material, decreases by about 4 nF. The low-frequency CPE2, which is associated with an interfacial phenomena increases by about 60 mF.

The electronic properties of the devices before and after a continuous operation are extracted from the EIS characteristics, under different LED light intensities. Figure 3.42(a) illustrates that the bulk capacitor (CPE1) decreases after the MPP-tracking, and the differences are becoming larger at lower light intensities (1.6 mW/cm²). Figure 3.42(b) shows the charge transport resistance (R_2) increases after MPP-tracking. This indicates charge carriers are trapped and the charge transport process is hindered. As mentioned above, the interfacial charge impedance (R_3) does not show significant change (Figure 3.42(c)). This could indicate that the impedance across the charge transporting layers does not change within the testing time domain. However, the interfacial capacitive element (CPE2) increases after MPP-tracking (see Figure 3.42(d)). This indicates that the accumulation of electronic and ionic charge carriers at the interface increases,^[126,127,181] suggesting ionic migration to the interfaces leaving behind defect-states in the bulk of the perovskite. This could explain the increase of J-V hysteresis observed.

Figure 3.43 illustrates the time-constants extracted from the EIS responses of the device under different light intensities (1.6, 3.2, 4.8, 6.4, 8 mW/cm²) of LED light. The charge transport resistance time-constant (τ_{tr}) represent the dielectric relaxation time. It is calculated from the maximum peak of angular frequency of the imaginary impedance in the high-frequency region using the relation $\tau_{tr} = 1/2\pi f$. It can also be derived from the product of R_2 and CPE1.^[178] The time-constant extracted from low-frequency region (τ_{inter}) appears to increase after MPP-tracking (Figure 3.43(b)). This indicates that the average characteristic life-time of the charge carriers

generated in the device is elongated, which could be associated with the accumulation of ions at the interfaces. This further suggests the accumulation of ion at the interface, could imply that the defect concentration in the bulk increases.

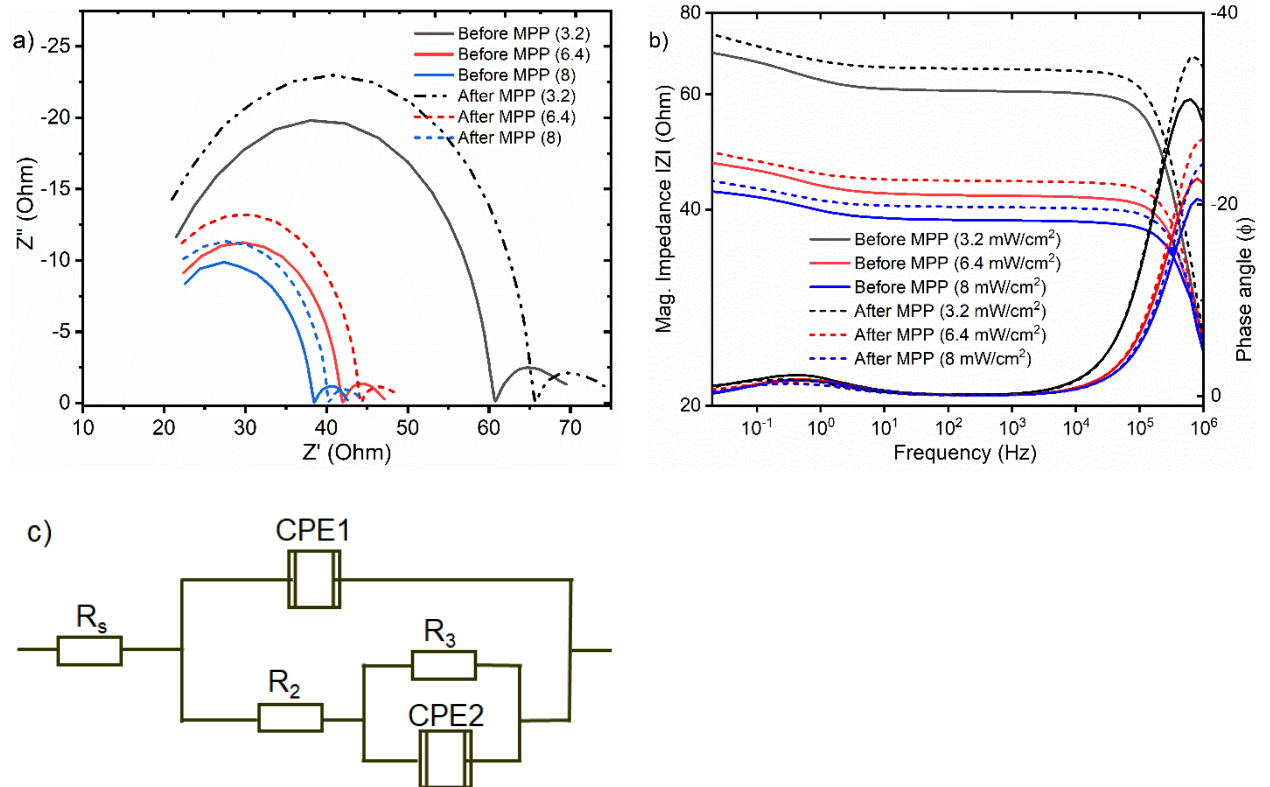


Figure 3.41. (a) Nyquist and (b) Bode plots of EIS characteristics of the device before (solid lines) and after (broken lines) the MPP-tracking was made, measured at short-circuit conditions with 10 mV AC voltage and under different light intensities (3.2, 6.4 and 8 mW/cm²) LED light ($\lambda = 590$ nm) illumination. (c) Equivalent circuit model for the solar cell.

Cells	R_s (Ohm)	R_2 (Ohm)	R_3 (Ohm)	CPE1		CPE2	
				TDE (F)	Phase	TDE (F)	Phase
Before MPP tracking	17.5	20.9	4.3	2.66E-08	0.96	0.12	0.66
After MPP tracking	16.5	23.7	4.6	2.26E-08	0.98	0.18	0.55

Table 3.12: Equivalent circuit fitting parameters; series resistance (R_1), transfer resistance (R_2), constant-phase element (CPE1) corresponding to the bulk, resistance related to interface (R_3) and interface related constant-phase element (CPE2), extracted from the fitting of the EIS response of PSC before and after MPP-tracking measured under 8 mW/cm² LED light ($\lambda = 590$ nm) illumination.

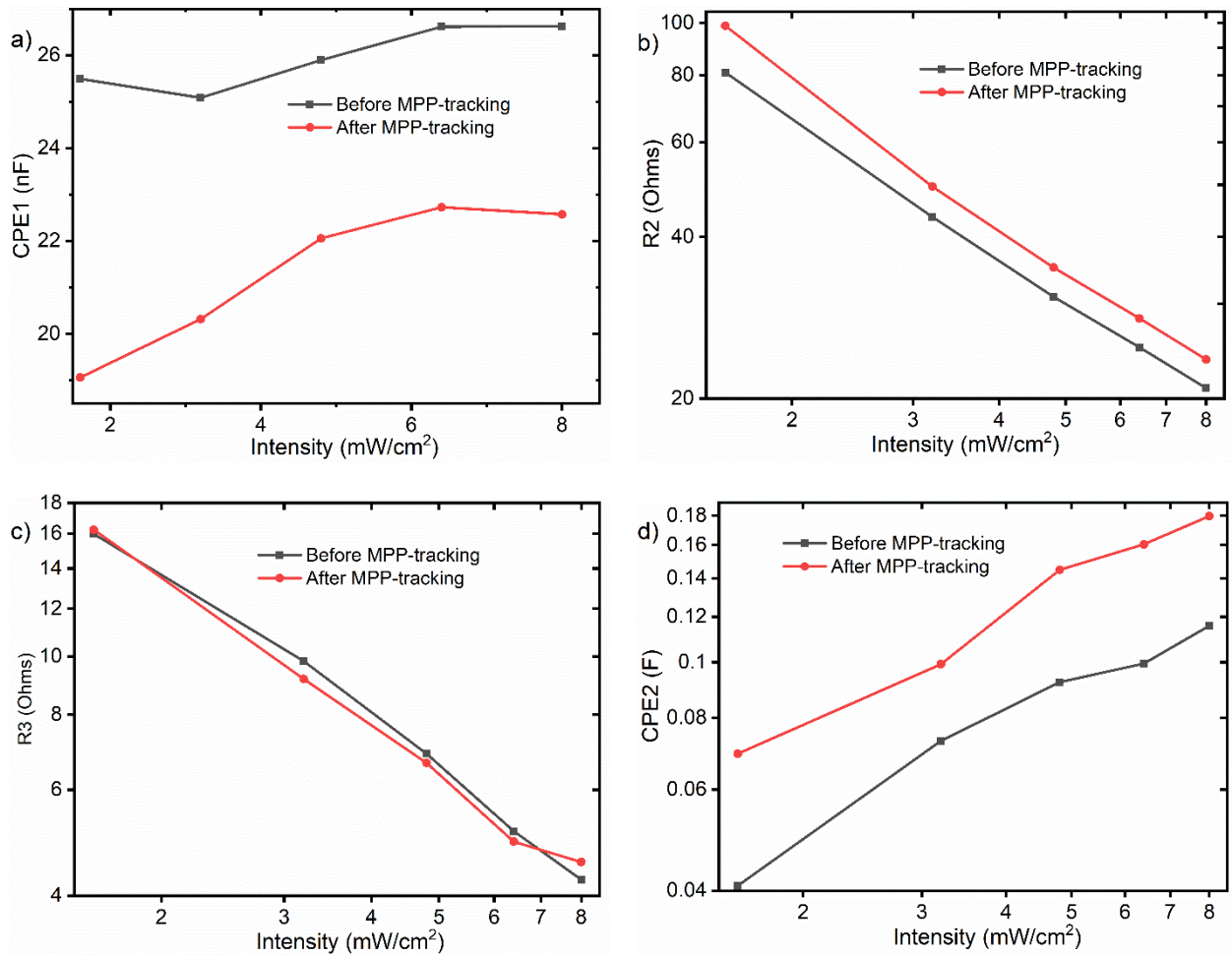


Figure 3.42. Comparative electronic properties of the PSCs before(cube) and after (sphere) MPP-tracking: (a) bulk-constant phase element (CPE1), (b) charge transport resistance (R_2), (c) interfacial recombination resistance (R_3) and (d) interfacial constant phase element (CPE2) under illumination of 1.6, 3.2, 4.8, 6.4, 8 mW/cm² LED light ($\lambda = 590$ nm) intensities.

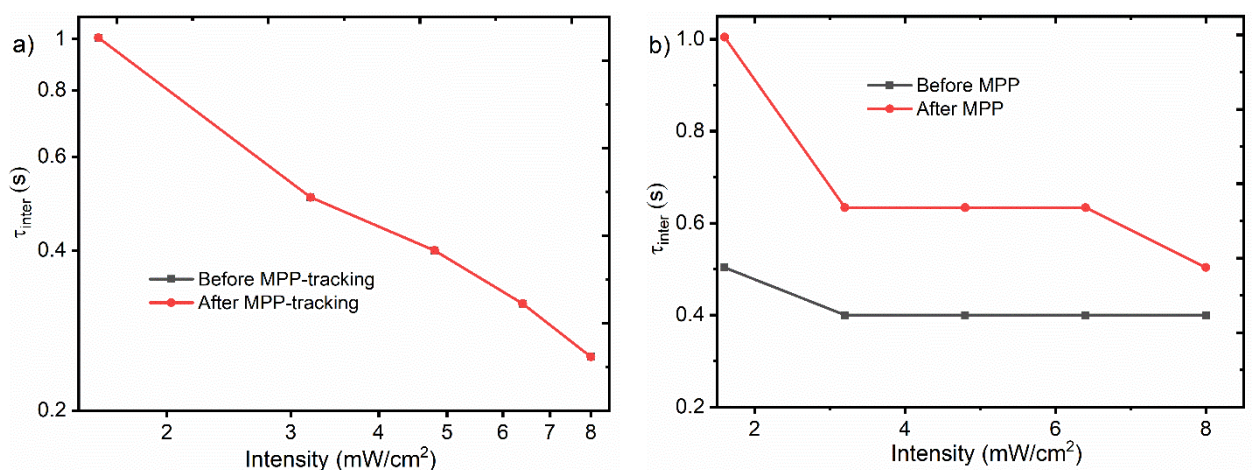


Figure 3.43. The time constants extracted from (a) high-frequency region and (d) low-frequency region of EIS responses of the device under different intensities (1.6, 3.2, 4.8, 6.4, 8 mW/cm²) LED light ($\lambda = 590$ nm) illumination with 10 mV AC-volt oscillation.

3.4.3. Intensity Modulated Photovoltage Spectroscopy (IMVS) Results

The intensity-modulated photovoltage spectroscopy response of the same device studied above was recorded to get a detail understanding of the charge recombination dynamics in the solar cell. The IMVS response was measured at open-circuit conditions, under LED light illumination with 10 % light intensity perturbation in the frequency range between 1 MHz to 0.02 Hz. Figure 3.44 shows the IMVS characteristics of the device measured before and after the MPP-tracking. Figure 3.44(a) shows Nyquist plots and Figure 3.44(b) shows the imaginary transfer function (H'') versus frequency recorded at different light intensities. The continuous operation led to a decrease in the diameter of the high-frequency semicircles, suggesting a reduction of the charge recombination resistance of the solar cell.

To extract the recombination time-constants, the IMVS response of the device was measured under different LED light ($\lambda = 590$ nm) intensities (1.6, 3.2, 4.8, 6.4, 8 mW/cm²) with identical modulation amplitude and in the same frequency region. Figure 3.44(c) depicts the V_{OC} of the device as a function of light intensities before (cube) and after (sphere) the MPP-tracking. The V_{OC} of the device decreases upon continuous operation. The charge carrier recombination time-constants (τ_{IMVS}) of the PSC before (cube) and after (sphere) the MPP-tracking as a function of the V_{OC} are extracted in the high-frequency region (Figure 3.44(d)). In IMVS, the critical frequency corresponding to the maximum of H'' at high-frequency, is related to critical time by $f_c = 1/2\pi\tau_c$.^[178]

The device recombination time-constants in the high-frequency region show similar trends on the light intensity before and after the continuous operation with an ideality factor of about 1.57 and 1.62, respectively. But at a given intensity, the device V_{OC} decreases after operation which is in a good agreement with the reduced recombination resistance illustrated in the Nyquist curve (Figure 3.44(a)). Consequently, at a given V_{OC} the high-frequency τ_{rec} shows reduction of the recombination time-constant. But the interface related and slow process time-constants (low-frequency response time-constants) show negligible change after continuous operation. This suggests that the reduction of the device photovoltaic properties upon continuous operation is mainly related to the changes in the bulk of the photoactive perovskite film which is in good agreement with the EIS response.

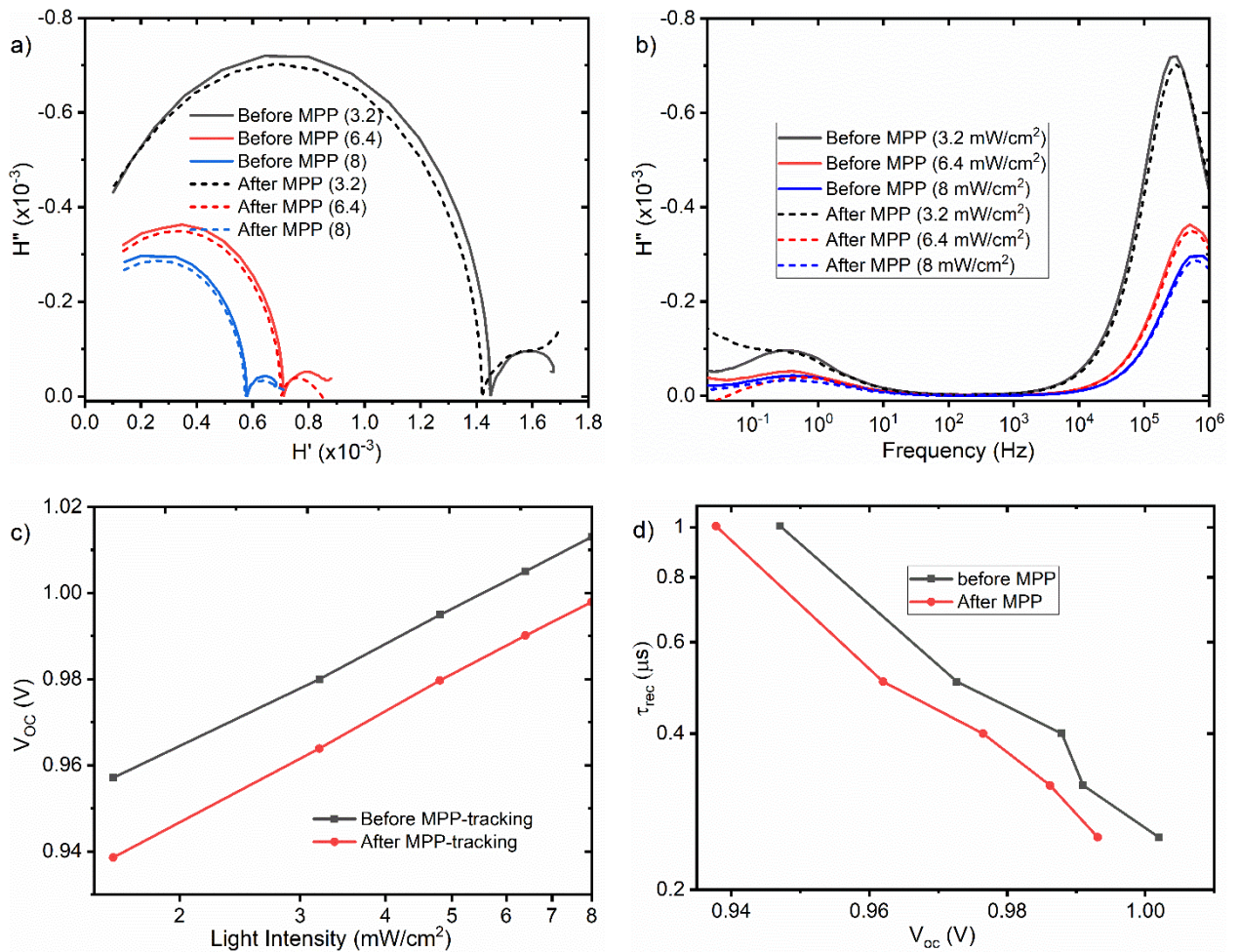


Figure 3.44. (a) Nyquist and (b) imaginary transfer function (H'') of IMVS characteristics of the device before (solid lines) and after (dash lines) the MPP-tracking was made, under 3.2, 6.4 and 8 mW/cm² LED light ($\lambda = 590$ nm) illumination with 10 % light intensity modulation amplitude. (c) Open-circuit voltage (V_{oc}), and (d) the time-constants of IMVS response of the device before (cube) and after (sphere) under different intensities (1.6, 3.2, 4.8, 6.4, 8 mW/cm²) LED light ($\lambda = 590$ nm) illumination with identical modulation amplitude extracted from high-frequency region.

Furthermore, another MAPbI_{3-x}Cl_x perovskite solar cells, with 2,9-dimethyl-4,7-diphenyl-1,10-phenanthroline (BCP) ETL interlayer instead of a TiO_x interlayer were studied, with the objective to compare the device behavior under continuous operation. The same approach applied for devices with TiO_x interlayer was applied for devices with BCP interlayer. Figure 3.45(a) shows the J-V characteristics of MAPbI_{3-x}Cl_x PSC with BCP interlayer before and after MPP-tracking, and Figure 3.45(b) displays the steady-state PCE and current density at MPP (J_{max}). The device photovoltaic parameters decrease with time under continuous operation. Figure 3.45(c&d) shows the Nyquist and Bode plots of MAPbI_{3-x}Cl_x PSC with BCP interlayer before and after MPP-tracking, respectively. Interestingly, analogous to devices with TiO_x interlayer, the EIS response of the device shows that the charge transport impedance increases under MPP-tracking. While the low-frequency, slowly moving species, and interfacial processes impedance show negligible changes.

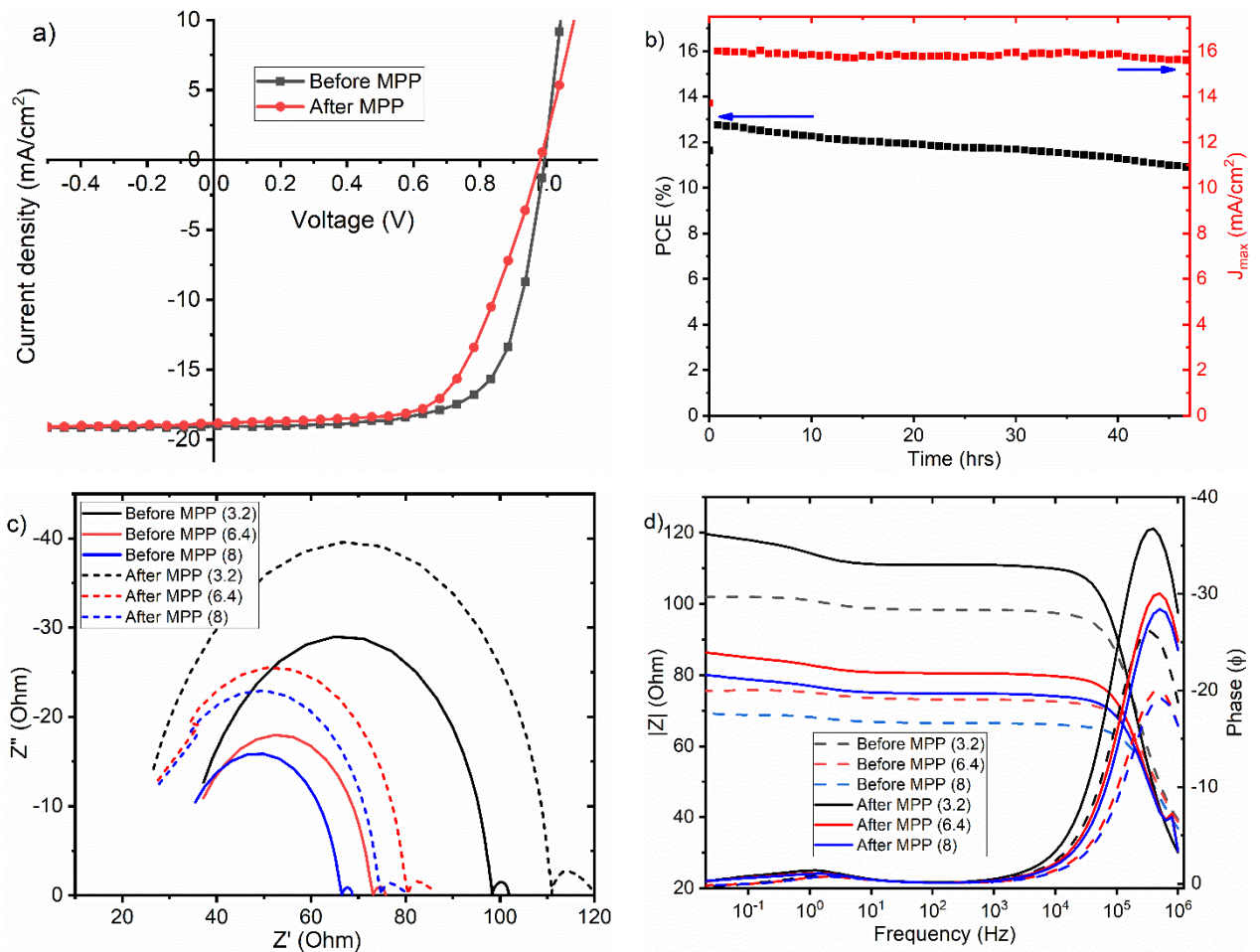


Figure 3.45. (a) J-V curves of PSC before (solid lines) and after (dash lines) MPP-tracking under AM1.5 solar spectrum (100 mW/cm² light intensity) illumination. (b) Maximum power point (MPP) tracking of an encapsulated PSC; steady-state power conversion efficiency (PCE) and current density at MPP (J_{max}). EIS characteristics; (a) Nyquist and (b) Bode plots of a PSC with BCP ETL buffer layer measured under 3.2, 6.4, and 8 mW/cm² LED light ($\lambda = 590$ nm) intensities at short-circuit with 10 mV AC voltage in the frequency range between 1 MHz to 0.02 Hz.

Figure 3.46(a&b) show Nyquist plots and imaginary transfer function (H'') versus frequency plots of PSC with BCP interlayer recorded at different light intensities. The IMVS characteristics depict an identical trend with the response observed for PSC with TiO_x interlayer. The diameter of high-frequency semicircles reduced after MPP tracking, confirming that the charge recombination resistance of the device decreases. Figure 3.47(a&b) show the V_{oc} and the recombination resistance time-constant extracted from the high-frequency arc of IMVS characteristics at different light intensities. Both, the V_{oc} and the recombination impedance time-constant significantly decreases after MPP-tracking which are analogous to devices response with a TiO_x interlayer. This further suggests that the changes in the device photovoltaic properties upon continuous operation are mainly related to ion migration in the photoactive perovskite film.

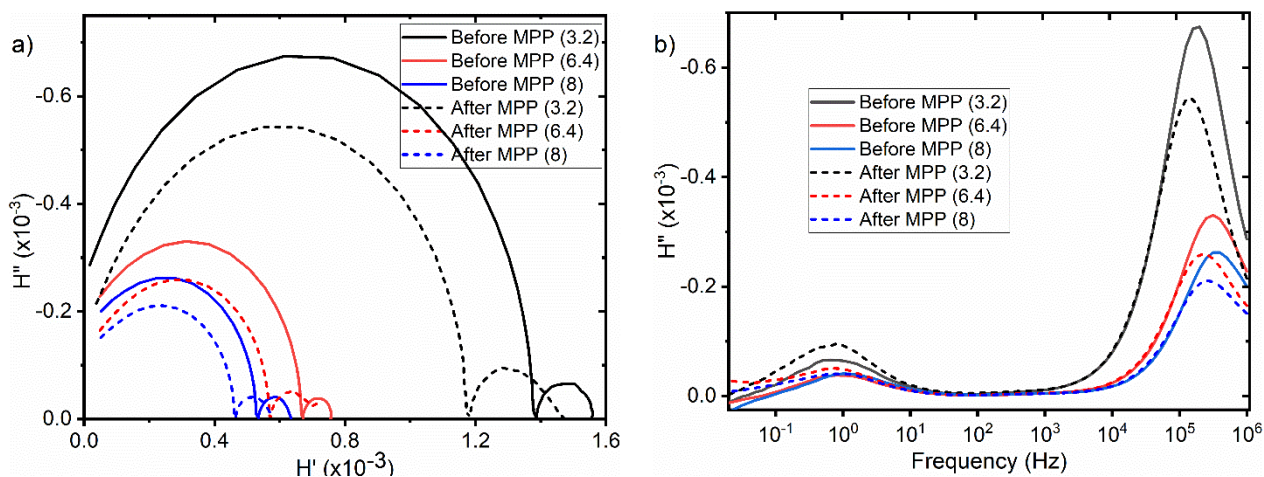


Figure 3.46. (a) Nyquist plot, and (b) imaginary transfer function (H'') of IMVS characteristics of a PSC with BCP buffer layer between the ETL and Al electrode measured before (solid lines) and after (dash lines) a continuous operation under 3.2, 6.4, and 8 mW/cm^2 LED light ($\lambda = 590 \text{ nm}$) intensities in the frequency range between 1 MHz to 0.02 Hz.

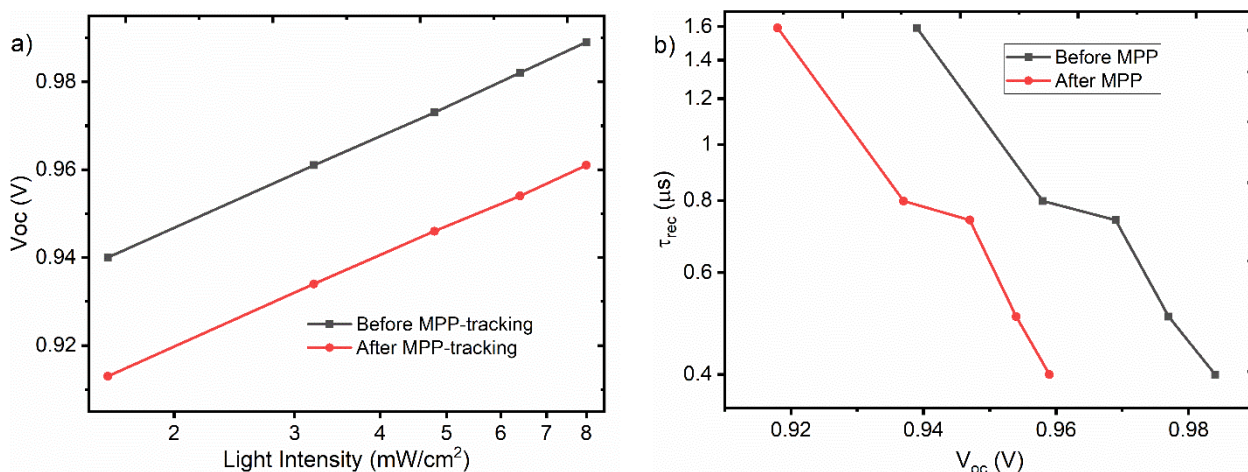


Figure 3.47. (a) The characteristics V_{oc} , and (b) charge carrier recombination time-constants of a PSC with BCP interlayer under different LED light ($\lambda = 590 \text{ nm}$) intensities (1.6, 3.2, 4.8, 6.4, 8 mW/cm^2) illumination with 10 % light modulation amplitude.

3.4.4. Capacitance-Voltage (C-V) Results

The electrochemical impedance spectroscopy characteristics of the PSC shows that the interface related capacitive behavior increases under continuous operation, suggesting the increase of ion accumulation at the interfaces upon continuous operation. This could be explained by ion migration from the bulk to interfaces leaving behind defect-states in the bulk. To confirm the change of defect-state densities in the photoactive layer, Mott-Schottky analysis was applied using the capacitance-voltage (C-V) response of the device. Figure 3.48(a&b) show the J-V characteristics and Mott-Schottky plots of a $\text{MAPbI}_{3-x}\text{Cl}_x$ PSC measured at 10 kHz with 10 mV AC voltage in the forward bias range (-0.5 to 1.2 V) under dark condition, before and after MPP-tracking.

As described in section 2.4.7 of this thesis, the trap density of the device is extracted from the slope of a Mott-Schottky plot (*i.e.* $slope = \frac{-2}{\epsilon_r \epsilon_0 q A^2 N_t}$) in the depletion region ($V < V_{bi}$). The trap density (N_t) of the device increases from $\sim 2.56 \times 10^{15} \text{ cm}^{-3}$ to around $2.76 \times 10^{15} \text{ cm}^{-3}$ after 90 hrs under continuous operation, which was further increased to $2.95 \times 10^{15} \text{ cm}^{-3}$ after 290 hrs continuous operation. This indicates that the trap-state density increases with time under MPP-tracking, leading to a decrease in device performance. This is in good agreement with the increase of charge transport impedance and the interface capacitance which suggests the ion migration to the interface leaving trap-states in the perovskite film. From this, it can be understood that the changes in the Mott-Schottky plots and device performance under continuous operation is predominantly related to the changes in the photoactive perovskite layer as well as the ion accumulation at the interfaces.

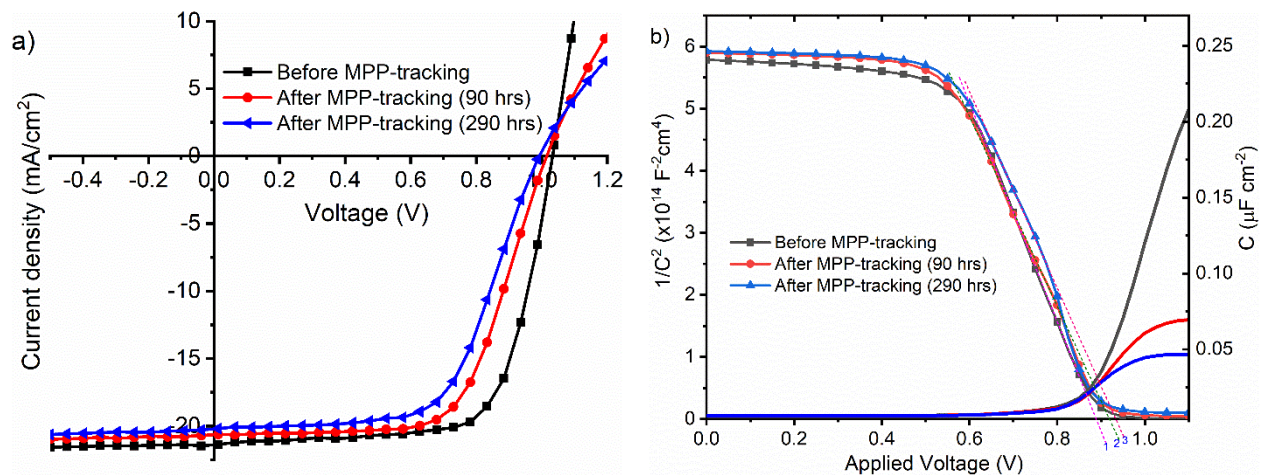


Figure 3.48. (a) J-V characteristics of MAPbI_{3-x}Cl_x PSC under AM1.5 solar spectrum (1 sun) illumination before (cube) and after 90 hrs (sphere) and 290 hrs (triangle) MPP-tracking. (b) C-V characteristics and Mott-Schottky plots (C^2 vs V) of the same PSC with active area of 0.15 cm^2 , before and after MPP-tracking measured at 10 kHz with 10 mV AC voltage oscillation in forward bias (applied voltage range of -0.5 to 1.2 V) under dark condition.

3.4.5. Conclusion

In summary, the electrical and ionic dynamics across the bulk and interfaces of the PSCs were characterized before and after continuous MPP tracking, using electrochemical impedance. EIS results show that the device charge transport resistance and interfacial capacitance associated with charge accumulation are increased after continuous operation. This suggests ion migration from the photoactive perovskite layer to the charge selective layers leaving defects in the bulk. Unlike the bulk charge transport resistance characteristics, resistance-associated interfacial layers show negligible changes after MPP-tracking. Furthermore, IMVS characteristics illustrate a decrease in charge recombination resistance, indicating formation of more trap-states in the device under continuous operation. The increase in the interfacial charge carrier recombination time-constant under continuous operation indicates that the average charge carrier life-time of the charges generated in the device is elongated. This could be associated with the accumulation of

electronic and ionic charge carriers at the interfaces. Moreover, C-V characteristics and Mott-Schottky analysis of the solar cell shows a consecutive increase of the trap-state density by about 8 % after 90 hrs and 15 % after 290 hrs of continuous operation. This could be due to ionic migration to the interfaces leaving behind defect-states in the bulk of the perovskite under continuous operation. From this study, it can be concluded that the decay of the device performance upon continuous operation is mainly related to changes in the bulk of the photoactive perovskite film and ion accumulation at the interfaces.

The study suggests that to reduce ion migration induced device decaying, “better” perovskite semiconductors and smarter interface engineering are required. “Better” perovskite semiconductors could be achieved through a careful understanding of the physics and chemistry of the materials, and precise compositional and process designing.

Summary and Outlook

In this dissertation, the role of different interface materials and solvent engineering on the physics and chemistry of interfaces in perovskite devices was investigated. Much efforts have been made to understand the effect of surfaces and interfaces on charge carrier dynamics, and outstanding improvements have been achieved on the performance and stability of the device. NiO_x and PEDOT:PSS have been applied and optimized as a HTLs for mixed-cation mixed-halide perovskite and mixed halide perovskite recipe. The device open-circuit voltage and overall performance show a strong dependence on the type of HTL employed. In this research, it has been verified that inverted mixed-cation mixed-halide perovskite devices based NiO_x HTL show higher photo-conversion efficiency compared to devices with PEDOT:PSS HTL when the same photoactive material is applied. This can be explained by the chemistry of the interface between the perovskite layer and the HTL (NiO_x or PEDOT:PSS) and degree of energy level alignment at the HTL/perovskite interface.

Studying the effect of ETLs interfaces on the performance and stability of devices was another motive of this dissertation. In this work, an effective and facile method to modify the ETL/Metal interface was shown using a thin layer of low temperature processed titanium oxide (TiO_x) or polyphosphazene derivatives (PPz), as a buffer layer between PCBM and back-contact metal. PSCs with TiO_x interlayer display reduced series resistance compared to the control device, which results in improved rectification of the J-V curves, and improved FF, PCE, and stability. PL and EL responses indicate the improvement of the charge carrier extraction process for devices with TiO_x compared to the control devices which is in a good agreement to EIS and IMVS measurements, showing higher charge transfer impedance for control devices and higher recombination impedance for devices with TiO_x interlayer.

A similar approach reveals that the application of PPz buffer layer between PCBM and back-contact metal is an ideal approach to reduced the J-V hysteresis, and improve photovoltaic properties and photostability. Furthermore, the merit of applying PPz5 interlayer extends to the possibility of using different metals (such as aluminum, gold, copper, and silver) as top contact in the prepared PCSs. Overall, this investigation proves that employing a PPz or TiO_x ETL interlayer is a promising approach to tackle the issue of interfacing and plays a dual role to improve device stability and overall performance.

Furthermore, a solvent engineering technique using acetylacetone (AA) additive was applied to modify the bulk and surface chemistry of the MAPbI_{3-x}Cl_x perovskite films and hence the charge carrier dynamics in PSCs. I show that AA additive induces morphological modifications and improvement in optoelectronic properties of MAPbI_{3-x}Cl_x perovskite. PSC with optimized AA additive (10 vol %) shows an improved V_{OC} of about 1.02 V, J_{SC} of around 20 mA/cm², Fill factor (FF) of ~76 %, and PCE of about 15.5 %. Moreover, PL, SCLC, and Mott-Schottky plot analysis

appear to confirm that AA solvent additive plays a vital role to reduce the trap-states and recombination channels across the film, which boosts the enhancement of radiative recombination pathways. This approach has proven to be a highly practical and viable option to fabricate and optimize large area, thin film $\text{MAPbI}_{3-x}\text{Cl}_x$ perovskite solar cells in an ambient environment with a high degree of reproducibility.

The issue of device degradation is one of the main obstacles challenging the progress of perovskite solar cells (PSCs). In this PhD thesis, I applied electrochemical impedance measurements in combination with MPP-tracking to characterize PSCs, aiming to gain insight on the bulk and interface charge carrier dynamics under operation. The EIS data show that the device charge transport resistance and interfacial capacitance increases, and the recombination impedance decreases after continuous operation. This suggests that the decaying of the device performance upon continuous operation is mainly related to the changes in the bulk of the photoactive perovskite film due to ion migration to the interfaces.

In this endeavor, I achieved the planned objectives, and show the choice of surfaces and interfaces in perovskite devices strongly affects the charge carrier extraction process, and hence the device efficiency and stability. I am able to fabricate stable PSCs with PCE of above 17 % by employing NiO_x as a HTL, mixed-cation mixed-halide perovskite as a photoactive layer, PCBM as ETL, and TiO_x or PPz5 as a buffer layer. Moreover, developing a reliable and reproducible device fabrication protocol was another principal objective. In this aspect, I found a highly practical approach to fabricate $\text{MAPbI}_{3-x}\text{Cl}_x$ perovskite devices, in an ambient air, by utilizing an acetylacetone solvent additive in the perovskite precursor solution and TiO_x as an ETL interlayer. This approach enables excellent reproducibility to fabricate a PSC typically having PCE of about 15 % with good stability.

The way forward, to achieve highly stable perovskite devices with enhanced performance, one needs to consider the combined effect of careful interface designing, compositional engineering, and processing conditions of the devices. Besides, proper designing of the perovskite band-gap to be able to absorb into the near infra-red region can help to improve the photocurrent. This could be achieved by careful incorporation of narrow band-gap perovskites, whispering gallery mode micro-resonators, and plasmonic light harvesters. Combining the best composition with the appropriate stoichiometric ratios and additives is essential to enhance the chemical and physical properties of the perovskite. Moreover, the application of careful ionic designing at the interfaces modifies the surface chemistry and electronic polarity, which could help to reduce the issue of ion migration.

References

- 1 Global Energy Statistical Yearbook 2019,
<https://yearbook.enerdata.net/total-energy/world-consumption-statistics.html>, accessed on 29/10/2019.
- 2 K. Yu. J. Chen, *Nanoscale Res. Lett.* 2009, 4, 1-10.
- 3 The U. S. Energy Information Administration (EIA), *Today in energy, EIA projects global energy-related CO2 emissions will increase through 2050*,
<https://www.eia.gov/todayinenergy/detail.php?id=41493>, accessed on 11/14/2019.
- 4 M.A. Halim, *Nanomaterials*, 2013, 3, 22-47.
- 5 L. Etgar, *Materials*, 2013, 6, 445-459.
- 6 M. Kouhnavard, S. Ikeda, N.A. Ludin, N.B.A. Khairudin, B.V. Ghaffari, M.A. Mat-Teridi, M.A. Ibrahim, S. Sepeai, K. Sopian, *Renew. Sustainable Energy Rev.* 2014, 37, 397-407.
- 7 U.S. Department of Energy, Energy Efficiency and Renewable Energy, *The History of solar-Department of Energy*, pp1-12.
- 8 J. Perlin, *From Space to Earth: The Story of Solar Electricity*. aatec publication, Ann Arbor, Michigan 48107, United States: 734.995.1470, 1999, pp1-56.
- 9 J. Tsao, N. Lewis, G. Crabtree, *Solar FAQs, Working Draft Version*, 2006, pp1-24.
- 10 M. Grätzel, *Nature*, 2001, 414, 338-344.
- 11 P.V. Kamat, *J. Phys. Chem. C* 2008, 112, 18737-18753.
- 12 H. J. Snaith, *J. Phys. Chem. Lett.* 2013, 4, 3623-3630.
- 13 J. H. Heo, M. H. Lee, M. H. Jang, S. H. Im, *J. Mater. Chem. A* 2016, 4, 17636-17642.
- 14 M. Saliba, T. Matsui, J.-Y. Seo, K. Domanski, J.-P. Correa-Baena, M. K. Nazeeruddin, S. M. Zakeeruddin, W. Tress, A. Abate, A. Hagfeldt, M. Grätzel, *Energy Environ. Sci.* 2016, 9, 1989-1997.
- 15 D. B. Mitzi, *Chem. Mater.* 1996, 8, 791-800.
- 16 Z. Yi, N. H. Ladi, X. Shai, H. Li, Y. Shen, M. Wang, *Nanoscale Adv.* 2019, 1, 1276-1289.
- 17 T.-B. Song, Q. Chen, H. Zhou, C. Jiang, H.-H. Wang, Y. M. Yang, Y. Liu, J. You, Y. Yang, *J. Mater. Chem. A*, 2015, 3, 9032-9050.
- 18 J.-H. Im, I.-H. Jang, N. Pellet, M. Grätzel, N.-G. Park, *Nat. Nanotechnol.* 2014, 9, 927-932.
- 19 D. P. McMeekin, G. Sadoughi, W. Rehman, G. E. Eperon, M. Saliba, M. T. Hörantner, A. Haghighirad, N. Sakai, L. Korte, B. Rech, M. B. Johnston, L. M. Herz, H. J. Snaith, *Science*, 2016, 351, 151-155.
- 20 J. Berry, T. Buonassisi, D. A. Egger, G. Hodes, L. Kronik, Y.-L. Loo, I. Lubomirsky, S. R. Marder, Y. Mastai, J. S. Miller, D. B. Mitzi, Y. Paz, A. M. Rappe, I. Riess, B. Rybtchinski, O. Stafsudd, V. Stevanovic, M. F. Toney, D. Zitoun, A. Kahn, D. Ginley, D. Cahen, *Adv. Mater.* 2015, 27, 5102-5112.

- 21 L. Zhao, N. Rolston, K. M. Lee, X. Zhao, M. A. Reyes-Martinez, N. L. Tran, Y.-W. Yeh, N. Yao, G. D. Scholes, Y.-L. Loo, A. Selloni, R. H. Dauskardt, B. P. Rand, *Adv. Funct. Mater.* 2018, 28, 1802060(1-9).
- 22 D. Yang, R. Yang, K. Wang, C. Wu, X. Zhu, J. Feng, X. Ren, G. Fang, S. Priya, S. (F.) Liu, *Nat. Commun.* 2018, 9, 1-11.
- 23 S. Chen, K. Roh, J. Lee, W. K. Chong, Y. Lu, N. Mathews, T. C. Sum, A. Nurmikko, *ACS Nano*, 2016, 10, 3959-3967.
- 24 N. Alwadai, M. A. Haque, S. Mitra, T. Flemban, Y. Pak, T. Wu, I. Roqan, *ACS Appl. Mater. Interfaces*, 2017, 9, 37832-37838.
- 25 Z. Xiao, R. A. Kerner, L. Zhao, N. L. Tran, K. M. Lee, T.-W. Koh, G. D. Scholes, B. P. Rand, *Nat. Photonics*, 2017, 11, 108-115.
- 26 A. Kojima, K. Teshima, Y. Shirai, T. Miyasaka, *J. Am. Chem. Soc.* 2009, 131, 6050-6051.
- 27 J.-H. Im, C.-R. Lee, J.-W. Lee, S.-W. Park, N.-G. Park, *Nanoscale*, 2011, 3, 4088-4093.
- 28 H.-S. Kim, C.-R. Lee, J.-H. Im, K.-B. Lee, T. Moehl, A. Marchioro, S.-J. Moon, R. Humphry-Baker, J.-H. Yum, J. E. Moser, M. Grätzel, N.-G. Park, *Sci. Rep.* 2012, 2, 1-7.
- 29 M. Lee, J. Teuscher, T. Miyasaka, T. N. Murakami, H. J. Snaith, *Science*, 2012, 338, 643-647.
- 30 A. Pockett, G. Eperon, N. Sakai, H. Snaith, L. M. Peter, P. J. Cameron, *Phys. Chem. Chem. Phys.* 2017, 19, 5959-5970.
- 31 S. D. Stranks, G. E. Eperon, G. Grancini, C. Menelaou, M. J. P. Alcocer, T. Leijtens, L. M. Herz, A. Petrozza, H. J. Snaith, *Science*, 2013, 342, 341-344.
- 32 M. Saliba, T. Matsui, J.-Y. Seo, K. Domanski, J.-P. Correa-Baena, M. K. Nazeeruddin, S. M. Zakeeruddin, A. Kojima, K. Teshima, Y. Shirai, T. Miyasaka, *J. Am. Chem. Soc.* 2009, 131, 6050-6051.
- 33 G. E. Eperon, V. M. Burlakov, P. Docampo, A. Goriely, H. J. Snaith, *Adv. Funct. Mater.* 2014, 24, 151-157.
- 34 G. Hodes, D. Cahen, *Acc. Chem. Res.* 2012, 45, 705-713.
- 35 M. Saliba, T. Matsui, K. Domanski, J.-Y. Seo, A. Ummadisingu, S. M. Zakeeruddin, J.-P. Correa-Baena, W. R. Tress, A. Abate, A. Hagfeldt, M. Grätzel, *Science*, 2016, 354, 206-209.
- 36 M. Saliba, K. W. Tan, H. Sai, D. T. Moore, T. Scott, W. Zhang, L. A. Estroff, U. Wiesner, H. J. Snaith, *J. Phys. Chem. C* 2014, 118, 17171-17177.
- 37 M. A. Halim, *Nanomaterials*, 2013, 3, 22-47.
- 38 NREL. Best Research Cell Efficiencies Chart, <https://www.nrel.gov/pv/cell-efficiency.html>, accessed on 29/8/2019.
- 39 W. S. Yang, B.-W. Park, E. H. Jung, N. J. Jeon, Y. C. Kim, D. Uk Lee, S. S. Shin, J. Seo, E. K. Kim, J. H. Noh, S. Il Seok, *Science*, 2017, 356, 1376-1379.
- 40 H. Chen, F. I. Ye, W. Tang, J. He, M. Yin, Y. Wang, F. Xie, E. Bi, X. Yang, M. Grätzel, L. Han, *Nature*, 2017, 550, 92-95.

-
- 41 V. M. Goldschmidt, *Naturwissenschaften*, 1926, 14, 477-485.
- 42 L. Yang, A. T. Barrows, D. G. Lidzey, T. Wang, *Rep. Prog. Phys.* 2016, 79, 026501(1-26).
- 43 J. Albero, A. M. Asiri, H. Garcia, *J. Mater. Chem. A* 2016, 4, 4353-4364.
- 44 L. K. Ono, Y. Qi, *J. Phys. D: Appl. Phys.* 2018, 51, 093001(1-27).
- 45 J. H. Noh, S. H. Im, J. H. Heo, T. N. Mandal, S. I. Seok, *Nano Lett.* 2013, 13, 1764-1769.
- 46 G. Xing, N. Mathews, S. Sun, S. S. Lim, Y. M. Lam, M. Gratzel, S. Mhaisalkar and T. C. Sum, *Science*, 2013, 342, 344-347.
- 47 E. T. Hoke, D. J. Slotcavage, E. R. Dohner, A. R. Bowring, H. I. Karunadasa, M. D. McGehee, *Chem. Sci.* 2015, 6, 613-617.
- 48 S. Colella, E. Mosconi, P. Fedeli, A. Listorti, F. Gazza, F. Orlandi, P. Ferro, T. Besagni, A. Rizzo, G. Calestani, G. Gigli, F. De Angelis and R. Mosca, *Chem. Mater.* 2013, 25, 4613-4618.
- 49 J. H. Heo, S. H. Im, *Nanoscale*, 2016,8, 2554-2560.
- 50 J. A. Christians, P. A. Miranda Herrera, P. V. Kamat, *J. Am. Chem. Soc.* 2015, 137, 4, 1530-1538.
- 51 B. Hailegnaw, S. Kirmayer, E. Edri, G. Hodes, D. Cahen, *J. Phys. Chem. Lett.* 6, 9, 1543-1547.
- 52 B. R. Vincent, K. N. Robertson, T. S. Cameron, O. Knop, *Can. J. Chem.* 1987, 65, 1042-1046.
- 53 J.-W. Lee, D.-J. Seol, A.-N. Cho, N.-G. Park, *Adv. Mater.* 2014, 26, 4991-4998.
- 54 G. E. Eperon, C. E. Beck, H. J. Snaith, *Mater. Horiz.* 2016, 3, 63-71.
- 55 A. Binek, F. C. Hanusch, P. Docampo, T. Bein, *J. Phys. Chem. Lett.* 2015, 6, 1249-1253.
- 56 J.-P. Correa-Baena, A. Abate, M. Saliba, W. Tress, T. J. Jacobsson, M. Grätzel, A. Hagfeldt, *Energy Environ. Sci.* 2017,10, 710-727.
- 57 Z. Li, M. Yang, J.-S. Park, S.-H. Wei, J. J. Berry, K. Zhu, *Chem. Mater.* 2016, 28, 284-292.
- 58 F. Hao, C. C. Stoumpos, D. H. Cao, R. P. H. Chang, M. G. Kanatzidis, *Nat. photonics* 2014, 8, 489-494.
- 59 N. K. Noel, S. D. Stranks, A. Abate, C. Wehrenfennig, S. Guarnera, A.-A. Haghighirad, A. Sadhanala, G. E. Eperon, S. K. Pathak, M. B. Johnston, A. Petrozza, L. M. Herz, H. J. Snaith, *Energy Environ. Sci.* 2014, 7, 3061-3068.
- 60 Y. Ogomi, A. Morita, S. Tsukamoto, *J. Phys. Chem. Lett.* 2014, 5, 1004-1011.
- 61 F. Hao, C. C. Stoumpos, R. P. H. Chang, M. G. Kanatzidis, *J. Am. Chem. Soc.* 2014, 136, 8094-8099.
- 62 D. Pérez-del-Rey, D. Forgács, E. M. Hutter, T. J. Savenije, D. Nordlund, P. Schulz, J. J. Berry, M. Sessolo, H. J. Bolink, *Adv. Mater.* 2016, 28, 9839-9845.
- 63 W. Xu, L. Zheng, X. Zhang, Y. Cao, T. Meng, D. Wu, L. Liu, Wenping . Hu, X. Gong, *Adv. Energy Mater.* 2018, 1703178 (1-11).
- 64 Z. Wang, B. Lei, X. Xia, Z. Huang, K. P. Homewood, Y. Gao, *J. Phys. Chem. C* 2018, 122, 2589-2595.

- 65 A. L. Abdelhady, M. I. Saidaminov, B. Murali, V. Adinolfi, O. Voznyy, K. Katsiev, E. Alarousu, R. Comin, I. Dursun, L. Sinatra, E. H. Sargent, O. F. Mohammed, O. M. Bakr, *J. Phys. Chem. Lett.* 2016, 7(2), 295-301.
- 66 J. Navas, A. Sanchez-Coronilla, J. J. Gallardo, N. Cruz Hernandez, J. C. Pinero, R. Alcantara, C. Fernandez-Lorenzo, D. M. De los Santos, T. Aguilar, J. Martin-Calleja, *Nanoscale* 2015, 7, 6216-6229.
- 67 J. Navas, A. Sanchez-Coronilla, J. J. Gallardo, E. I. Martin, N. C. Hernandez, R. Alcantara, C. Fernandez-Lorenzo, J. Martin-Calleja, *Phys. Chem. Chem. Phys.* 2015, 17, 23886-23896.
- 68 C. McDowell, M. Abdelsamie, M. F. Toney, G. C. Bazan, *Adv. Mater.* 2018, 30, 1707114(1-30).
- 69 C. Liu, X. Hu, C. Zhong, M. Huang, K. Wang, Z. Zhang, X. Gong, Y. Cao, A. J. Heeger, *Nanoscale*, 2014, 6, 14297-14304
- 70 T. Li, Y. Pan, Z. Wang, Y. Xia, Y. Chen, W. Huang, *J. Mater. Chem. A* 2017,5, 12602-12652.
- 71 C. Wu, C. Chiang, Z. Tseng, M.-K. Nazeeruddin, A. Hagfeldt, M. Graetzel, *Energ. Environ. Sci.* 2015, 8, 2725.
- 72 C.-H. Chiang, M. K. Nazeeruddin, M. Grätzel, C.-G. Wu, *Energy Environ. Sci.* 2017,10, 808-817.
- 73 L. Zhao, D. Luo, J. Wu, Q. Hu, W. Zhang, K. Chen, T. Liu, Y. Liu, Y. Zhang, F. Liu, T.-P. Russell, H.-J. Snaith, R. Zhu and Q. Gong, *Adv. Funct. Mater.* 2016, 26, 3508.
- 74 X. Gong, M. Li, X. Shi, H. Ma, Z. Wang, L. Liao, *Adv. Funct. Mater.* 2015, 25, 6671-6678.
- 75 Y. Sun, J. Peng, Y. Chen, Y. Yao, Z. Liang, *Sci. Rep.* 2017, 7, 46193(1-7).
- 76 Yi. Cai, S. Wang, M. Sun, X. Li, Y. Xiao, *Org. Electron.* 2018, 53, 249-255.
- 77 Z. Xiao, L. Zhao, N. L. Tran, Y. L. Lin, S. H. Silver, R. A. Kerner, N. Yao, A. Kahn, G. D. Scholes, B. P. Rand, *Nano Lett.* 2017, 17, 6863-6869.
- 78 H. Tsai, W. Nie, J.-C. Blancon, C. C. Stoumpos, R. Asadpour, B. Harutyunyan, A. J. Neukirch, R. Verduzco, J. J. Crochet, S. Tretiak, L. Pedesseau, J. Even, M. A. Alam, G. Gupta, J. Lou, P. M. Ajayan, M. J. Bedzyk, M. G. Kanatzidis, A. D. Mohite, *Nature*, 2016, 536, 312-316.
- 79 A. Mei, X. Li, L. Liu, Z. Ku, T. Liu, Y. Rong, M. Xu, M. Hu, J. Chen, Y. Yang, M. Grätzel, H. Han, *Science*, 2014, 345, 295.
- 80 P. Schulz, D. Cahen, A. Kahn, *Chem. Rev.* 2019 119, 3349-3417.
- 81 L. Hu, K. Sun, M. Wang, W. Chen, B. Yang, J. Fu, Z. Xiong, X. Li, X. Tang, Z. Zang, S. Zhang, L. Sun, M. Li, *ACS Appl. Mater. Interfaces*, 2017, 9, 43902-43909.
- 82 S. Wang, H. Chen, J. Zhang, G. Xu, W. Chen, R. Xue, M. Zhang, Y. Li, Y. Li, *Adv. Mater.* 2019, 1903691(1-9).
- 83 A. Fakharuddin, L. Schmidt-Mende, G. Garcia-Belmonte, R. Jose, I. Mora-Sero, *Adv. Energy Mater.* 2017, 7, 1700623(1-44).

- 84 M. Ye, C. He, J. Iocozzia, X. Liu, X. Cui, X. Meng, M. Rager, X. Hong, X. Liu, Z. Lin, *J. Phys. D: Appl. Phys.* 2017, 50, 373002(1-16).
- 85 P. Wang, Z. Shao, M. Ulfa, T. Pauporte, *J. Phys. Chem. C* 2017, 121, 9131-9141.
- 86 R. Fan, Y. Huang, L. Wang, L. Li, G. Zheng, H. Zhou, *Adv. Energy Mater.* 2016, 6, 1600460(1-32).
- 87 W. Yan, S. Ye, Y. Li, W. Sun, H. Rao, Z. Liu, Z. Bian, C. Huang, *Adv. Energy Mater.* 2016, 1600474(1-20).
- 88 Z. Liu, J. Chang, Z. Lin, L. Zhou, Z. Yang, D. Chen, C. Zhang, S. (F.) Liu, Y. Hao, *Adv. Energy Mater.* 2018, 1703432(1-9).
- 89 G. Yang, C. Wang, H. Lei, X. Zheng, P. Qin, L. Xiong, X. Zhao, Y. Yan, G. Fang, *J. Mater. Chem. A* 2017, 5, 1658-1666.
- 90 J. Xu, A. Buin, A. H. Ip, W. Li, O. Voznyy, R. Comin, M. Yuan, S. Jeon, Z. Ning, J. J. McDowell, P. n Kanjanaboos, J.-P. Sun, X. Lan, L. N. Quan, D. H. Kim, I. G. Hill, P. Maksymovych, E. H. Sargent, *Nat. Commun.* 2015, 6, 7081(1-8).
- 91 C.-H. Chiang, C.-G. Wu, *Nat. Photonics*, 2016, 10, 196-200.
- 92 G.-W. Kim, G. Kang, J. Kim, G.-Y. Lee, H. Il Kim, L. Pyeon, J. Lee, T. Park Lee, *Energy Environ. Sci.* 2016, 9, 2326-2333.
- 93 T. Kirchartz, K. Taretto, U. Rau, *J. Phys. Chem. C* 2009, 113, 17958-17966.
- 94 W. Chen, Y. Zhu, Y. Yu, L. Xu, G. Zhang, Z. He, *Chem. Mater.* 2016, 28, 4879-4883.
- 95 W. Yan, Y. Li, Y. Li, S. Ye, Z. Liu, S. Wang, Z. Bian, C. Huang, *Nano Res.* 2015, 8, 2474-2480.
- 96 L. S. Hung, C. W. Tang, M. G. Mason, *Appl. Phys. Lett.* 1997, 70, 152-154.
- 97 H. Ding, Y. Geo, *Appl. Phys. Lett.* 2007, 91, 172107(1-3).
- 98 P. Docampo, J. M. Ball, M. Darwich, G. E. Eperon, H. J. Snaith, *Nat. Commun.* 2013, 4, 1-6.
- 99 S. D. Stranks, P. K. Nayak, W. Zhang, T. Stergiopoulos, H. J. Snaith, *Angew. Chem. Int. Ed.* 2015, 54, 3240-3248.
- 100 H. S. Jung, N. -G. Park, *Small*, 2015, 11, 10-25.
- 101 Y. Wu, A. Islam, X. Yang, C. Qin, J. Liu, K. Zhang, W. Peng, L. Han, *Energy Environ. Sci.* 2014, 7, 2934-2938.
- 102 X. Wang, X. Li, G. Tang, L. Zhao, W. Zhang, T. Jiu, J. Fang, *Org. Electron.* 2015, 24, 205-211.
- 103 P. Fassel, V. Lami, A. Bausch, Z. Wang, M. T. Klug, H. J. Snaith, Y. Vaynzof, *Energy Environ. Sci.* 2018, 11, 3380-3391.
- 104 C. Roldan-Carmona, P. Gratia, I. Zimmermann, G. Grancini, P. Gao, M. Graetzel, M. K. Nazeeruddin, *Energy Environ. Sci.* 2015, 8, 3550-3556.
- 105 Q. Jiang, Z. Chu, P. Wang, X. Yang, H. Liu, Y. Wang, Z. Yin, J. Wu, X. Zhang, J. You, *Adv. Mater.* 2017, 29, 1703852(1-7).
- 106 S. Tombe, G. Adam, H. Heilbrunner, C. Yumusak, D. H. Apaydin, B. Hailegnaw, C. Ulbricht, C. J. Arendse, H. Langhals, E. Iwuohaa, N. S. Sariciftci, M. C. Scharber, *Solar Energy*, 2018, 163, 215-223.

- 107 D. Bi, W. Tress, M. I. Dar, P. Gao, J. Luo, C. Renevier, K. Schenk, A. Abate, F. Giordano, J.-P. C. Baena, J.-D. Decoppet, S. M. Zakeeruddin, M. K. Nazeeruddin, M. Grätzel, A. Hagfeldt, *Sci. Adv.* 2016, 2, e1501170(1-7).
- 108 B.-W. Park, N. Kedem, M. Kulbak, D. Y. Lee, W. S. Yang, N. J. Jeon, J. Seo, G. Kim, K. J. Kim, T. J. Shin, G. Hodes, D. Cahen, S. I. Seok, *Nat. Commun.* 2018, 9, 3301(1-8).
- 109 B. Wang, E. Rivard, I. Manners, *Inorg. Chem.* 2002, 41, 1690
- 110 V. Poscher, I. Teasdale, Y. Salinas, *ACS Appl. Nanomater.* 2019, 2, 655-660.
- 111 S. Wilfert, H. Henke, W. Schoefberger, O. Brüggemann, I. Teasdale, *Macromol. Rapid Commun.* 2014, 35, 1135.
- 112 X. Yin, P. Chen, M. Que, Y. Xing, W. Que, Ch. Niu, J. Shao, *ACS Nano*, 2016, 10, 3630-3636.
- 113 S. H. Park, A. Roy, S. Beaupre, S. Cho, N. Coates, J. S. Moon, D. Moses, M. Leclerc, K. Lee, A. J. Heeger, *Nat. Photonics*, 2009, 3, 297-303.
- 114 C. Ran, J. Xu, W. Gao, C. Huang, S. Dou, *Chem. Soc. Rev.* 2018, 47, 4581-4610.
- 115 Q. Dong, Y. Fang, Y. Shao, P. Mulligan, J. Qiu, L. Cao, J. Huang, *Science*, 2015, 347, 967-970.
- 116 D. Shi, V. Adinolfi, R. Comin, M. Yuan, E. Alarousu, A. Buin, Y. Chen, S. Hoogland, A. Rothenberger, K. Katsiev, et al. *Science*, 2015, 347, 519-522.
- 117 J. Peng, Y. Chen, K. Zheng, T. Pullerits, Z. Liang, *Chem. Soc. Rev.* 2017, 46, 5714-5729.
- 118 V. F. Lvovich, *Impedance Spectroscopy: Applications to Electrochemical and Dielectric Phenomena*. John Wiley & Sons, Inc. 2012, pp1-21.
- 119 E. Barsoukov, J. R. Macdonald, *Impedance Spectroscopy: Theory, Experiment, and Applications*. 2nd Edition, A John Wiley & Sons, Inc., 2005, pp1-11.
- 120 E. von Hauff, *J. Phys. Chem. C* 2019, 12318, 11329-11346.
- 121 K. Adhitya, A. Alsulami, A. Buckley, R. C. Tozer, M. Grell, *IEEE Journal of Photovoltaics*, 2015, 5, 1414-1421.
- 122 B. Buzz, <https://electrochemistryresources.com/the-constant-phase-element-cpe/>. Posted on July, 2014, accessed on 09/16/2019.
- 123 M. Cha, P. Da, J. Wang, W. Wang, Z. Chen, F. Xiu, G. Zheng, Z.-S. Wang, *J. Am. Chem. Soc.* 2016, 138, 8581-8587.
- 124 A. Todinova, L. Contreras-Bernal, M. Salado, S. Ahmad, N. Morillo, J. Idígoras, J. A. Anta, *ChemElectroChem*. 2017, 4, 2891-2901.
- 125 D. Klotz, D. S. Ellis, H. Dotan, A. Rothschild, *Phys. Chem. Chem. Phys.* 2016, 18, 23438-23457.
- 126 I. Zarazua, G. Han, P. P. Boix, S. Mhaisalkar, F. Fabregat-Santiago, I. M. Sero, J. Bisquert, G. Garcia-Belmonte, *J. Phys. Chem. Lett.* 2016, 7, 5105-5113.
- 127 A. Guerrero, G. Garcia-Belmonte, I. Mora-Sero, J. Bisquert, Y. S. Kang, T. J. Jacobsson, J. P. Correa-Baena, A. Hagfeldt, *J. Phys. Chem. C* 2016, 120, 8023-8032.

- 128 T. Bu, J. Li, F. Zheng, W. Chen, X. Wen, Z. Ku, Y. Peng, J. Zhong, Y.-B. Cheng, F. Huang, *Nat. commun.* 2018, 9, 4609(1-10).
- 129 J. Zhang, W. Mao, X. Hou, J. Duan, J. Zhou, S. Huang, W. Ou-Yang, X. Zhang, Z. Sun, X. Che, *Solar Energy*, 2018, 174, 1133-1141.
- 130 X. Guo, C. McCleese, C. Kolodziej, A. C. S. Samia, Y. Zhao, C. Burda, *Dalton Trans.* 2016, 45, 3806-3813.
- 131 H. Back, G. Kim, J. Kim, J. Kong, T. K. Kim, H. Kang, H. Kim, J. Lee, S. Lee, K. Lee, *Energy Environ. Sci.* 2016, 9, 1258-1263.
- 132 J. C. Yu, J. A. Hong, E. D. Jung, D. B. Kim, S.-M. Baek, S. Lee, S. Cho, S. S. Park, K. J. Choi, M. H. Song, *Sci. Rep.* 2018, 8, 1-9.
- 133 A. Pockett, G. E. Eperon, T. Peltola, H. J. Snaith, A. Walker, L. M. Peter, P. J. Cameron, *J. Phys. Chem. C* 2015, 119, 3456-3465.
- 134 Y. Zhou, Z. Zhou, M. Chen, Y. Zong, J. Huang, S. Pang, N. P. Padture, *J. Mater. Chem. A* 2016, 4, 17623-17635.
- 135 Z. H. Bakr, Q. Wali, A. Fakhruddin, L. Schmidt-Mende, T. M. Brown, R. Jose, *Nano Energy*, 2017, 34, 271-305.
- 136 B. Chen, M. Yang, S. Priya, K. Zhu, *J. Phys. Chem. Lett.* 2016, 7, 905-917.
- 137 A. F. Akbulatov, L. A. Frolova, M. P. Griffin, I. R. Gearba, A. Dolocan, D. A. van den Bout, S. Tsarev, E. A. Katz, A. F. Shestakov, K. J. Stevenson, P. A. Troshin, *Adv. Energy Mater.* 2017, 1700476, 1-7.
- 138 J. You, L. Meng, T.-B. Song, T.-F. Guo, Y. (M.) Yang, W.-H. Chang, Z. Hong, H. Chen, H. Zhou, Q. Chen, Y. Liu, N. De Marco, Y. Yang, *Nature Nanotech.* 2016, 11, 75-81.
- 139 Q. Bao, X. Liu, S. Braun, M. Fahlman, *Adv. Energy Mater.* 2014, 4, 1-7.
- 140 S. Rothmund, I. Teasdale, *Chem. Soc. Rev.* 2016, 45, 5200-5215.
- 141 M. Deng, S. G. Kumbar, Y. Wan, U. S. Toti, H. R. Allcock, C. T. Laurencin, *Soft Matter*, 2010, 6, 3119-3132.
- 142 A. Linhardt, M. König, W. Schöfberger, O. Brüggemann, A. K. Andrianov, I. Teasdale, *Polymers*, 2016, 8, 1-16.
- 143 J. Paulsdorf, N. Kaskhedikar, M. Burjanadze, S. Obeidi, N. A. Stolwijk, D. Wilmer, H.-D. Wiemhöfer, *Chem. Mater.* 2006, 18, 1281-1288.
- 144 I. Teasdale, *Eur. J. Inorg. Chem.* 2018, DOI: 10.1002/ejic.201801077.
- 145 T. Mayer-Gall, D. Knittel, J. S. Gutmann, K. Opwis, *ACS Appl. Mater. Interfaces*, 2015, 7, 9349-9363.
- 146 C. G. Zoski, *Handbook of Electrochemistry*, Elsevier, 1000 AE Amsterdam, The Netherlands, 2007, pp 73-110.
- 147 C. M. Cardona, W. Li, A. E. Kaifer, D. Stockdale, G. C. Bazan, *Adv. Mater.* 2011, 23, 2367-2371.

- 148 D. Baran, A. Balan, S. Celebi, B. M. Esteban, H. Neugebauer, N. S. Sariciftci, L. Toppare, *Chem. Mater.* 2010, 22, 2978-2987.
- 149 S. S. Mali, H. Kim, H. H. Kim, S. E. Shim, C. K. Hong, *Mater. Today*, 2018, 21, 483.
- 150 D. Prochowicz, M. M. Tavakoli, S.-H. Turren-Cruz, K. Pandey, M. Saliba, P. Yadav, *Sustainable Energy Fuels*, 2018, 2, 2407-2411.
- 151 A. R. Pascoe, N. W. Duffy, A. D. Scully, F. Huang, Y.-B. Cheng, *J. Phys. Chem. C* 2015, 119, 4444-4453.
- 152 G. Adam, M. Kaltenbrunner, E. D. Głowacki, M. S. White, H. Heilbrunner, S. Tombe, P. Stadler, N. S. Sariciftci, M. C. Scharber, *Sol. Energy Mater. Sol. Cells*, 2016, 157, 318-325.
- 153 T. Singh, T. Miyasaka, *Adv. Energy Mater.* 2017, 1700677, 1-9.
- 154 M. Guo, F. Li, L. Ling, C. Chen, *J. Mater. Chem. C* 2017,5, 12112-12120.
- 155 N. Arora, M. I. Dar, A. Hinderhofer, N. Pellet, F. Schreiber, S. M. Zakeeruddin, M. Grätzel, *Science*, 2017, 358, 768.
- 156 S.-J. Lou, J.-M. Szarko, T. Xu, L. Yu, T.-J. Marks, L.-X. Chen, *J. Am. Chem. Soc.* 2011, 133, 20661-20663.
- 157 Y. Rong, Z. Tang, Y. Zhao, X. Zhong, S. Venkatesan, H. Graham, M. Patton, Y. Jing, A.M. Guloy, Y. Yao, *Nanoscale*, 2015, 7, 0595-10599.
- 158 K. Lyczko, J. Narbutt, B. Paluchowska, J. K. Maurin, I. Persson, *Dalton Trans.* 2006, 0, 3972-3976.
- 159 J. A. Suttill, J. F. Kucharyson, I. L. Escalante-Garcia, P. J. Cabrera, B. R. James, R. F. Savinell, M. S. Sanford, L. T. Thompson, *J. Mater. Chem. A* 2015, 3, 7929-7938.
- 160 T. Oku, *Crystal Structures of CH₃NH₃PbI₃ and Related Perovskite Compounds Used for Solar Cells*, 2015, DOI: 10.5772/59284.
- 161 Q. Chen, H. Zhou, Y. Fang, A. Z. Stieg, T.-B. Song, H.-H. Wang, X. Xu, Y. Liu, S. Lu, J. You, P. Sun, J. McKay, M. S. Goorsky, Y. Yang, *Nat. Commun.* 2015, 6, 7269(1-9).
- 162 S. Luo, W. A. Daoud, *Mater.* 2016, 9, 123; doi:10.3390/ma9030123
- 163 N. Yantara, F. Yanan, C. Shi, H. A. Dewi, P. P. Boix, S. G. Mhaisalkar, N. Mathews, *Chem. Mater.* 2015, 27, 2309-2314.
- 164 O. Almora, C. Aranda, E. Mas-Marza, G. Garcia-Belmonte, *Appl. Phys. Lett.* 2016, 109, 173903 (1-5).
- 165 I. J. Park, S. Seo, M. A. Park, S. Lee, D. H. Kim, K. Zhu, H. Shin, J. Y. Kim, *ACS Appl. Mater. Interfaces*, 2017, 9, 41898-41905.
- 166 B. Hailegnaw, G. Adam, H. Heilbrunner, D. H. Apaydin, C. Ulbricht, N. S. Sariciftci, M. C. Scharber, *RSC Adv.* 2018, 8, 24836-24846.
- 167 X. Qin, Z. Zhao, Y. Wang, J. Wu, Q. Jiang, J. You, *J. Semicond.* 2017, 38, 011002(1-9)
- 168 S. Heo, G. Seo, Y. Lee, M. Seol, S. H. Kim, D.-J. Yun, Y. Kim, K. Kim, J. Lee, J. Lee, W. S. Jeon, J. K. Shin, J. Park, D. Lee, M. K. Nazeeruddin, *Adv. Mater.* 2019, 31, 1805438(1-5).

-
- 169 U. Krishnan, M. Kaur, M. Kumar, A. Kumar, *J. of Photonics for Energy*, 2019, 9, 021001(1-42).
- 170 L. Meng, J. You, Y. Yang, *Nat. Commun.* 2018, 9, 5265(1-4).
- 171 W. Tress, K. Domanski, B. Carlsen, A. Agarwalla, E. A. Alharbi, M. Graetzel, A. Hagfeldt, *Nature energy*, 2019, 4, 568-574.
- 172 R. Fu, W. Zhou, Q. Li, Y. Zhao, D. Yu, Q. Zhao, *ChemNanoMat*. 2019, 5, 253-265.
- 173 F. A. Roghabadi, M. Alidaei, S. M. Mousavi, T. Ashjari, A. S. Tehrani, V. Ahmadi, S. M. Sadrameli, *J. Mater. Chem. A* 2019, 7, 5898-5933.
- 174 Z. Wang, D. P. McMeekin, N. Sakai, S. van Reenen, K. Wojciechowski, J. B. Patel, M. B. Johnston, H. J. Snaith, *Adv. Mater.* 2017, 29, 1604186(1-8).
- 175 S. Yang, S. Chen, E. Mosconi, Y. Fang, X. Xiao, C. Wang, Y. Zhou, Z. Yu, J. Zhao, Y. Gao, F. De Angelis, J. Huang, *Science*, 2019, 365, 473-478.
- 176 C. C. Boyd, R. Cheacharoen, T. Leijtens, M. D. McGehee, *Chem. Rev.* 2019, 119, 3418-3451.
- 177 F. Bella, G. Griffini, J.-P. Correa-Baena, G. Saracco, M. Grätzel, A. Hagfeldt, S. Turri, C. Gerbaldi, *Science*, 2016, 354, 203-206.
- 178 A. Pockett, G. E. Eperon, N. Sakai, H. Snaith, L. M. Peter, P. J. Cameron, *Phys. Chem. Chem. Phys.* 2017, 19, 5959-5970.
- 179 P. Wang, M. Ulfa, T. Pauporte, *J. Phys. Chem. C* 2018, 122, 1973-1981.
- 180 Q. Wang, *J. Phys. Chem. C* 2018, 122, 4822-4827.
- 181 H.-S. Kim, I.-H. Jang, N. Ahn, M. Choi, A. Guerrero, J. Bisquert, N.-G. Park, *J. Phys. Chem. Lett.* 2015, 6, 4633-4639.

Curriculum Vitae

Family name: Teklemariam

First name [given name]: Bekele Hailegnaw

Address

Linz Institute for Organic Solar Cells (LIOS),
Johannes Kepler University Linz,
Altenberger Straße 69, 4040 Linz,
Austria



Nationality: Ethiopian

Date of Birth: June 23, 1986

Email: bekele.teklemariam@jku.at

Academic Qualifications

University/ Status

Duration

Johannes Kepler University Linz, Austria

Oct. 2016 – now

PhD student at the Institute of Physical Chemistry

PhD Thesis Title: *Role of interfaces in perovskite devices.*

Weizmann Institute of Science, Israel

Oct. 2013 - Jan. 2016

M.Sc. in Materials and interface Science

Addis Ababa University, Ethiopia

Sept. 2010 - Jul.2012

M.Sc. in Chemistry (Physical Chemistry)

Bahir Dar University, Ethiopia

Sept.2004-Jul. 2007

Bachelor Degree in Chemistry

Research Experience

- ✓ **Hybrid organic-inorganic perovskite solar cells-** fabrication, characterization and investigation of perovskite solar cells, specifically on the physics and chemistry of interfaces and its effect on the performance and stability of solar cells.
- ✓ **Growth and characterization of crystals-** growth of perovskite and other material based single crystals and characterization of the optoelectrical, magnetic and crystallographic properties.
- ✓ **Semiconductor sensitized solar cells:** M.Sc. thesis work at Weizmann Institute of Science in the area of semiconductor sensitized solar cells (SSSCs) with the title *“Effect*

of Different Solution Deposition Techniques on Semiconductor-sensitized solar cells based on CdS and Perovskite Semiconductors Solar Cells”,

- ✓ **Organic Solar Cells:** fabrication and characterization of bulk-heterojunction organic solar cells, at Addis Ababa University, Ethiopia,
- ✓ **Catalysis:** “Catalytic depolymerisation of cellulose in water using phenylboronic acid derivatives” at Weizmann Institute of Science.

Publications

1. B. Hailegnaw, G. Adam, D. Wielend, J. D. Pedarnig, N. S. Sariciftci, M. C. Scharber, Acetylacetone Improves the Performance of Planar Mixed Halide Perovskite Solar Cells, *Journal of Physical Chemistry C* 2019, DOI: 10.1021/acs.jpcc.9b05058.
2. B. Hailegnaw, S. Paek, K. T. Cho, Y. Lee, F. Ongül, M. K. Nazeeruddin, M. C. Scharber, Optoelectronic Properties of Layered Perovskite Solar Cells, *Solar Rapid Research Letters*, 2019, 1900126(1-6).
3. B. Hailegnaw, V. Poscher, C. Ulbricht, H. Seelajaroen, I. Teasdale, Y. Salinas, N. S. Sariciftci, M. C. Scharber, Improving the Performance of Perovskite Solar Cells Using a Polyphosphazene Interfacing layer, *Physica Status Solidi A* 2019, 1900436(1-10).
4. B. Hailegnaw, G. Adam, H. Heilbrunner, D. H. Apaydin, C. Ulbricht, N. S. Sariciftci, M. C. Scharber, Inverted (p-i-n) Perovskite Solar Cells Using Low Temperature Processed TiO_x Interlayer, *RSC Advances*, 2018, 8, 24836-24846.
5. S. Tombe, G. Adam, H. Heilbrunner, C. Yumusak, D. H. Apaydin, B. Hailegnaw, C. Ulbricht, C. J. Arendse, H. Langhals, E. Iwuohaa, N. S. Sariciftci, M. C. Scharber, The influence of perovskite precursor composition on the morphology and photovoltaic performance of mixed halide MAPb_{1-3-x}Cl_x solar cells, *Solar Energy*, 2018, 163, 215-223.
6. N. Levi, A. M. Khenkin, B. Hailegnaw, R. Neumann, Depolymerization of Cellulose in Water Catalyzed by Phenylboronic Acid Derivatives, *ACS Sustainable Chemistry and Energy*, 2016, 4, 5799-5803.
7. B. Hailegnaw, S. Kirmayer, E. Edri, G. Hodes, D. Cahen, Rain on Methylammonium Lead Iodide Based Perovskites: Possible Environmental Effects of Perovskite Solar Cells, *Journal of Physical Chemistry Letters*, 2015, 6 (9), 1543-1547.
8. B. Hailegnaw, G. Adam, T. Yohannes, Effect of Short Chain Iodoalkane Solvent Additives on Photovoltaic Performance of Poly(3-hexylthiophene) and Phenyl-C₆₁-butyric Acid Methyl Ester Based Bulk Heterojunction Solar Cells, *Thin Solid Films* (2015), 589, 272-277.

Workshops and Conferences Attained

- July, 2019: Europe-Korea Conference on Science and Technology-2019 (EKC-2019) at Vienna, Austria,
- March, 2019: Quantsol-2019 Winter Workshop at Rauris, Austria,

- September, 2015: 33rd Israel Vacuum Society Annual Conference at Rehovot, Israel,
- February, 2015: The 80th Annual Meeting of the Israel Chemical Society at Tel Aviv, Israel,
- February, 2015: Workshop on Metal Oxide Material Discovery and Applications at Jerusalem, Israel,
- December, 2012: Joint US-Africa Materials Institute First School on Materials for Sustainable Energy in Addis Ababa, Ethiopia,
- May 2010: African School on Nanoscience for Solar Energy Conversion Workshop at Addis Ababa, Ethiopia.

Award

Award	Year	Organization
Award of <i>Gold Medal</i> for Outstanding academic performance in the university	2007	Bahir Dar University, Ethiopia
Award of Certification for my excellent academic performance	2012	Addis Ababa University, Ethiopia
Award of best poster on Europe-Korea Conference on Science and Technology (EKC-2019)	2019	EKC-2019 at Vienna, Austria